

Alma Mater Studiorum – Università di Bologna

DOTTORATO DI RICERCA IN

**INGEGNERIA ELETTRONICA, TELECOMUNICAZIONI E TECHNOLOGIE
DELL' INFORMAZIONE**

Ciclo 34

Settore Concorsuale: 09/F1 - CAMPI ELETTROMAGNETICI

Settore Scientifico Disciplinare: ING-INF/02 - CAMPI ELETTROMAGNETICI

**PROPAGATION MODELLING AND RESOURCE ALLOCATION IN MOBILE
RADIO COMMUNICATIONS**

Presentata da: Denis Bilibashi

Coordinatore Dottorato

Aldo Romani

Supervisore

Vittorio Degli Esposti

Co-Supervisore

Enrico Maria Vitucci

Esame finale anno 2022

Acknowledgements

Hereby i would like to express my gratitude to every person that has contributed to the completion of this thesis.

First of all, I would like to express my sincere gratitude my supervisors Prof. Vittorio Degli Esposti and Prof. Enrico M. Vitucci for their guidance, availability and patience during these 3 years. I would like to thank them for the opportunity to work and learn from them.

Furthermore, I would like to thank Prof. Andrea Giorgetti for his help, valuable recommendations and advices regarding the second part of this thesis. Without him that part wouldn't have been possible.

Last but not least, I would like to thank my family and my fiancée for all their support and encouragements during this period. Their patience and love guided me through this PhD period.

Abstract

Over the past years, ray tracing (RT) models popularity has been increasing. From the nineties, RT has been used for field prediction in environment such as indoor and urban environments. Nevertheless, with the advent of new technologies, the channel model has become decidedly more dynamic and to perform RT simulations at each discrete time instant become computationally expensive. In this thesis, a new dynamic ray tracing (DRT) approach is presented in which from a single ray tracing simulation at an initial time t_0 , through analytical formulas we are able to track the motion of the interaction points. The benefits that this approach bring are that Doppler frequencies and channel prediction can be derived at every time instant, without recurring to multiple RT runs and therefore shortening the computation time. DRT performance was studied on two case studies and the results shows the accuracy and the computational gain that derives from this approach.

Another issue that has been addressed in this thesis is the licensed band exhaustion of some frequency bands. To deal with this problem, a novel unselfish spectrum leasing scheme in cognitive radio networks (CRNs) is proposed that offers an energy-efficient solution minimizing the environmental impact of the network. In addition, a network management architecture is introduced and resource allocation is proposed as a constrained sum energy efficiency maximization problem. System simulations demonstrate an increment in the energy efficiency of the primary users' network compared with previously proposed algorithms.

Contents

Acknowledgements	i
Abstract	i
1 Introduction	2
1.1 Thesis outline	3
I On Dynamic Ray Tracing and Anticipative Channel Prediction for Vehicular Environment	5
2 Background and state of the art	6
2.1 Propagation modeling	6
2.1.1 Channel models	7
2.2 Ray Tracing method	9
2.3 Dynamic environments	10
2.4 Summary of Ray Tracing	11
3 Ray Tracing theory	13
3.1 Solving Maxwell's equations using GO assumptions	13
3.2 Reflection	16
3.3 Diffuse scattering	17
3.4 Diffraction from an edge	18
3.4.1 Geometrical theory of diffraction	19
3.4.2 Uniform theory of diffraction	20
4 Dynamic Ray Tracing	23
4.1 The DRT concept	23

4.2	DRT algorithm description	25
4.2.1	Reflection points' calculation	27
4.2.2	Diffraction Points' Calculation	34
4.2.3	Diffuse scattering	37
4.3	Validation on case studies	37
4.3.1	Case study 1: Street canyon	37
4.3.2	Case study 2: Comparison with measurements in an intersection	41
4.3.3	Computational gain	45
4.3.4	Future prospect: Predictive Radio Awareness	46
II An Energy-Efficient Unselfish Spectrum Leasing Scheme for Cognitive Radio Networks		48
5	Background and motivation	49
5.1	Introduction to CRNs	49
5.1.1	Key technologies in CRN	51
5.2	Cooperative communications in CRN	52
5.3	Spectrum leasing in CCRN	53
5.4	Motivation and contribution	54
6	Proposed architecture and system model for CCRN	57
6.1	Proposed Architecture	57
6.2	System Model	58
7	Proposed joint resource allocation and relay selection scheme	61
7.1	Energy Efficiency of PUs	61
7.1.1	Direct Mode	62
7.1.2	Relay Mode	62
7.2	Energy Efficiency of SUs	63
7.3	Energy Efficiency for CCRN Problem Formulation and Solution . . .	64
7.3.1	Optimization Problem Formulation	64
7.3.2	Power Allocation Subproblem	65

7.3.3	Equivalent Problem Transformation	66
7.3.4	Energy Efficiency Maximization	67
7.3.5	Transmission Mode and Relay Selection Subproblem	71
7.4	Numerical Results	72
7.4.1	Convergence of the Iterative Algorithm	74
7.4.2	Energy Efficiency Versus Maximum Transmit Power	74
7.4.3	Energy Efficiency Versus Number of PUs	75
7.4.4	Energy Efficiency Versus Path Loss Exponent	76
7.4.5	Energy Efficiency Versus Shadowing Standard Deviation	77
7.4.6	Energy Efficiency Versus Time Slot Division	77
7.5	Future incorporation with RT models	79
8	Conclusions	80
A	Doppler frequency calculation	82
B	Reflection points' velocity and acceleration calculation	84
C	Diffraction Point's Velocity and Acceleration Calculation	87
D	Proof of Theorem 1	88
E	Summary of K-M algorithm	90
E.1	Solving Optimal Relay Selection Problem Based on K-M Algorithm	91
E.2	Complexity of the K-M Algorithm	92
	Bibliography	92

List of Figures

2.1	Ray tracing in an urban environment. (Source [6])	10
3.1	Narrow astigmatic ray tube. (Source [31])	15
3.2	Example of reflected and transmitted ray with two different mediums represented by the refraction indices n_1 and n_2	17
3.3	Geometry for diffraction by an edge	19
3.4	Diffacted rays cone (Source [31])	20
3.5	Edge-fixed coordination geometry [33]	21
4.1	Representation of single multi-bounce ray path.	23
4.2	Example of the composition of the dynamic environment database . .	26
4.3	Example of the dynamic database	27
4.4	Example of a single reflection scenario with the plane Π^I that rotates w.r.t. to the global frame. a) Scenario at $t = t_0$ and instantaneous velocities of TX, image-TX, RX, and reflection point Q_R . b) Scenario at $t = t_0 + \Delta t$	29
4.5	Flowcharts showing DRT algorithm : in (a) single reflection algorithm is presented, in (b) double reflection procedure is shown.	35
4.6	Example of edge diffraction, and related geometry for the computa- tion of the diffraction point.	36
4.7	Ideal street canyon with a moving parallelepiped representing a bus and two moving terminals TX and RX. In (a) the bus is moving the middle lane, in (b) in the side lane.	38
4.8	PDfP evolution in a V2V scenario with a simulation time of 5 seconds.	39
4.9	Absolute value of error between standard multiple-run RT and DRT analytical approach	40

4.10	PDFP for a snapshot of the V2V scenario with reflection from bus side (see Fig. 4.6(b)). Here TX and RX are moving in the same direction at 28 km/h and 30 km/h, respectively, while bus is moving at 30 km/h in the opposite direction. Bus moving straight without (blue) and with (red) rotation.	41
4.11	Intersection scenario in the city of Lund, Sweden	42
4.12	Power Delay Profile obtained from measurements (a) and (b), from RT simulations (c) and (d) and from DRT prediction (e) and (f) . . .	44
4.13	PDP obtained from simulation with DRT. In (a) $3T_C$ were used, in (b) $10T_C$	45
4.14	Scheme of an environment-aware system including both channel prediction and localization	47
6.1	Proposed architecture and scenario for the cell.	58
6.2	Bandwidth allocation and time slot division for PU and SU.	59
7.1	Energy efficiency versus number of iterations with $M = 10$ and $K = 10$, for different circuit power consumption P_c	75
7.2	Energy efficiency varying the maximum transmit power. Three different algorithms are compared. M and K in this case change randomly from 1 to 10.	76
7.3	Energy efficiency varying number of PUs. M varies from 2 to 18 and $K = 10$	77
7.4	Energy efficiency increment with respect to direct mode varying the path loss exponent. M and K change randomly from 1 to 15 while $\sigma_s = 8\text{dB}$	78
7.5	Energy efficiency increment with respect to direct mode versus shadowing standard deviation. M and K in this case change randomly within 1 and 15 while $\gamma = 3$	78
7.6	Energy efficiency versus time slot division in the relay transmission link. The parameters M and K are random variables uniformly distributed from 1 to 10.	79
A.1	Representation of the multiple scatterers Doppler model	83

List of Tables

4.1	Execution time for RT and DRT in M1 and M2	46
7.1	Tables of direct mode and cooperative mode	71
7.2	System parameters	74

List of acronyms

EM Electromagnetic

TX Transmitter

RX Receiver

GSCM Geometry-based Stochastic Channel Models

MoM Method of Moments

FDTD Finite Difference Time Domain

RT Ray Tracing

D2D Device to device

V2V Vehicular communications

UMi 3D-urban micro

UMa 3D-urban macro

GO Geometrical Optics

LoS line-of-sight

NLoS non line-of-sight

DRT Dynamic Ray Tracing

GTD Geometrical Theory of Diffraction

UTD Uniform Theory of Diffraction

PDfP Power Doppler frequency profile

PDP Power delay profile

CR Cognitive radio

CRN Cognitive radio network

PU Primary user

SU Secondary user

CCRN Cooperative cognitive radio network

PDA Personal digital assistant

PBS Primary base station

CC Cooperative communications

WLAN Wireless Local Area Network

QoS Quality of service

URME User resource management entity

LRME Local resource management entity

CRME Cell resource management entity

SBS Secondary base station

OFDMA Orthogonal Frequency Division Multiple Access

DF Decode-and-forward

KKT Karush-Kuhn-Tucker

K-M Kuhn-Munkres

Chapter 1

Introduction

Mobile communications networks have experienced tremendous development over the decades providing year after year more services with higher efficiency and capacity. The use of mobile communications nowadays has become a daily part of humanity. With this massive and exponential increase of data usage and connectivity of a large number of mobile-connected devices, significant pressure has been placed on mobile service providers and the research community to find solution in providing high data rates and good quality of service (QoS) at affordable rates [1] [2]. This demand can only be met by advancing to new technologies that can provide wireless services and systems to various subscribers.

With the advent of mmWave and vehicular communications (V2V), highly dynamic radio channels are becoming more frequent. The dynamicity of radio channels introduces several issues such as abrupt transitions between line-of-sight (LoS) and non line-of-sight (NLoS) due to lower diffraction contributions or high values of Doppler shifts due to the high carrier frequencies and terminals' high velocity. Due to these reasons and large variety of possible environments and system configurations, accurate deterministic propagation models are needed for the deployment and simulation of future communication networks. Ray Tracing (RT) has gained interest and is expected to assist in simulating these new generation networks. Nevertheless, RT algorithms introduce a high degree of time complexity which would require a huge CPU time.

In the first part of this thesis a new Dynamic Ray Tracing (DRT) is presented. DRT is presented as a new paradigm where RT is redesigned and extended to com-

pute the speed and acceleration of rays' contribution points on objects' surfaces through analytical formulas on the base of the roto-translational speed and acceleration of the moving objects. The advantages of DRT are that Doppler Frequencies as well as the field/channel prediction for a time instant $t \in \Delta t$ can be derived from a single RT run through a fast analytical formulation, without resorting to multiple RT runs shortening the computation time [3], [4].

Another issue brought to surface by the exponential growth of mobile network services is the current static spectrum policy used by most countries in the world. This has almost resulted in licensed spectrum exhaustion of some frequency bands. On the contrary, recent spectrum utilization measurements have shown that the available spectrum opportunities are severely underutilized. Cognitive radio (CR), with its ability to sense available frequency bands and adaptively adjust transmission frequency, has attracted considerable attention as one of the most promising solutions to spectrum under-utilization [5]. Traditionally in CR networks (CRNs), there are two categories of users, namely, primary users (PUs) and secondary users (SUs). PUs are licensed users, and they have the exclusive right to use their respective channels, while SUs are unlicensed, and they wish to use the underutilized channels. To pay off the use of a licensed band, cooperative CRNs (CCRN) have been proposed in which SUs act as relays to provide a better transmission performance to the PUs.

In the second part of this thesis, an energy-efficient communication in multiuser CRN is presented. In addition, to provide improved cooperation between PUs and SUs and to secure an unselfish behavior of each user, we propose a resource management network architecture for a considered cell. This architecture, composed of various entities, will be responsible for making decisions regarding the usage of relay and for applying the optimal strategy to achieve the maximum energy efficiency of the cell [5].

1.1 Thesis outline

This thesis is divided into two parts. In part I, a new DRT and anticipative channel prediction for V2V is presented. Meanwhile in part II, an energy-efficient unselfish

spectrum leasing for CRN is introduced.

Part I is divided into three chapters. In Chapter 2, a brief background about propagation modelling and available channel models is presented as well as the main research trends in the field for RT models. It also presents the state of the art and motivation for DRT. Chapter 3 presents a mathematical background behind the RT theory and explains the concept of ray. Using the equations gathered in Chapter 3, the received electric fields can be determined. The DRT algorithm is presented in Chapter 4. To assess the performance of such algorithm, results are presented in different scenarios, i.e., an ideal street canyon and comparison with measurements performed in an intersection.

Part II also consists of three chapters. In Chapter 5 a brief introduction to CRN and cooperative communication is given as well as a presentation of the state of the art in spectrum leasing in CCRN. In the last part of the chapter the motivation and contribution of this work are presented in detail. An architecture composed of various entities is proposed for CCRN in Chapter 6. Also the system model is explained and a stochastic channel model is used to represent the propagation channel. The new proposed resource allocation and relay selection scheme is shown in Chapter 7. The proposed algorithm is formulated as an energy efficiency optimization problem and solved by transforming the objective function into two sub-problems. To evaluate the system performance and effectiveness of the proposed solution, Monte Carlo simulations are performed. As a last section, a new approach to model the propagation model is presented using RT models which is part of our future work.

Part I

On Dynamic Ray Tracing and Anticipative Channel Prediction for Vehicular Environment

Chapter 2

Background and state of the art

2.1 Propagation modeling

In any wireless communication system, radio waves are employed to carry the signals or information in a wireless channel. Although electromagnetic (EM) waves are governed by Maxwell conditions with appropriate boundary conditions, in general it is not possible to have an analytical solution for EM field in a realistic propagation environment. The purpose of propagation modeling is to obtain an estimation of field/signal strengths when some of the parameters of the wireless system are given, such as the frequency, terrain characteristics, antenna height, and so on [6].

The Friis equation for free space radio propagation, can be regarded as the simplest propagation model and was first published in 1946 [7]. It relates the free space path loss, antenna gains (G_{RX}, G_{TX}) and wavelength (λ) to the received (P_{RX}) and transmit powers (P_{TX}):

$$\frac{P_{RX}}{P_{TX}} = G_{RX}G_{TX} \left(\frac{\lambda}{4\pi d} \right)^2 \quad (2.1)$$

Nevertheless, the received power computed in (2.1), is referred as the direct field from the transmitting antenna. In case of an object into the Fresnel zone defined by the transmitter (TX) and receiver (RX) locations, then the free space assumption fails. In this case the reflected and diffracted field needs to be taken in consideration in order to count the effect of these objects. These effects may be related with ground reflection and diffraction from mountain peaks and ridges. For the reflection the calculation might be simpler, but the diffracted field is much more difficult to

compute. For scenarios in which the free space assumption fails, there exists different types of channel models which will be presented in the next sections.

2.1.1 Channel models

Channel measurements can be costly and time consuming. Therefore, to design a wireless communication system, the propagation channel is simulated thanks to channel models. They can be categorized into three types: empirical, stochastic and deterministic.

Empirical models The first of the channel models is widely used and developed based on extensive field measurements in typical propagation scenarios. Empirical models in general are used in macrocell scenarios to predict narrow-band characteristics of the channel, i.e., path loss. One of the most known models is the Hata-Okumura model for urban regions [8–10]. The formula expressed in dB units and is used to calculate the path loss L :

$$L_{dB} = A + B \log(d_{km}) - C, \quad (2.2)$$

where L_{dB} is the path loss in dB units, d_{km} is the distance in kilometers between base station and mobile terminal, A and B are parameters that depend on the frequency and base station height, while C depends on frequency, mobile terminal height and the type of propagation environment (urban, suburban or open area). There also exist extensions of this model, such as COST-Hata-Model [11]. The empirical models are in general simple and fast in terms of computation. The main disadvantage is that they are in general limited in range and mostly valid to the environment similar to the ones the model is developed, e.g. the environment of the Hata-Okumura model is Tokyo which might be very different from a typical European environment [6], [12].

Stochastic models The second type of channel model is the stochastic one, in which a statistical characterization of the channel is known. These models are not generally derived by measurements, but typical measurements scenarios are used to derive their parameters. They are more complex than empirical models but can provide a more detailed description of channel characteristics.

One important type of stochastic channel model is Geometry-Based Stochastic Channel Models (GSCM), which refers to the geometric distribution of scatterers in a scenario to model the stochastic properties of the channels [13], [14]. The advantages of these models are their much higher relation to physical propagation and the fact that they can reproduce full channel characteristics.

Deterministic models None of the above mentioned models considers all the elements of an environment and this can result in circumstances where the surroundings have a great impact on the electromagnetic propagation (i.e., vegetation, different types of scatterers or other materials present in a certain environment). For this reason, deterministic models are widely used in the past years for propagation predictions, given a specific environment. These methods are based on the ray optics and solve the Maxwell's equations in a high frequency regime and take into account all the elements of an environment.

The most accurate deterministic models are the ones that directly derive from the solution of Maxwell's equations such as Method of Moments (MoM) and Finite Difference Time Domain (FDTD). It is well-known that these two methods are highly impractical in a large-scale environment due to their complexity.

The most commonly used type of deterministic models are the ray-based approaches like Ray Tracing (RT) [15], [16]. In RT approach, imaging techniques are employed, leading to a number of possible paths that rays follow from the transmitter to the receiver over direct, reflected and diffracted rays. Their accuracy is very high but is related with the accuracy of the scenario representation [12]. The main disadvantage though is that RT technique requires a high computational effort. In Chapter 3, RT theory will be presented and the propagation mechanism formulas will be shown in more detail.

5G models Next generation 5G cellular systems will encompass frequencies from around 500 MHz up to 100 GHz. For the development of the new 5G systems to operate in bands above 6 GHz, there is a need for accurate radio propagation models for higher frequencies. Previous presented models were designed and evaluated for operation at frequencies only as high as 6 GHz.

New channel models will need to be based on existing 3GPP 3D channel model [17] which provides additional flexibility for the elevation dimension, thereby al-

lowing modelling for two dimensional antenna systems. Furthermore, new channel model must support large channel bandwidths (up to 2 GHz). Additionally, must accommodate mobility, in particular should be suitable for mobility up to 350 km/h, also small-scale mobility in order to support scenarios such as device to device (D2D) or vehicular communications (V2V).

Important examples are the recently developed 3D-urban micro (UMi) and 3D-urban macro (UMa). They both built for typical usage scenarios for elevation beam-forming and FD-MIMO. Both scenarios are considered to be densely populated by buildings and homogeneous in nature- in terms of height and building density. These channel models are applicable to carrier frequencies between 2-6 GHz with up to 100 MHz of bandwidth [17–19].

2.2 Ray Tracing method

Ray tracing is a method for calculating the path of waves or particles through a system with regions of varying propagation velocity absorption characteristics and reflecting surfaces. To do so, RT works by assuming that a particle or wave can be modeled as a narrow beam called *ray*. This leads to the derivation of the concept of ray which can be defined as a line showing the direction of a wave and is perpendicular to the wavefront (in Section 3.1 the mathematical derivation of ray concept is presented). A ray under such circumstances can be reflected, transmitted and diffracted (with some extensions of Geometrical Optics (GO)). Initially applied to optical propagation problems, in the early 1990s RT have been applied to radio frequencies for field prediction in indoor or outdoor environments [20].

When applied to electromagnetic radiation, RT relies on an approximate solution of the Maxwell's equations using GO assumption. Strictly speaking, provided a geometrical description of a scenario, an RT algorithm can provide estimates of path loss, angle of arrival/departure and time delays [6], [20]. In Fig. 2.1, an example of a RT software output is shown where the rays connecting transmitter (TX) and receiver (RX) are highlighted.

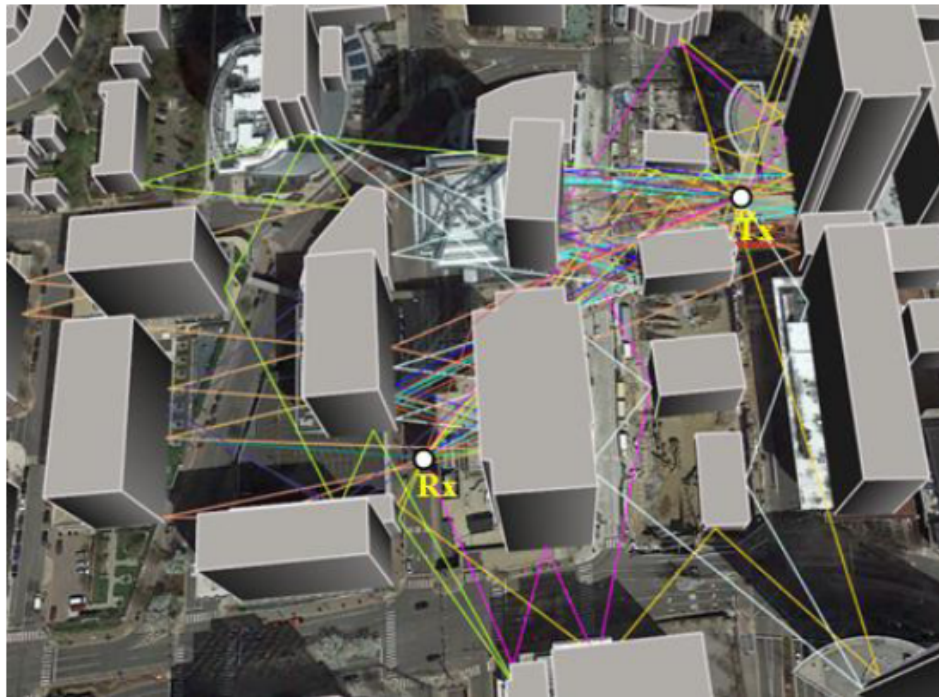


Figure 2.1: Ray tracing in an urban environment. (Source [6])

2.3 Dynamic environments

With the advent of mmWave and vehicular communications (V2V), the radio channel will become more and more dynamic: line-of-sight (LoS) and non line-of-sight (NLoS) transitions will become more abrupt due to the lower diffraction contributions and Doppler shifts will increase proportionally to the carrier frequency. In addition, due to the large variety of possible environment and system configurations, accurate deterministic propagation models are essential for the design, deployment and simulation of future communication networks. These simulations can be done by performing RT runs at every time instant. However, as we mentioned in the previous sections, RT algorithms are very precise but introduce a high level of time complexity, which would require a huge CPU time.

The future frontier in RT modeling is the actual "ahead-of-time" prediction of the multipath, and therefore of the channel characteristics in dynamic environments. More recently, fast RT algorithms have been proposed for real-time application in dynamic environments, including estimation of the optimum beam in beam-steering application for multi-antenna wireless systems [21] or the estimation of the channel state information in vehicular communications [22].

However, this is not the only option as fully deterministic and dynamic RT (DRT) are starting to gain interest in the last few years and are considered in this work. At present research in the field is still at its early stage [3, 4, 23, 24]. Deterministic DRT algorithms allows to get more physical insights of high dynamic channels enabling to obtain statistical quantities thanks to simulations as shown in [25].

Furthermore, V2V and mmWave communication channels due to their dynamic behaviour, introduce some propagation problematics compared to the well-known mobile wireless communication channels [26]. In V2V, TX and RX as well as many moving objects are moving. Measurements have shown that the shadowing due to a moving object or vehicle can go up to 15-20 dB especially if the vehicle is obstructing the LoS [27], [28]. This effect highlights the need to add these obstacles into the environment description .

Another important feature in highly dynamic environments is the increase of the Doppler frequency shift due to the speeds of the terminals and vehicles, as well as the high carrier frequencies. In DRT approach, for each ray the Doppler shift can be derived with simple analytical formulas over a period of time in which the overall multipath structure of the environment doesn't change [3], [4]. This concept and the derivation of the Doppler shift has been considered in this work and will be explained in more detail in the Chapter 4. Similar approach though has been presented in [15] and [29] where ray-based propagation models were applied to vehicular propagation with moving terminals and scatterers. In such investigations however the fact that reflection and diffraction points can actually slide over the obstacles' surfaces in a moving scene is disregarded. The sliding of interaction points has been presented in [3] and shows why this is important in short-range applications with large obstacles such as buses or when specular reflection from smooth walls is considered. Further analytical equations and formulas regarding this approach are part of this work and are presented in Chapter 4.

2.4 Summary of Ray Tracing

To summarize, RT method is based on ray optics which solve the Maxwell's equations in high frequency regime. This method and deterministic methods in general,

tend to be very accurate but their high computational complexity in certain environments can make this method impractical. This is the case of highly dynamic environments such as V2V or mmWaves communications in which RT simulations should be performed at every instant but it would require a huge CPU time. To tackle the dynamic limitation of RT, DRT will be used in this work and presented in Chapter 4. In this work are taken into account the sliding of the interaction point as well as the effect of shadowing from moving objects.

Chapter 3

Ray Tracing theory

In this chapter the objective is to gather all the physical equations representing the concept of ray widely used in RT algorithms.

In the first section, ray concept is derived solving Maxwell's equations using GO assumptions. Next the propagation mechanisms (reflection and diffraction) are explored.

3.1 Solving Maxwell's equations using GO assumptions

Maxwell's equations are a set of coupled partial differential equations that form the foundation of classical electromagnetism, classical optics, and electric circuits. They describe how charges and currents behave as sources and how time variant electric or magnetic field generate its correspondent [12]. In free space for time-harmonic fields, Maxwell's equations are:

$$\nabla \times \bar{E}(\bar{r}, \omega) + j\omega\mu\bar{H}(\bar{r}, \omega) = 0 \quad (3.1)$$

$$\nabla \times \bar{H}(\bar{r}, \omega) + j\omega\epsilon\bar{E}(\bar{r}, \omega) = 0 \quad (3.2)$$

$$\nabla \cdot \bar{E}(\bar{r}, \omega) = 0 \quad (3.3)$$

$$\nabla \cdot \bar{H}(\bar{r}, \omega) = 0 \quad (3.4)$$

where $\bar{E}(\bar{r}, \omega)$ and $\bar{H}(\bar{r}, \omega)$ are the electric and magnetic field vectors. The vector \bar{r} is the position vector, ω is the pulsation, $\epsilon = \epsilon_0\epsilon_r$ and $\mu = \mu_0\mu_r$ are respectively the permittivity and permeability of the medium in free space. In a wireless propagation

context $\mu = \mu_0$ as we deal with non-magnetic media. From equation (3.1) and (3.2) we can obtain:

$$\nabla^2 \bar{E}(\bar{r}, \omega) + k^2 \bar{E}(\bar{r}, \omega) = 0, \quad (3.5)$$

which is known as the Helmholtz equation. In (3.5), $k = \omega \sqrt{\mu_0 \epsilon}$ is the wavenumber [12]. In a similar way we derive the equation for the magnetic field \bar{H} .

EM problems should be studied by solving Maxwell's equations applying ad-hoc initial and boundary conditions, but only in few cases they can be solved exactly [30]. The *Luneburg – Kline* asymptotic approximation is a bridge between GO and wave propagation [31], [32]. In an isotropic medium source-free it can be written as [33]:

$$\bar{E}(\bar{r}, \omega) \sim e^{-jk\Psi(\bar{r})} \sum_{m=0}^{+\infty} \frac{\bar{E}_m(\bar{r})}{(j\omega)^m} \quad (3.6)$$

$$\bar{H}(\bar{r}, \omega) \sim e^{-jk\Psi(\bar{r})} \sum_{m=0}^{+\infty} \frac{\bar{H}_m(\bar{r})}{(j\omega)^m} \quad (3.7)$$

where $\Psi(\bar{r})$ is the phase function, and \sim means equal in asymptotic sense. In an ideal scenario that frequency tends to infinite, the only significant term is the one for $n = 0$ which it is called GO field:

$$\lim_{\omega \rightarrow +\infty} \bar{E}(\bar{r}, \omega) = e^{-jk\Psi(\bar{r})} \bar{E}_0(\bar{r}) \quad (3.8)$$

By mathematical manipulation of equation (3.8) [33], we can obtain the eikonal equation

$$|\nabla \Psi(\bar{r})| = 1 \quad (3.9)$$

which has at least three solutions, that are planar, spherical and cylindrical surfaces.

The Poynting vector

$$\bar{S} = \bar{E} \times \bar{H} \quad (3.10)$$

expresses the magnitude and direction of the flow of energy in electromagnetic waves. If applied to the GO fields, it is possible to derive

$$\hat{s} = \nabla \Psi \quad (3.11)$$

that is the direction of propagation of a GO ray. In Fig. 3.1 is represented a narrow astigmatic ray tube (an infinitesimally narrow tube surrounding a central ray of direction \hat{s}). Corresponding with 0 and s (see Fig 3.1) there are the equiphase

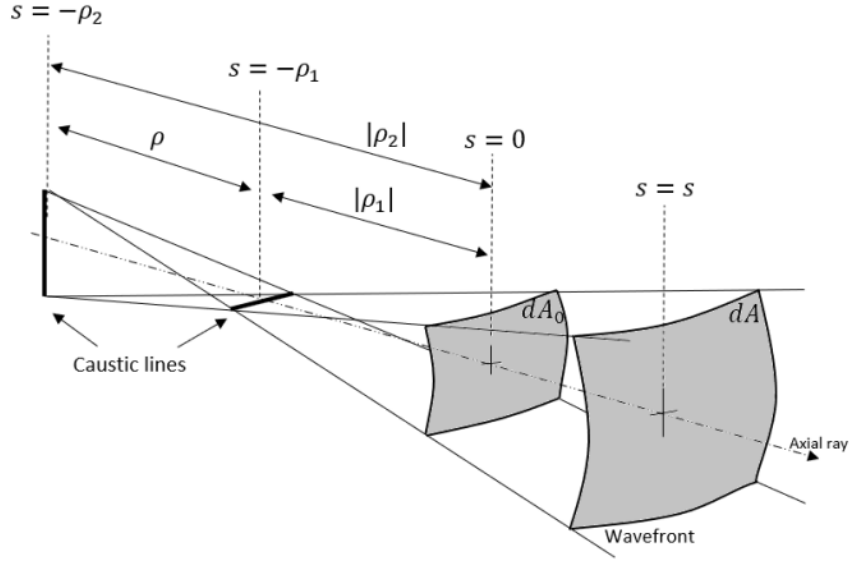


Figure 3.1: Narrow astigmatic ray tube. (Source [31])

surfaces $\Psi(0)$ and $\Psi(s)$, respectively. The reference surface $\Psi(0)$ has ρ_1 and ρ_2 as radii of curvature. If the medium is homogeneous where the rays are rectilinear, the phase along the path is [33]:

$$e^{-jk\Psi(s)} = e^{-jk\Psi(0)} e^{-jks} \quad (3.12)$$

In a similar way, the expression of amplitude continuation is

$$\bar{E}(s) = \bar{E}(0) \sqrt{\frac{\rho_1 \rho_2}{(\rho_1 + s)(\rho_2 + s)}} e^{-jks} \quad (3.13)$$

with $\bar{E}(0)$ is the field at reference point $s = 0$ and e^{-jks} represents the phase factor.

Meanwhile the factor:

$$A(s) = \sqrt{\frac{\rho_1 \rho_2}{(\rho_1 + s)(\rho_2 + s)}} \quad (3.14)$$

is called the *spreading factor* (or divergence factor).

When particular cases are considered equation (3.13) is simplified:

1. If the assumption of a plane wave is made, the radii of curvature ρ_1 and ρ_2 tend to infinite and as a consequence $A(s) \rightarrow 1$. In this case GO field can be written as:

$$\bar{E}(s) = \bar{E}(0) e^{-jks} \quad (3.15)$$

2. When spherical wave is considered then, $\rho_1 = \rho_2 = \rho$. In this case the GO field is reduced to

$$\bar{E}(s) = \bar{E}(0) \frac{\rho}{\rho + s} e^{-jks} \quad (3.16)$$

3. In terms of cylindrical waves, one of the radii of curvature tend to infinite (for example $\rho_1 \rightarrow \infty$, $\rho_2 = \rho$):

$$\bar{E}(s) = \bar{E}(0) \sqrt{\frac{\rho}{\rho + s}} e^{-jks} \quad (3.17)$$

The before-mentioned equations describe only LoS wave propagation. Other contributions such as reflections and transmissions require modification of such expressions.

3.2 Reflection

If a ray is reflected (transmitted) one or more times before reaching the field point, the ray is called a reflected (transmitted) ray [6]. This ray corresponds to the reflection (transmission) of EM waves at interfaces between different mediums (see Fig. 3.2). The incident ray trajectory is modified according to the *Snell's laws of reflection/transmission*. Reflected rays and wavefront are as if the reflected wave were generated at the source image point.

Law of reflection Incident and reflected rays, as well as the normal to the interface, lie in the same plane, called *plane of incidence*. Incident and reflected angles, measured with respect to the normal, are equal (and lie on opposite sides of the normal):

$$\theta_i = \theta_r \quad (3.18)$$

where θ_i is the incidence angle and θ_r is the reflected ray angle [31].

Fresnel coefficients The law of reflection determines the propagation direction of the reflected (transmitted) ray. The magnitude of the reflected field is determined by the *Fresnel's* equations for different polarizations. The Fresnel coefficients

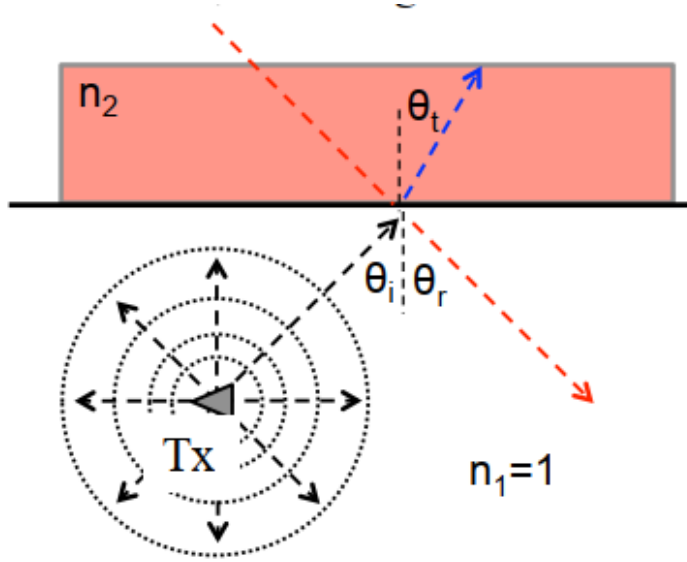


Figure 3.2: Example of reflected and transmitted ray with two different mediums represented by the refractive indices n_1 and n_2

for the parallel and perpendicular components are:

$$\Gamma_{\parallel} = \frac{\epsilon_e \cos \theta_i - \sqrt{\epsilon_e \sin^2 \theta_i}}{\epsilon_e \cos \theta_i + \sqrt{\epsilon_e \sin^2 \theta_i}} \quad (3.19)$$

$$\Gamma_{\perp} = \frac{\cos \theta_i - \sqrt{\epsilon_e \sin^2 \theta_i}}{\cos \theta_i + \sqrt{\epsilon_e \sin^2 \theta_i}} \quad (3.20)$$

where $\epsilon_e = \epsilon - \frac{j\sigma}{\omega}$ is the effective permittivity.

Finally the reflected field at a distance s from the point of reflection (Q_R) is:

$$E_r(s) = E_i(Q_R) \cdot \bar{\bar{R}} \sqrt{\frac{\rho_1 \rho_2}{(\rho_1 + s)(\rho_2 + s)}} e^{-jks} \quad (3.21)$$

where $\bar{\bar{R}} = \begin{bmatrix} \Gamma_{\perp} & 0 \\ 0 & \Gamma_{\parallel} \end{bmatrix}$ is the depolarization matrix for reflection coefficients.

Similar calculations can be conducted even for the transmitted field but in this work the transmissions will not be considered.

3.3 Diffuse scattering

Another propagation mechanism is the *diffuse scattering* from rough surfaces such as building facades [6]. In urban scenarios, the ray concept can still be used by incorporating the effect of scattering or defuse from these objects [34]. The scattering

from buildings can be split into specular and nonspecular components [35]. In [16], the importance of incorporating the diffuse scattering effect is validated by comparing the ray tracing simulated results with the measurement. The effective roughness concept is proposed in [36] and [37] for the calculation of scattered power from building facades. Recent developments for modeling diffuse scattering of urban environments using ray tracing can be found in [38].

In this work the used pattern associated with the effective roughness scattering model is the *Lambertian model*. The amplitude of the scattered field from a surface element is :

$$E_s^2 = K_0^2 S^2 \Gamma^2 \frac{dS \cos \theta_i \cos \theta_s}{\pi} \frac{1}{r_i^2 r_s^2} \quad (3.22)$$

where K_0 is a coefficient depending on the gain of the transmitting antenna and the transmitted power, Γ is the reflecting coefficient, θ_i is the angle of incidence and θ_s is the angle of scattering direction. S is the scattering coefficient.

3.4 Diffraction from an edge

In the study of wave propagation in the presence of dielectric objects, reflection and transmission might not be sufficient to predict correctly the EM field distribution. For this reason, another wave propagation mechanism should be considered that is the diffraction by an edge, for which the GO must be extended.

If we consider an edge and an EM field source near it, GO for such geometry divides the space around the edge into three regions [33]:

1. Region I with only direct and reflected rays
2. Region II with only direct rays
3. Region III no rays

Therefore in the resultant EM field, there will be discontinuities in the boundaries between the regions (Reflection Shadow Boundary between I and II and Incident Shadow Boundary between II and III) (see Fig. 3.3). To eliminate these discontinuities between these regions, it has to be included the diffraction field.

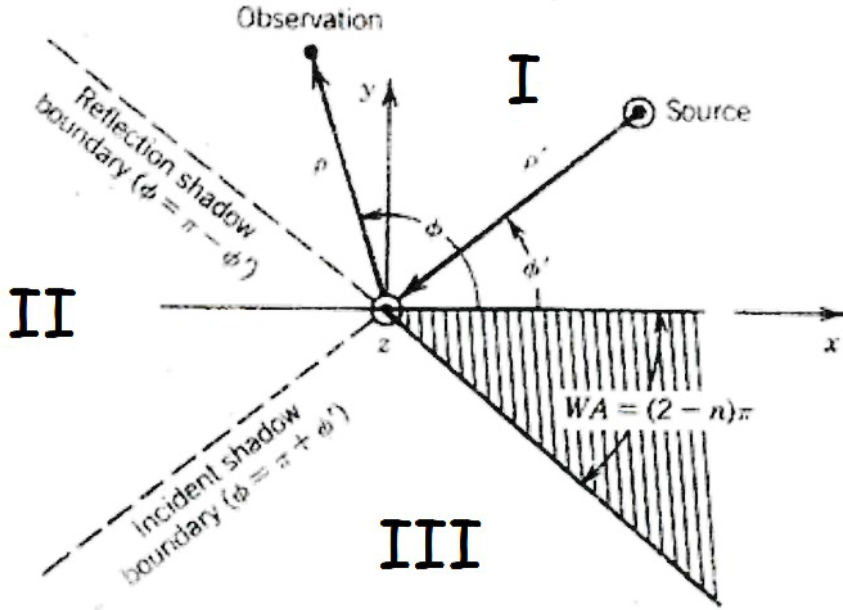


Figure 3.3: Geometry for diffraction by an edge

3.4.1 Geometrical theory of diffraction

The first extension of GO taking into consideration the diffraction field, was presented by Keller in 1953 [39] and published in 1962 [40]. The position of the diffraction point on the edge can be found by using the Keller's law of diffraction:

"A diffracted ray and the corresponding incident ray make equal angles with the edge at the point of diffraction, provided they are in the same medium. They lie on opposite sides of the plane normal to the edge at the point of diffraction" [33].

This means that for every incident ray forming an angle $\beta_{0,inc}$ with the edge is equal to the $\beta_{0,diff}$ between the diffracted ray and the edge:

$$\beta_{0,inc} = \beta_{0,diff} = \beta_0 \quad (3.23)$$

Between the incident ray and the corresponding diffracted one, according to the law of diffraction, there exists a relation which gives us the position of the diffraction point:

$$\sin \beta_0 = |\hat{s}_i \times \hat{t}| = |\hat{s}_d \times \hat{t}| \quad (3.24)$$

with \hat{t} the unit vector tangent to the edge, \hat{s}_i and \hat{s}_d are the unit vectors related with the direction of propagation of the incident and diffracted rays, respectively. An example is shown in Fig. 3.4

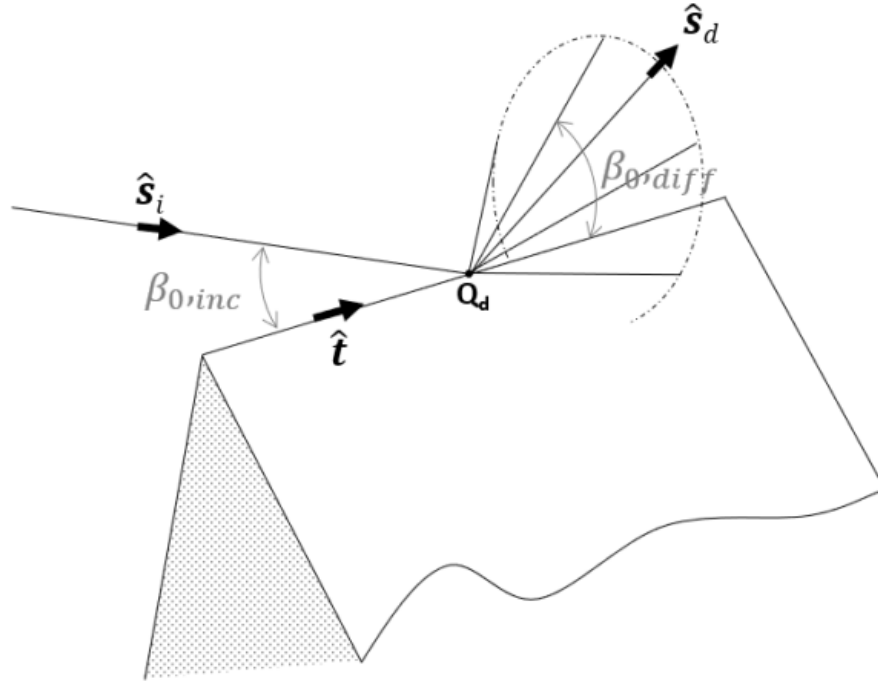


Figure 3.4: Diffracted rays cone (Source [31])

The main drawback of Geometrical Theory of Diffraction (GTD) is linked to not having considered the radius of curvature of the surface that generates the diffracted field. Therefore, GTD improves the prediction of the diffracted field but becomes singular in the transition regions surrounding the shadow boundaries. The Uniform Theory of Diffraction (UTD) solves this problem by adding a transition function which keeps the value of the diffracted field finite.

3.4.2 Uniform theory of diffraction

In 1974, Kouyoumjian and Pathak presents the UTD and prove that by introducing a transition function and multiplying it with diffraction coefficient, we can achieve a finite value of the diffraction field even in the surrounding of the *shadow boundaries*.

At this point, the UTD diffracted field can be calculated. If we consider an edge-fixed coordinate system, the incident field can be divided into $\hat{\beta}_0$ and ξ components, where ξ is the angle between one the two faces of the edge, taken as a reference and

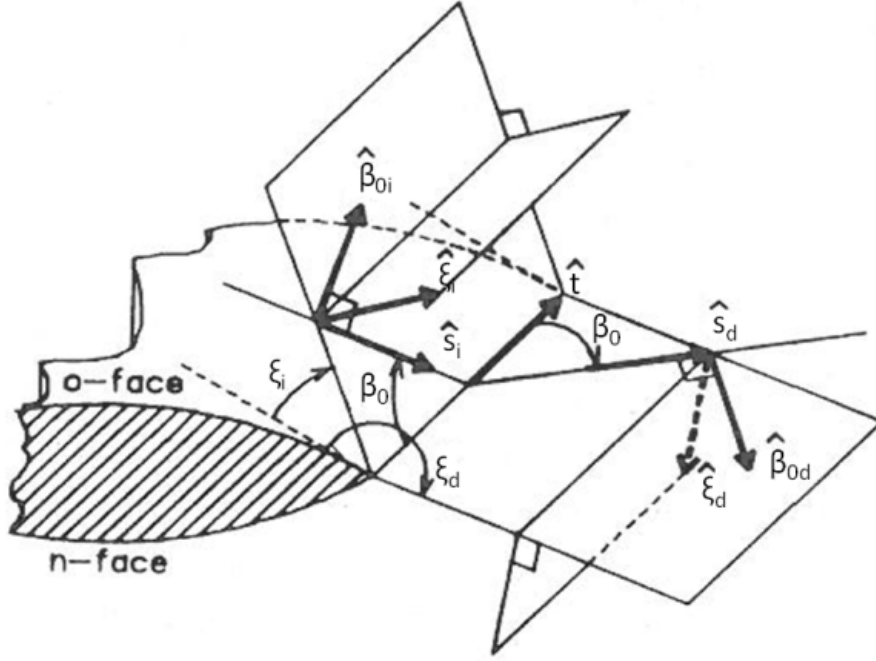


Figure 3.5: Edge-fixed coordination geometry [33]

called "o-face", and the considered ray. $\hat{\beta}_0$ and $\hat{\xi}$ can be evaluated as:

$$\hat{\xi}_i = \frac{\hat{s}_i \times \hat{t}}{|\hat{s}_i \times \hat{t}|} \quad (3.25)$$

$$\hat{\xi}_d = \frac{\hat{t} \times \hat{s}_d}{|\hat{t} \times \hat{s}_d|} \quad (3.26)$$

$$\hat{\beta}_{0,i} = \hat{\xi}_i \times \hat{s}_i \quad (3.27)$$

$$\hat{\beta}_{0,d} = \hat{\xi}_d \times \hat{s}_d \quad (3.28)$$

An example of an edge-fixed coordinates geometry is shown in Fig 3.5.

If we consider spherical waves, the UTD diffracted field at a distance s' from the point of diffraction (Q_D) is given by [32], [41]:

$$\bar{E}_d(s') = \bar{E}_i(Q_D) \bar{D} \sqrt{\frac{s}{s'(s+s')}} e^{-jks'} \quad (3.29)$$

with s being the distance travelled by the incident ray from its reference to the diffraction point. The dyadic UTD diffraction coefficient \bar{D} is:

$$\bar{D} = -\hat{\beta}_{0,i}\hat{\beta}_{0,d}D_\beta - \hat{\xi}_i\hat{\xi}_dD_\xi \quad (3.30)$$

where

$$D_\beta = D_1 + D_2 + R_{\parallel}(D_3 + D_4) \quad (3.31)$$

$$D_\xi = D_1 + D_2 + R_{\perp}(D_3 + D_4) \quad (3.32)$$

the four items that form the diffraction coefficients can be calculated in the following way:

$$D_1 = \frac{-e^{-j\pi/4}}{2n\sqrt{2\pi k} \sin \beta_0} \cot \left(\frac{\pi + (\xi_d - \xi_i)}{2n} \right) F(kLa^+(\xi_d - \xi_i)) \quad (3.33)$$

$$D_2 = \frac{-e^{-j\pi/4}}{2n\sqrt{2\pi k} \sin \beta_0} \cot \left(\frac{\pi - (\xi_d - \xi_i)}{2n} \right) F(kLa^-(\xi_d - \xi_i)) \quad (3.34)$$

$$D_3 = \frac{-e^{-j\pi/4}}{2n\sqrt{2\pi k} \sin \beta_0} \cot \left(\frac{\pi + (\xi_d + \xi_i)}{2n} \right) F(kLa^+(\xi_d + \xi_i)) \quad (3.35)$$

$$D_4 = \frac{-e^{-j\pi/4}}{2n\sqrt{2\pi k} \sin \beta_0} \cot \left(\frac{\pi - (\xi_d + \xi_i)}{2n} \right) F(kLa^-(\xi_d + \xi_i)) \quad (3.36)$$

Functions a^\pm are defined as

$$a^\pm(\xi_d \pm \xi_i) = 2 \cos^2 \left(\frac{2n\pi N^\pm - (\xi_d \pm \xi_i)}{2} \right) \quad (3.37)$$

where N^\pm are the integer that most nearly satisfy the equation:

$$2n\pi N^\pm - (\xi_d \pm \xi_i) = \pm\pi \quad (3.38)$$

$F(x)$ is the transition function that forces GTD diffracted fields to remain bounded across the shadow boundaries, as it goes zero in the same way as the GTD diffraction coefficients become singular:

$$F(x) = 2j\sqrt{x}e^{jx} \int_{\sqrt{x}}^{\infty} e^{-ju^2} du \quad (3.39)$$

Finally the parameter L , for a spherical wavefront, is:

$$L = \frac{s' s}{s' + s} \quad (3.40)$$

Chapter 4

Dynamic Ray Tracing

4.1 The DRT concept

A single multi-bounce ray path can be represented as a polygonal chain where TX, the interaction points (e.g. reflection points or diffraction points) and RX are defined as the vertexes of the chain (see Fig. 4.1). The evolution of this chain in a dynamic environment can be described only if we know how its vertexes will move in time. While the motion of the terminals is independent, the motion of the interaction points depends on the motion of the terminals and of objects generating these interaction points as well as on their instantaneous positions. Furthermore, the motion of the interaction points is not constant even if the terminals motion is constant.

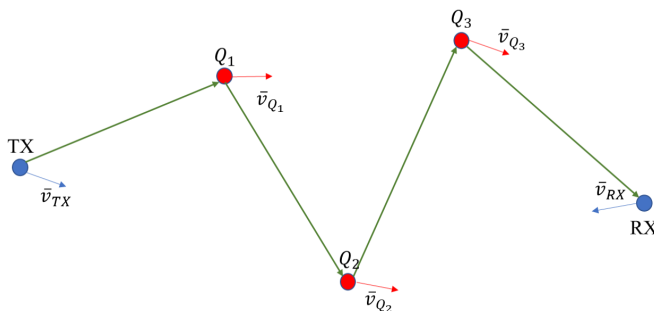


Figure 4.1: Representation of single multi-bounce ray path.

The computation of the dynamic evolution of paths can of course be accomplished by multiple RT runs on multiple environment descriptions corresponding to successive "snapshots" of the environment in time. Nonetheless, this technique

requires the creation of a very large number of environment databases as well as an equally large number of RT runs making it impractical if an accurate description is required and moreover it will require a huge CPU time.

The proposed DRT algorithm is based on the combination of a classical 3D image-based RT approach with an analytical extrapolation of multipath evolution using a proper description of the dynamic environment [3], [4]. A dynamic environment database is introduced that describes the geometry of the environment also including the motion characteristics of both the radio terminals and the rigid bodies that can move, such as vehicles or machines. The database is divided into two parts. The first one provides a geometrical description of the environment for a given time instant t_0 . Objects are described here - as in most RT models - as polyhedrons with flat surfaces and right edges, although an extension to curved surfaces is possible. In the second part, the dynamic parameters of every terminal and object are provided. In particular, the objects are modelled as "rigid bodies" with a roto-translational motion, that can be described in a complete way by providing translation velocity, rotation axis, angular velocity and the corresponding accelerations.

A traditional RT prediction is carried out for the initial time t_0 , then the positions of all interaction points are extracted. From the initial positions, the motion of each vertex of the chain within T_C must be computed. Our assumption is that the complete motion of the radio terminals is a-priori known. If this is not true, we assume at least that the the terminals' instant velocity and acceleration at t_0 is known, so that the positions $\bar{r}_P(t)$ of TX or RX on a time instant $t = t_0 + \Delta t$ can be calculated using the Taylor series formula:

$$\begin{aligned} \bar{r}_P(t_0 + \Delta t) = \bar{r}_P(t_0) + \bar{v}_P(t_0)\Delta t + \\ \frac{1}{2}\bar{a}_P(t_0)\Delta t^2 + O(\Delta t^3) \end{aligned} \tag{4.1}$$

where $\bar{v}_P(t_0)$ and $\bar{a}_P(t_0)$ are the velocity and acceleration of P, respectively, at t_0 , and the symbol $O(\Delta t^3)$ means that all the variations higher than 2^{nd} order, i.e. variations of accelerations, are neglected.

Now the problem is that the interaction points' positions, velocities and accelerations is unknown and needs to be determined for every time instant $t_0 + \Delta t$ on the base of the current positions, velocities and accelerations of TX, RX and of the obstacles generating such interactions. For this purpose, we developed closed form

formulas as explained in Section 4.2.

The analytical extrapolation procedure is valid as long as the multipath structure remains the same, i.e., no path disappears and no new path appears to significantly change such structure. This time interval will be referred to in the following as *multipath lifetime* (T_C). As long as $\Delta t < T_C$, DRT allows to extrapolate the multipath - and therefore the total field, the time-variant channel's transfer function, Doppler's shift frequencies, time delays, etc. - for every time instant $t_0 + \Delta t$ without re-running the RT engine, and therefore at only a fraction of the computation time. In fact, the computationally most expensive part of a RT algorithm consists in determining the geometry of the rays, which requires checking the visibility and obstructions between all objects in the database, in order to establish the existence of each of the traced rays. With the DRT approach, this is done only once at time t_0 , while in the subsequent time instants within T_C we rely on analytical prolongation of the same rays, which is computationally much faster.

Also, we believe that it is a reasonable assumption to neglect the temporal variations of acceleration during the time T_C , in accordance with eq. (4.1): in fact, in vehicular scenarios the multipath structure usually varies on a faster time scale than acceleration, as discussed in later sections.

4.2 DRT algorithm description

The DRT algorithm is based on a classical 3D image based RT approach and an analytical continuation in a fully dynamic environment [3], [4]. In order to extract the geometry of a ray, one should be able to track the motion of every interaction points constituting the ray. To do so, the position and velocity of the terminals and objects should be known. These quantities can be stored in a database containing a description of the environment at any moment.

The dynamic environment database is divided into two parts, i.e., environment database and dynamic database. In Fig. 4.2 is shown an example of how the dynamic environment database is composed. As in a RT database, the environment database is composed of two files, **.data* file and **.list* file. The first file provides a geometrical description of the environment for a given time instant t_0 in which the

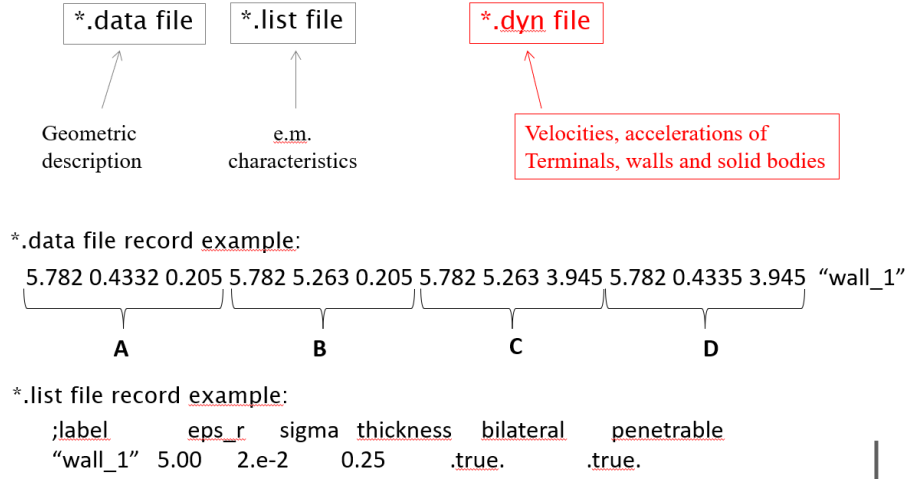


Figure 4.2: Example of the composition of the dynamic environment database

objects are described as polyhedrons with right flat surfaces and right edges. While the second provides the EM characteristics for every plane present in **.data* file.

The difference with the environment database used in RT simulation is the dynamic database composed by **.dyn* file. In our considered environment any object can have a roto-translational motion. In the dynamic database are provided the dynamic parameters of every object. Generally, for the terminals, only position, velocity and acceleration vectors are necessary, meanwhile for the moving objects the angular velocity is needed. In Fig. 4.3 is shown in detail the composition of **.dyn* file.

After obtaining all these information, then, from a single RT run in time t_0 , the positions of all interaction points are extracted, including reflection, scattering and diffraction points. Subsequently, defined T_C as the *multipath lifetime* of the channel, i.e. the time during which the accelerations are constant and the multipath macrostructure remains unchanged, DRT allows to extrapolate a complete prediction for every time instant within $[t_0, t_0 + T_C]$ without re-running the RT engine. T_C being an important parameter of the DRT simulation, depends not only on the multipath changes but also on the link distance between the terminals and the dynamic characteristics of terminals and objects present in the scenario.

DRT includes the time and space domain channel characteristics as well as Doppler frequency information. Since DRT accounts for speeds and accelerations, Doppler information is derived in closed form, without resorting to finite-difference

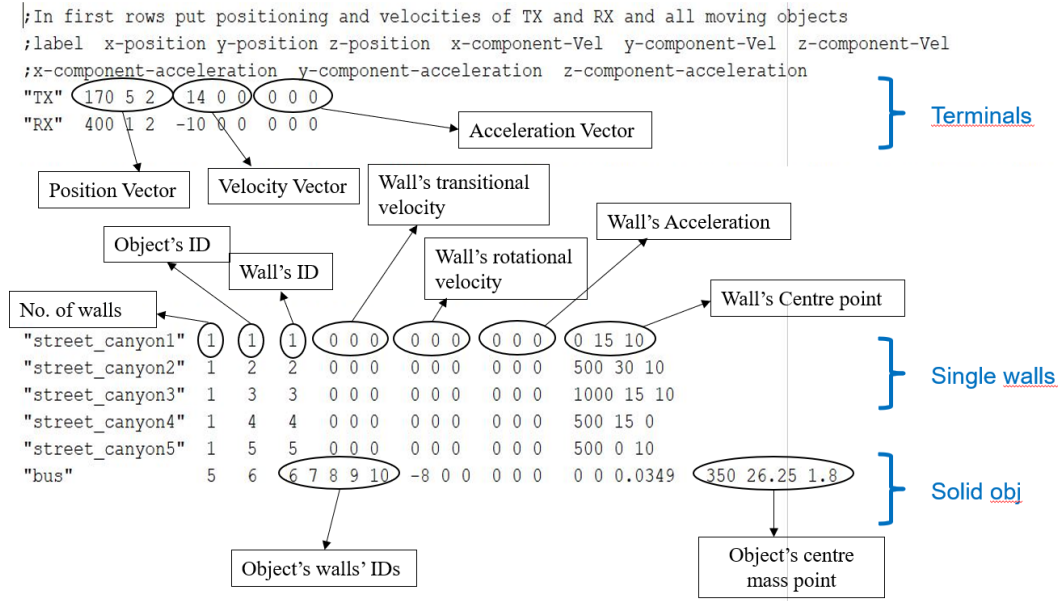


Figure 4.3: Example of the dynamic database

computation. A more detailed explanation about Doppler frequency calculation is described in Appendix A.

In the following sections, the DRT algorithm formulation is described for single and multiple bounce rays, including specular reflection and edge diffraction, based on the outcome of a single RT simulation at the initial time t_0 , and on the knowledge of the dynamic parameters of TX/RX, and of the objects in the propagation environment.

4.2.1 Reflection points' calculation

DRT algorithm performs a RT simulation for the environment at the initial time t_0 , and then by applying analytical formulas is able to track the motion of the reflection points, i.e. to compute their position, velocity, and acceleration, at any time instant after t_0 which falls within the multipath lifetime.

4.2.1.1 Single reflection calculation

A simple case is considered with a reflecting wall laying on a plane Π^I , and transmitter (TX) and receiver (RX) located at different distances from Π^I . As a start, we consider the case where TX and RX move with instantaneous speeds \bar{v}_{TX} and \bar{v}_{RX} , while the reflecting wall is at rest. Without loss of generality, we can assume

a proper reference system so that the wall lies on the plane of equation $y = 0$, while TX and RX lie on the xy plane. Then, by using the image method and through simple geometric considerations we can derive the reflection point position (Q_R) at the considered time instant, which is located at the intersection between the reflecting plane and the line passing through RX and the image of TX:

$$\begin{cases} x_{Q_R}(t) = x_{TX}(t) + \frac{x_{RX}(t) - x_{TX}(t)}{y_{RX}(t) + y_{TX}(t)} y_{TX}(t) \\ y_{Q_R}(t) = 0 \\ z_{Q_R}(t) = z_{TX}(t) + \frac{z_{RX}(t) - z_{TX}(t)}{y_{RX}(t) + y_{TX}(t)} y_{TX}(t) \end{cases} \quad (4.2)$$

When TX/RX move with a certain speed, the corresponding reflection point "slides" along the plane surface: therefore, by deriving Q_R coordinates with respect to time, the instantaneous velocity of the reflection point ($\bar{v}_{Q_R} = v_{Q_{R,x}} \hat{x} + v_{Q_{R,z}} \hat{z}$) can be determined, by using the derivative chain rule.

For example, the x-component of \bar{v}_{Q_R} is:

$$\begin{aligned} v_{Q_{R,x}} = \frac{\partial x_{Q_R}}{\partial t} &= \frac{\partial x_{Q_R}}{\partial x_{TX}} v_{TX,x} + \frac{\partial x_{Q_R}}{\partial y_{TX}} v_{TX,y} \\ &+ \frac{\partial x_{Q_R}}{\partial x_{RX}} v_{RX,x} + \frac{\partial x_{Q_R}}{\partial y_{RX}} v_{RX,y}. \end{aligned} \quad (4.3)$$

The closed-form expressions of the derivatives in eq. (4.3) are reported in Appendix B.

This approach is similar to the one adopted in [24], but in the following it will be extended to a more general case, where the reflecting wall has a roto-translational motion, and TX, RX, and the reflecting wall can vary their velocities during time, so their motion is accelerated. The basic idea is to use a local reference system integral with the wall (local frame) so that we can resort to the previous case where the wall is at rest and apply equations (4.2) and (4.3) again, as shown below.

Moreover, in the present work we make a complete characterization of the reflection point motion, including acceleration: in fact, except very particular cases, Q_R velocity is not constant in time, i.e. the reflection point has an accelerated motion. Therefore, with a similar method as in (4.3), the acceleration of the reflection point ($\bar{a}_{Q_R} = a_{Q_{R,x}} \hat{x} + a_{Q_{R,z}} \hat{z}$) can be calculated by deriving \bar{v}_{Q_R} with respect to time. For instance, the x-component of the acceleration will be:

$$a_{Q_{R,x}} = \frac{\partial v_{Q_{R,x}}}{\partial t} = \frac{\partial}{\partial t} \frac{\partial x_{Q_R}}{\partial t} \quad (4.4)$$

The complete expression of \bar{a}_{Q_R} , and the detailed computation of \bar{v}_{Q_R} and \bar{a}_{Q_R} are presented in Appendix B.

In Fig. 4.4, an example of a single reflection scenario is presented. For the sake of simplicity, we refer to a bi-dimensional case where TX/RX are located in a horizontal plane $z = z_0$ and moving with arbitrary speeds, meanwhile the reflecting wall is located along a vertical plane $y = y_0$, and is then represented with a straight line. Moreover, the wall rotates around a vertical axis, and the intersection of the rotation axis with the plane $z = z_0$ provides the rotation center O^I . The local reference system $O^I x^I y^I z^I$ centered in O^I (local frame), is also represented in the figure. The axes of the local frame are oriented so that at each time instant the reflecting wall is laying on the $z^I x^I$ plane of equation $y = 0$, in order to apply eq. (4.2). The scenario represented in the figure is simplified for ease of readability, but the presented method is general, so the TX/RX positions and velocities, the wall plane and the rotation axis can be arbitrarily oriented with respect to the global reference system $Oxyz$.

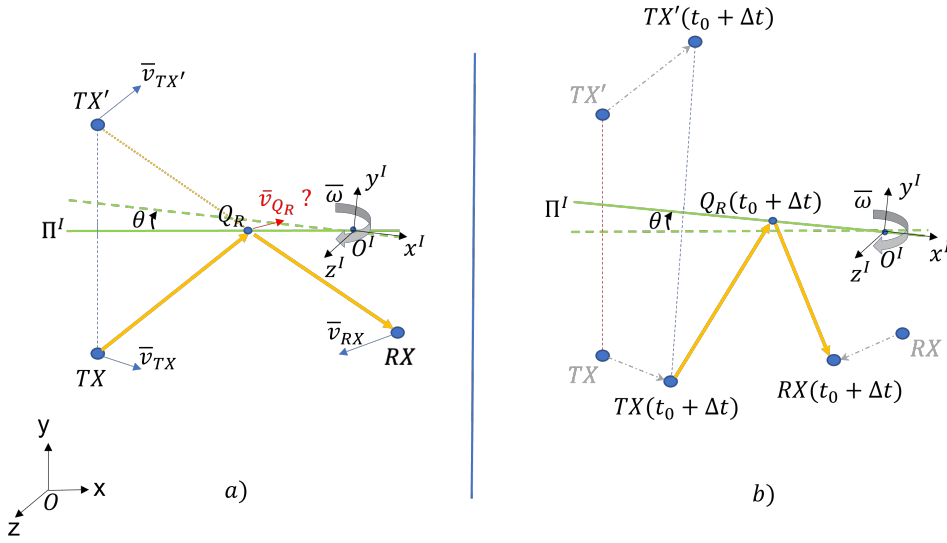


Figure 4.4: Example of a single reflection scenario with the plane Π^I that rotates w.r.t. to the global frame. a) Scenario at $t = t_0$ and instantaneous velocities of TX, image-TX, RX, and reflection point Q_R . b) Scenario at $t = t_0 + \Delta t$.

Fig. 4.4a) shows the configuration of the system at a certain time $t = t_0$, when the wall plane Π^I is parallel to the plane xz of the global frame $Oxyz$. The instantaneous velocities of TX (\bar{v}_{TX}), image-TX ($\bar{v}_{TX'}$), reflection point (\bar{v}_{Q_R}) and RX (\bar{v}_{RX}) at

$t = t_0$ are depicted as well. The instantaneous angular velocity of the wall plane is expressed by the vector $\bar{\omega} = \omega \hat{k}$, where $\omega = \frac{d\alpha}{dt}$ is the scalar angular velocity, and \hat{k} is a unit vector parallel to the rotation axis, and properly oriented according to the right-hand rule. In the example of Fig. 4.4, we have $\hat{k} = -\hat{z}^I$, as the wall is rotating clockwise around the z -axis of the local frame.

Fig. 4.4b) shows the configuration of the system in a subsequent time instant $t = t_0 + \Delta t$, when the wall plane has rotated clockwise by an angle θ , and TX/RX have moved to different positions: the result of this motion is a shift of the reflection point Q_R along the reflecting wall.

In Fig. 4.4 a wall rotating around a fixed rotation axis is shown, but in general, a translational motion of the wall plane can be also present, in addition to the rotational motion. In the general case of roto-translational motion, any point Q of the wall will have a different speed, given by [42]:

$$\bar{v}_Q = \bar{v}_{\Pi^I} + \bar{\omega} \times \overline{O^I Q} \quad (4.5)$$

where the symbol "×" stands for the cross vector product, \bar{v}_{Π^I} is the translation velocity, common to all the points of the plane, and $\overline{O^I Q}$ is the position vector of the considered point Q w.r.t. the origin O^I of the local frame, positioned on the (instantaneous) rotation axis.

The first step of the DRT procedure consists in the computation of the (instantaneous) position of the reflecting point Q_R . Thanks to the adoption of the local frame, this can be accomplished through eq. (4.2), but in order to do that, we need to transform the coordinates of TX and RX into the local frame associated with the wall. To this end, we observe that the positions of TX/RX with respect to the global and local frames are related each other through the following *coordinate transformation* [42]:

$$\begin{aligned} \bar{r}_{TX}^0(t) &= \bar{\bar{R}}(t) \cdot \bar{r}_{TX}^I(t) + \bar{r}_{0^I}(t) \\ \bar{r}_{RX}^0(t) &= \bar{\bar{R}}(t) \cdot \bar{r}_{RX}^I(t) + \bar{r}_{0^I}(t) \end{aligned} \quad (4.6)$$

with

$$\begin{aligned} \bar{r}_{TX}^0(t) &= [x_{TX}(t) \ y_{TX}(t) \ z_{TX}(t)]^T \\ \bar{r}_{RX}^0(t) &= [x_{RX}(t) \ y_{RX}(t) \ z_{RX}(t)]^T \end{aligned}$$

and

$$\begin{aligned}\bar{r}_{TX}^I(t) &= [x_{TX}^I(t) \ y_{TX}^I(t) \ z_{TX}^I(t)]^T \\ \bar{r}_{RX}^I(t) &= [x_{RX}^I(t) \ y_{RX}^I(t) \ z_{RX}^I(t)]^T\end{aligned}$$

being the position vectors of TX/RX w.r.t. the global and local frame, respectively, where $\bar{\bar{R}}(t)$ is the (instantaneous) rotation matrix and $\bar{r}_{OI}(t) = [x_{OI}(t) \ y_{OI}(t) \ z_{OI}(t)]^T$ is the position vector associated with the origin point O^I of the local frame. By inverting eq. (4.6), we can determine the positions $\bar{r}_{TX}^I, \bar{r}_{RX}^I$ of TX and RX w.r.t. to the local frame, and then apply eq. (4.2) to find the coordinates of Q_R .

In the simple example of Fig. 4.4 (clockwise rotation around the z-axis), the rotation matrix at the time instant $t = t_0 + \Delta t$ is given by:

$$\bar{\bar{R}}(t_0 + \Delta t) = \begin{pmatrix} \cos\theta & \sin\theta & 0 \\ -\sin\theta & \cos\theta & 0 \\ 0 & 0 & 1 \end{pmatrix}$$

In a generic time instant $t = t_0 + \Delta t$ within the multipath lifetime T_C , the instantaneous rotation angle $\theta(t)$ can be obtained in the following way, similarly to eq.(4.1) and neglecting time variations of angular acceleration:

$$\theta(t) = \theta(t_0) + \omega\Delta t + \frac{1}{2} \frac{d\omega}{dt} \Delta t^2$$

Of course, *coordinate transformation* must be applied to the components of $\bar{v}_{TX}, \bar{v}_{RX}$ and $\bar{a}_{TX}, \bar{a}_{RX}$ as well.

The next step of the DRT procedure consists in the computation of the velocity and acceleration of Q_R which can be obtained through eq. (4.3) and (4.4). In fact, one of the main advantages of the DRT approach is that we can derive \bar{v}_{Q_R} and \bar{a}_{Q_R} analytically, without need to resort to time differences methods. However, projecting the components of $\bar{v}_{TX}, \bar{v}_{RX}$ and $\bar{a}_{TX}, \bar{a}_{RX}$ on the local frame is not enough to apply eq. (4.3) and (4.4), which have been obtained from eq. (4.2), i.e. assuming that the reflecting wall is at rest. Since now the reflecting wall is moving, and then the local frame is in motion w.r.t. the global reference system, the velocities and accelerations of TX/RX must be preliminary transformed according to the *relative motion transformations*, to obtain "relative" velocities and accelerations w.r.t. an observer located in the origin of the local frame [43]. For instance, the velocity and

acceleration of TX must be transformed in the following way:

$$\bar{v}_{TX}^I = \bar{v}_{TX}^0 - \bar{v}_{\Pi^I} - \bar{\omega} \times \bar{r}_{TX}^I \quad (4.7)$$

$$\begin{aligned} \bar{a}_{TX}^I = \bar{a}_{TX}^0 - \bar{a}_{\Pi^I} - \dot{\bar{\omega}} \times \bar{r}_{TX}^I - 2\bar{\omega} \times \bar{v}_{TX}^I \\ - \bar{\omega} \times (\bar{\omega} \times \bar{r}_{TX}^I) \end{aligned} \quad (4.8)$$

where the headers "I" and "0" are associated with the velocities and accelerations seen by an observer located in the origin of the local and global frame, respectively, $\bar{r}_{TX}^I = \bar{r}_{TX}^0 - \bar{r}_{O^I}$ is the position vector of TX in the local frame, \bar{v}_{Π^I} , $\bar{\omega}$ are the translation and angular velocities of the wall plane Π^I , and \bar{a}_{Π^I} , $\dot{\bar{\omega}} = \frac{d\bar{\omega}}{dt}$ are the corresponding translation and angular accelerations, respectively. The terms $\dot{\bar{\omega}} \times \bar{r}_{TX}^I$, $2\bar{\omega} \times \bar{v}_{TX}^I$ and $\bar{\omega} \times (\bar{\omega} \times \bar{r}_{TX}^I)$ in eq. (4.8) are also known as Euler's, Coriolis', and centrifugal acceleration, respectively.

It is worth noting that the accelerations \bar{a}_{Π^I} , $\dot{\bar{\omega}}$ are assumed to be constant in the time interval $[t_0, t_0 + T_C]$, while \bar{v}_{Π^I} , $\bar{\omega}$ in eq. (4.7) are *instantaneous* velocities, computed as:

$$\bar{v}_{\Pi^I}(t) = \bar{v}_{\Pi^I}(t_0) + \bar{a}_{\Pi^I} \Delta t$$

$$\bar{\omega}(t) = \bar{\omega}(t_0) + \dot{\bar{\omega}} \Delta t$$

In practice, with the *relative motion transformations* (4.7) and (4.8) we turn the original problem into an equivalent problem, where the wall plane is at rest and the TX/RX velocities and accelerations are modified, according to the point of view of an observer located in the origin of the local frame. It is worth noting that, even in the simple case of TX/RX moving with constant speed, TX and RX are accelerated in the equivalent problem: this acceleration is caused by the angular rotation $\bar{\omega}$ of the wall plane, according to eq. (4.7) and (4.8).

Once the reflection point position, velocity and acceleration have been determined in the local frame using eq. (4.2), (4.3), and (4.4), the following inverse transformations need to be applied:

- back-transformation to get Q_R coordinates, and \bar{v}_{Q_R} and \bar{a}_{Q_R} components w.r.t. the global reference system (inverse *coordinate transformation*).
- back-transformation to get the velocity and acceleration (\bar{v}_{Q_R} and \bar{a}_{Q_R}) relative to an observer located in the origin of the global reference system (inverse

relative motion transformation):

$$\vec{v}_{Q_R}^0 = \vec{v}_{Q_R}^I + \vec{v}_{\Pi^I} + \vec{\omega} \times \vec{r}_{Q_R}^I \quad (4.9)$$

$$\begin{aligned} \vec{a}_{Q_R}^0 = \vec{a}_{Q_R}^I + \vec{a}_{\Pi^I} + \dot{\vec{\omega}} \times \vec{r}_{Q_R}^I + 2\vec{\omega} \times \vec{v}_{Q_R}^I \\ + \vec{\omega} \times (\vec{\omega} \times \vec{r}_{Q_R}^I) \end{aligned} \quad (4.10)$$

4.2.1.2 Multiple reflection generalization

In the case of multiple reflections, the motion of a certain reflection point is influenced by the motion of the previous or latter reflection points. However, the method discussed above can be extended in a straightforward way to a multiple-bounce case.

Let's consider for simplicity a double reflection case: instead of using TX, we can resort to the use of the image-TX (TX') with respect to the first wall plane, and after that we can analyze the reflection on the second wall: in practice, we replace TX with TX' and we bring the computation back to the single-reflection scenario analyzed in the previous section. This means that in a case with two reflecting walls, TX' and RX are used to compute the motion of the reflection point along the second reflecting wall (Q_{R2}), by applying the same procedure as for the single-bounce scenario. Then, once Q_{R2} is known, it is used as a new virtual receiver to compute, in addition to the TX location, the position and the motion of the reflection point along the first reflecting wall (Q_{R1}).

This approach can be iterated in a similar way for the case of more than 2 reflections. In practice, we compute the image-TX (TX'), the image of the image (TX''), etc., until we reach the last reflecting wall, then a "back-tracking" procedure is used: we start from RX and the last reflecting wall, we apply all the equations of the previous section to compute the last reflection point, and then we move back towards TX, to trace the motion of all the remaining reflection points.

In order to apply all the equations of the previous section for the determination of the reflection points motion, we need to apply all the necessary transformations from the global to the local frame, and vice-versa, for each of the reflecting walls.

Moreover, a preliminary computation is needed to compute the position and the instantaneous velocity for each of the image-transmitters. This can be done in a straightforward way by relying on the local frame, and using the image principle. For example, the image-TX with respect to the first wall (TX'), will have the same

x^I and z^I coordinates as TX, and opposite y^I coordinate. Similarly, the velocity components will be:

$$\begin{cases} v_{TX',x}^I = v_{TX,x}^I \\ v_{TX',y}^I = -v_{TX,y}^I \\ v_{TX',z}^I = v_{TX,z}^I \end{cases} \quad (4.11)$$

Once $\bar{v}_{TX'}$ is computed in the local frame, it can be expressed w.r.t. to an observer located in the origin of the global frame, according to the relative motion transformation:

$$\bar{v}_{TX'}^0 = \bar{v}_{TX'}^I + \bar{\omega} \times \bar{r}_{TX'}^I \quad (4.12)$$

In a similar way, the acceleration of the image-TX, $\bar{a}_{TX'}$, can be also found. The DRT algorithm then proceeds according to steps described above, to find the coordinates, velocities and accelerations for each of the reflection points.

The whole DRT algorithm is summarized by the flowchart depicted in Fig. 4.5, with reference to a double-bounce case, for the sake of simplicity.

Once the geometric part is done, i.e. the analytical prolongation of all the rays in the considered time instants within T_C has been completed, the very last step of DRT consists in the re-computation of the field associated to each ray. This is done in a straightforward way as the geometry of the rays is known, by applying the Fresnel's reflection coefficients and the ray divergence factor, as usually done in standard RT algorithms [20, 44]. It is worth noting however, that ray's field computation is based on analytical formulas and is therefore orders of magnitude faster than ray's geometry computation [20].

4.2.2 Diffraction Points' Calculation

The DRT algorithm can be further extended to diffraction, modeled with a ray-based approach according the Uniform Theory of Diffraction (UTD) [45]. A method to track the motion of diffraction points in an analytical way, as previously done for the reflection points, is outlined in this section. We present only the single-diffraction case for the sake of brevity, but the procedure can be extended in a straightforward way to multiple diffractions, as well as to combinations of multiple reflections and

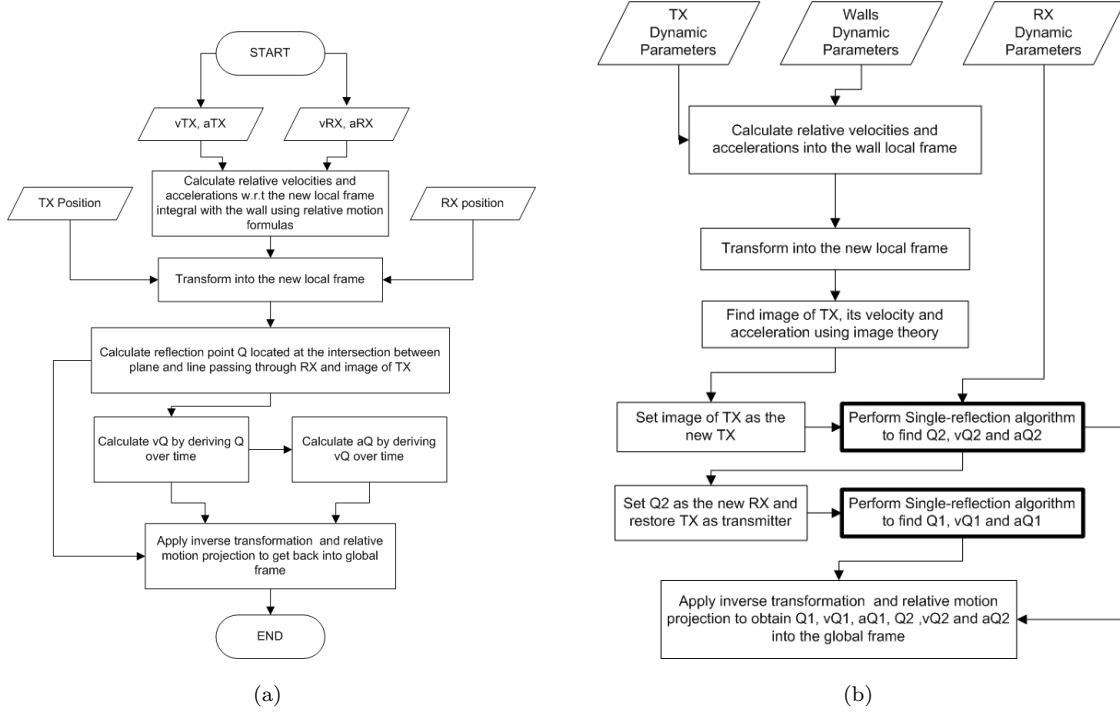


Figure 4.5: Flowcharts showing DRT algorithm : in (a) single reflection algorithm is presented, in (b) double reflection procedure is shown.

diffractions.

In Fig. 4.6 diffraction from an edge formed by two adjacent walls is illustrated, where the unit edge vector \hat{e} is chosen to be aligned with the z -axis of the reference system $Oxyz$, with no loss of generality. For the sake of simplicity and with no limitation - as the diffracted rays lay on the Keller's cone and share the same geometric properties [40] - we represent in Fig. 4.6 an "unfolded" diffracted ray, i.e. the diffraction plane has been rotated to be coincident with the incidence plane.

Since the diffraction point (Q_D) is constrained to move along the edge, the x and y coordinates of Q_D are known, then only z_{Q_D} remains to be computed: this can be done in a simple way by using the similar triangles properties.

Looking at Fig. 4.6, we see that two similar triangles are formed. The sides of these triangles are proportional each other, so the following relation holds:

$$z_{TX} - z_{RX} : d_{TX} + d_{RX} = z_{Q_D} - z_{RX} : d_{RX} \quad (4.13)$$

where

$$\begin{aligned} d_{TX}(t) &= \sqrt{(x_{TX}(t) - x_{Q_D})^2 + (y_{TX}(t) - y_{Q_D})^2} \\ d_{RX}(t) &= \sqrt{(x_{RX}(t) - x_{Q_D})^2 + (y_{RX}(t) - y_{Q_D})^2} \end{aligned} \quad (4.14)$$

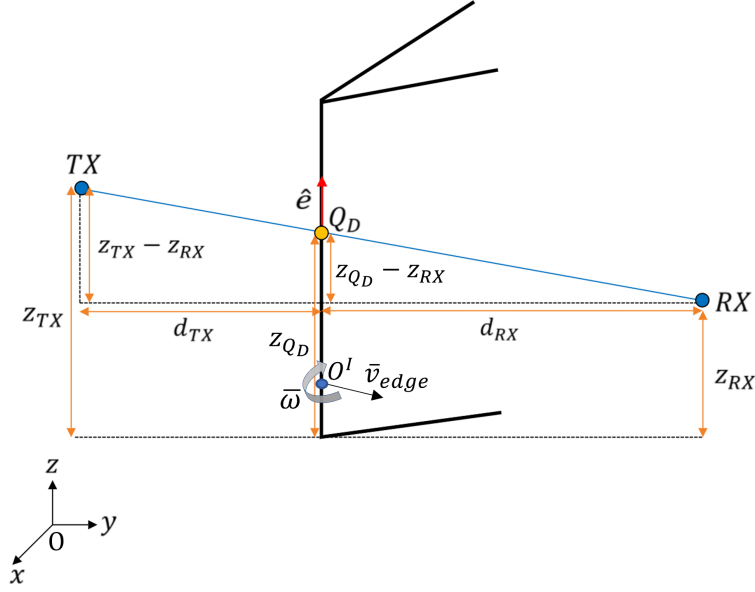


Figure 4.6: Example of edge diffraction, and related geometry for the computation of the diffraction point.

are the 2D distances of TX and RX from the edge, respectively. Hence, the z -coordinate of Q_D is given by:

$$z_{Q_D}(t) = z_{RX}(t) + \frac{d_{RX}(t) \cdot [z_{TX}(t) - z_{RX}(t)]}{d_{TX}(t) + d_{RX}(t)} \quad (4.15)$$

The instantaneous velocity of Q_D ($\bar{v}_{Q_D} = v_{Q_D,z} \hat{z}$) can be computed by time deriving z_{Q_D} . The detailed calculation of $v_{Q_D,z}$ is presented in Appendix C.

Similarly, by further deriving \bar{v}_{Q_D} , we can find the acceleration of the diffraction point, $\bar{a}_{Q_D} = a_{Q_D,z} \hat{z}$, not reported here for the sake of brevity.

The expression in (4.15) and the related velocity and acceleration \bar{v}_{Q_D} , \bar{a}_{Q_D} are valid and do not require any further computation in case the terminals are moving but the edge is at rest. However, in general an edge might be part of a moving object and then might be moving with a certain roto-translational velocity. In particular, we assume that the edge has a rotational motion with instantaneous angular velocity $\bar{\omega}$, and is also translating according to the instantaneous velocity \bar{v}_{edge} . In the example of Fig. 4.6, the edge is rotating clockwise around the x -axis.

As for reflections, we can compute the instantaneous position and the motion of the diffraction point if we assume a proper local reference $O^I x^I y^I z^I$, with the origin located in the rotation center O^I , and the z -axis parallel to the edge. By doing so,

the same procedure used for reflections, can be followed to transform velocities and accelerations, and finally find z_{Q_D} as well as $v_{Q_D,z}$ and $a_{Q_D,z}$.

The final step of DRT is, as usual, the computation of the updated UTD coefficients, and then, of the total diffracted field, at the considered time instant.

4.2.3 Diffuse scattering

Diffuse scattering is modeled according to the Effective Roughness approach [44], which is based on a subdivision of each surface into tiles and on the application of a virtual scattering source to the centroid of each tile. Therefore, the calculation of scattering points' position and speed is straightforward, as it boils down to the application of basic kinematic equations for the motion of rigid bodies' surface points. For instance, equation (4.5) can be used to compute each scattering point's velocity if the rototranslation speed of the body is known.

4.3 Validation on case studies

The presented algorithm is validated over two main case studies. In the first case the results are obtained in a simple vehicular environment. In the second case, a realistic scenario is considered, and results are compared with measurements carried out in an intersection in the city of Lund, Sweden [46].

4.3.1 Case study 1: Street canyon

In this section the results are obtained using the DRT approach in a vehicular environment composed of a street canyon, a moving parallelepiped made of metal representing a bus, and two moving radio terminals. The propagation environment consists of an ideal street canyon 1km long and 30m large, with building walls on both sides and no intersections. Two reflecting walls are also present at its end sections. We first consider a vehicle-to-vehicle (V2V) communication scenario, where the two vehicles carrying TX and RX terminals drive in opposite lanes and the bus is moving on a middle lane between the two terminals as shown in Fig. 4.7a. Therefore, the bus can generate a reflection from its front. We assume that TX is moving toward the end of the street at a constant speed of 50 km/h, RX and

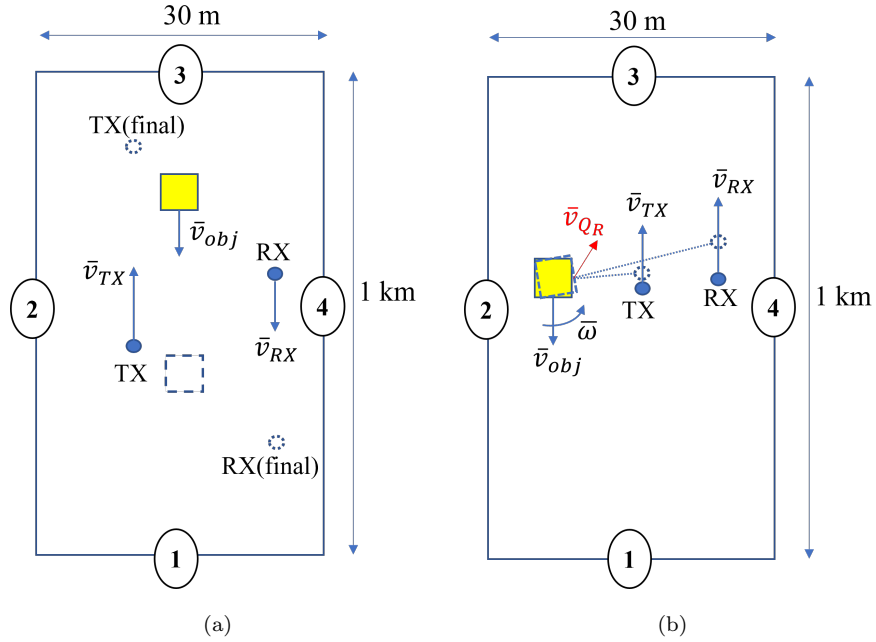


Figure 4.7: Ideal street canyon with a moving parallelepiped representing a bus and two moving terminals TX and RX. In (a) the bus is moving the middle lane, in (b) in the side lane.

the bus are moving in the opposite direction at constant speeds of 36 km/h and 30 km/h, respectively. In the simulations, we considered reflections up to the second order and constant velocities for terminals and moving object.

To perform the simulation of the above-mentioned scenario, omnidirectional antennas were chosen with a transmit power of 1 W operating at a carrier frequency of 3 GHz. The antennas were placed on top of the TX and RX terminals at a height of 1.75m.

4.3.1.1 Power delay profile

Figure 4.8 shows the evolution of Power-Doppler frequency profile (PDFP) obtained through DRT with a total simulation time of 5 seconds and discretized into "bins" for display purposes, with a time step of 200 ms and a Doppler frequency step of 14.34 Hz. The Doppler shift is computed for each ray using eq. (A.2) (see Appendix A). For each bin, an incoherent sum of the power contribution of each ray whose time of arrival and Doppler shift fall within the bin is performed.

Since the scenario is simple and the obstructions or abrupt changes are minimal,

we perform DRT simulation with only two T_C with length 3 s and 2 s. The reason to use two T_C is related to the contributions from the parallelepiped representing a bus: since the bus passes through the LoS line in the middle of the considered time span, the reflection from the front of the bus disappears and therefore we must consider the first T_C expired and refresh the multipath structure with a new RT simulation.

The other main contributions to PDFP (LoS, single and double reflections) are tagged in the plot and are present mainly throughout the whole simulation period. The most interesting trend in the contributions can be seen in the direct ray which from a positive Doppler shift in the first part of the simulation becomes negative with an inflection when TX and RX passes by each other. The same trend can be seen even for the reflections from the side walls but with lower values and less abrupt transitions.

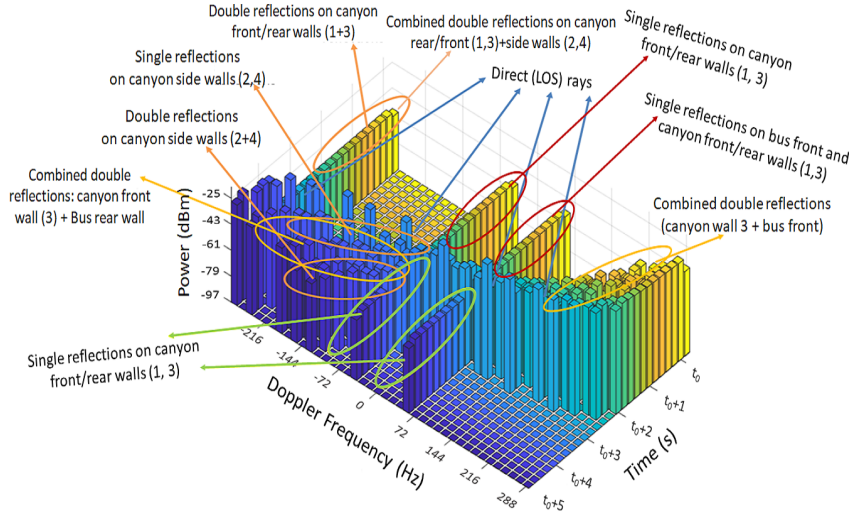


Figure 4.8: PDFP evolution in a V2V scenario with a simulation time of 5 seconds.

4.3.1.2 Absolute value of error

We have also compared the DRT analytical approach with the classical approach based on "snapshots", where the RT simulation is repeated at every discrete time instant. In Fig. 4.9, we show the absolute value of the error of the estimated power by DRT w.r.t RT in each of the time-Doppler bins of fig 4.8. The absolute error is computed as:

$$e_{ij}^{ABS}(dB) = |P_{ij}^{DRT}(dBm) - P_{ij}^{RT}(dBm)|$$

where i, j are the indices associated to the time and Doppler bins, respectively. Fig. 4.9 shows that the error is virtually zero, as even in the worst case its value is several order of magnitudes lower than 1 dB. The non-zero values in Fig. 4.9 are essentially caused by numerical inaccuracies in floating-point operations, and propagation of the errors when applying several successive reference systems transformations. However, it is interesting to observe that the error becomes more evident in cases where there is a strong acceleration of the reflection point, e.g. when the reflecting wall is perpendicular to motion direction of the vehicles. This acceleration becomes more relevant when TX gets nearer to the wall, and also when the wall is part of a moving object.

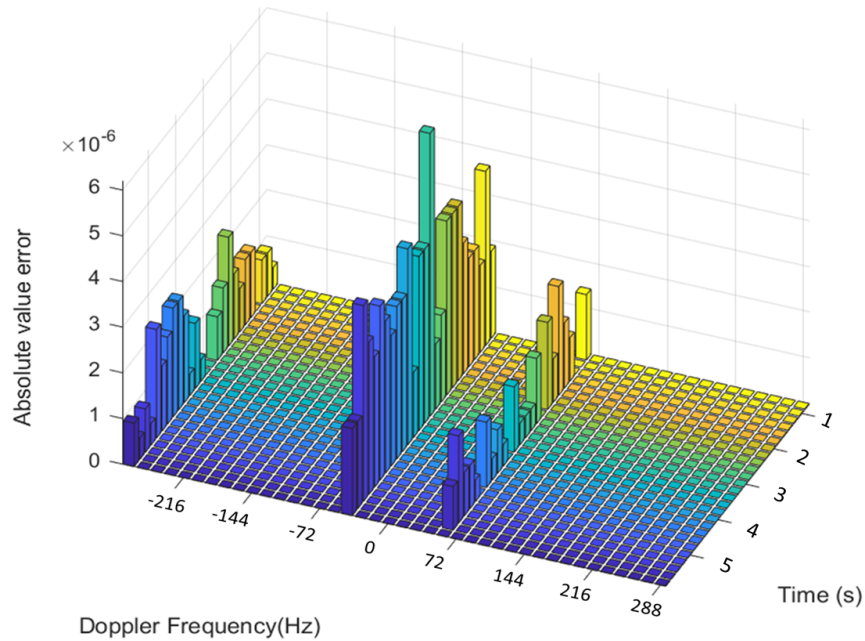


Figure 4.9: Absolute value of error between standard multiple-run RT and DRT analytical approach

4.3.1.3 Bus moving on a side lane and then rotating

We consider now the case of TX and RX moving in the same direction with constant speed at 28 km/h and 30 km/h, respectively, while the bus is moving in the opposite direction at 30 km/h. We consider a time instant when a reflection on the bus side wall is present, and the bus deviates from its straight path toward the center lane, by rotating counterclockwise with an instantaneous angular velocity $\omega = \pi/6$ [rad/s] (see Fig. 4.7b). A comparison of the PDFP is shown in Fig. 4.10 for the case of

the bus driving straight (blue) and the bus swerving toward the center lane (red), respectively. In the first case, the LoS ray and the ray reflected from the bus side are overlapped in the figure with Doppler shift close to zero, as both are almost perpendicular to the TX's, RX's and reflection point's velocities. In the latter case the Doppler's shift of bus reflection becomes positive (37 Hz) due to the reflection point's movement toward the central lane.

This behaviour is important from the applications point of view: when Doppler frequency of a major multipath component abruptly changes, this could indicate a potentially dangerous situation, e.g. a vehicle swerving from its lane.

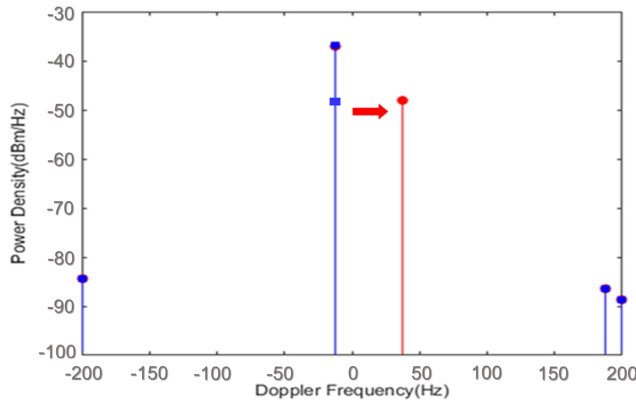


Figure 4.10: PDfP for a snapshot of the V2V scenario with reflection from bus side (see Fig. 4.6(b)). Here TX and RX are moving in the same direction at 28 km/h and 30 km/h, respectively, while bus is moving at 30 km/h in the opposite direction. Bus moving straight without (blue) and with (red) rotation.

4.3.2 Case study 2: Comparison with measurements in an intersection

In this section we perform a validation of DRT simulations results for a V2V scenario by means of a comparison with measured channel data [46] and conventional, multiple-snapshot RT simulation using the same 3D RT algorithm used in our DRT model for initial simulation [20]. Both RT and DRT are performed with a maximum of 2 specular reflections, 1 diffraction and 1 diffuse scattering.

The measurements described in [46] were performed using the RUSK LUND channel sounder at a carrier frequency of 5.9 GHz with a bandwidth of 240 MHz

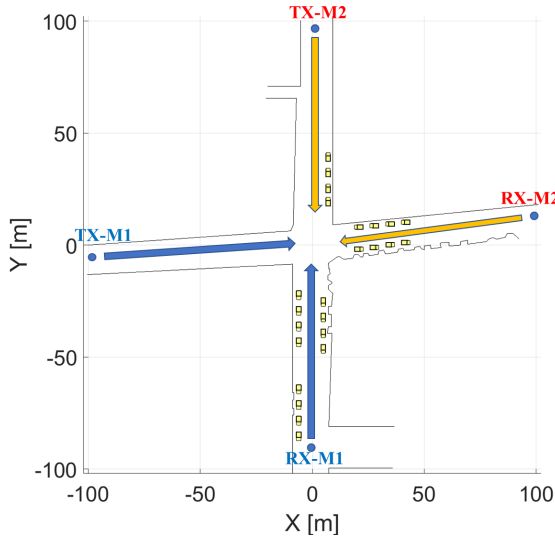


Figure 4.11: Intersection scenario in the city of Lund, Sweden

and TX power of 1 W. The antenna modules, identical for Tx and Rx, consist of 4 identical arrays mounted at 90° from each other and properly driven in order to simulate a quasi omnidirectional antenna. Two hatchback cars were used to carry TX and RX and the antenna modules were mounted on the roof-top. Based on these information, we used omni-directional half-wavelength dipole antennas for all RT and DRT simulations.

4.3.2.1 Power delay profile

The scenario is a narrow urban intersection as shown in Fig. 4.11. The measurements are divided into two parts: *M1*) when TX and RX are driving from the streets *TX – M1* and *RX – M1*, and *M2*) when TX and RX are driving from *TX – M2* and *RX – M2*, respectively, towards the intersection with a speed of approximately 10 m/s. The RT simulations are performed using the classical approach based on snapshots repeated every $\Delta t = 10\text{ms}$. The overall time-span is $t_S = 10\text{s}$. Since the scenario evolution within t_S includes a transition between NLoS and LoS then certainly $t_S > T_C$. Therefore DRT simulation is divided into several T_C , namely into 25 and 20 T_C s for *M1* and *M2*, respectively, with larger T_C s at the beginning of the routes and shorter ones close to the NLoS/LoS transition. Such a subdivision was optimized after a short trial-and-error procedure in order for DRT results to become very similar to RT results. During each T_C the acceleration of the ter-

minals is considered constant. In the first seconds, TX and RX are far from the street intersection and LOS between them is blocked by the buildings situated at the corners for both scenarios. In this period of time, we used only $2T_C$. In the following time span which stretches till the appearance of LOS components (C) and (F) at approximately 6.8s and 7.9s in $M1$ and $M2$, respectively, new contributions appear that make the multipath structure change rapidly. At this stage the number of T_C need to be increased and their duration reduced. The reason to change the duration and the number of T_C in this time span is related with the lower impact of diffraction contributions in higher frequencies such as 5.9 GHz. In these frequencies the transitions between NLOS/LOS become more abrupt. In the last 0.4s leading to the LOS, $4T_C$ with a duration of 100ms, are used in both scenarios. By doing so, we were able to capture most of the contributions in the time span. A further discussion on the criteria for the choice of T_C is provided in the next sub-section.

The measured, RT- and DRT-simulated power delay profiles (PDP) are depicted in Fig. 4.12a, 4.12c, 4.12e for $M1$ and Fig. 4.12b, 4.12d, 4.12f for $M2$. In general, there is good agreement between simulations and measurements with several similar contributions in the RT/DRT simulation and in the measurements. The group of arrows (D), (G) and (B) in Fig. 4.12 point at contributions that probably originated from nearby buildings. There is also good agreement between our simulations and RT simulations performed in [46] although our simulations appears to capture some more contributions in the final 2 seconds of t_S , probably because we considered a larger variety of interactions, including diffuse scattering from building walls and cars parked along the streets. However, there are several contributions in the measured PDP that are missing in the simulations. One of the reasons could be the incomplete building database used in RT/DRT. For example some of the contributions like (E) and (I), in [46] are said to be from a building which has a metallic structure on the walls, which is not present in the building database. This shows the necessity of a very detailed scenario description in order to get a really good match between simulations and measurements.

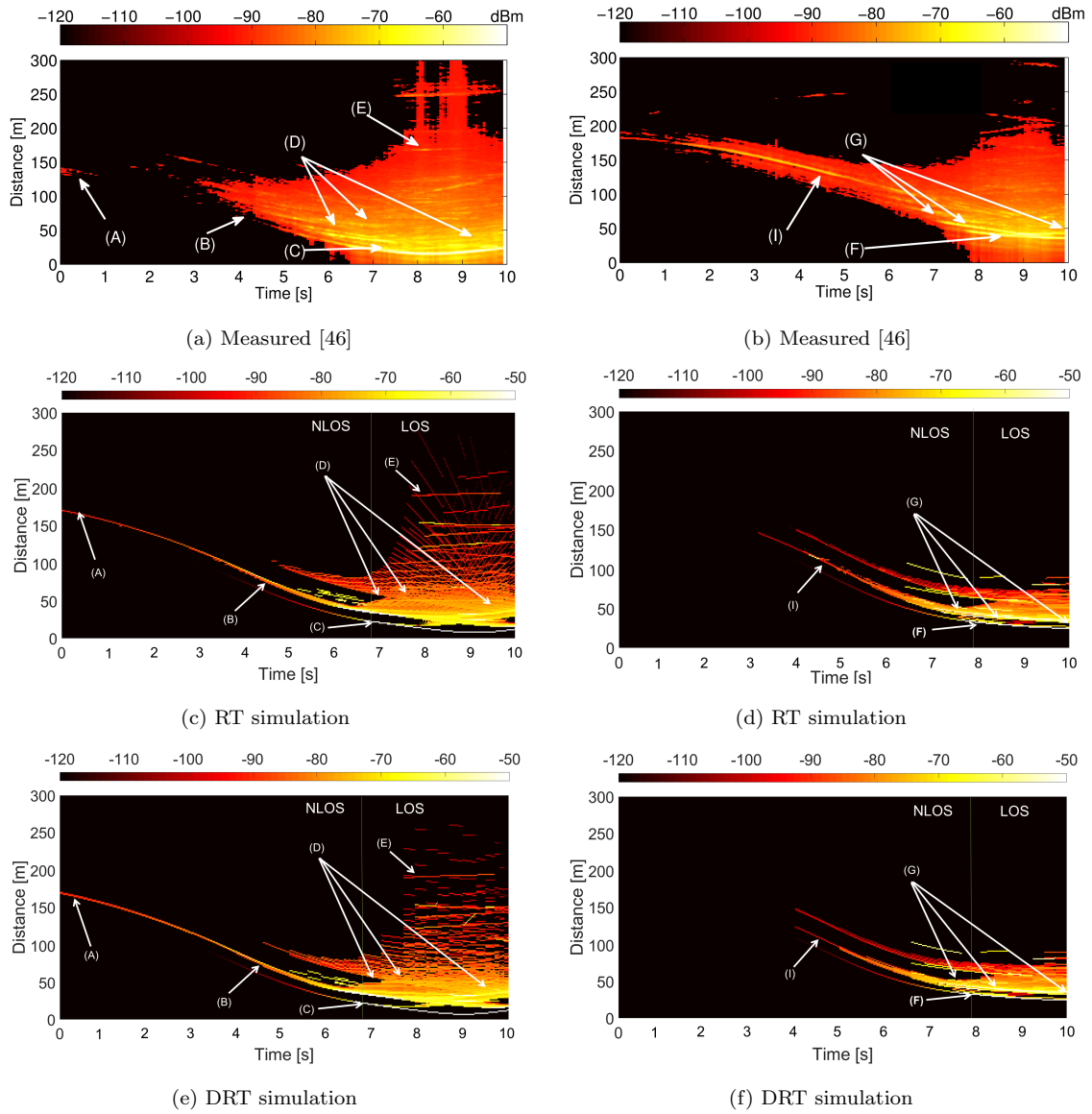


Figure 4.12: Power Delay Profile obtained from measurements (a) and (b), from RT simulations (c) and (d) and from DRT prediction (e) and (f)

4.3.2.2 Impact of the choice of T_C

The number of T_C and the right choice of them is very important in DRT simulation, that has a strong impact on both accuracy of results and computation time. In Fig. 4.13a, DRT simulation PDP for $M1$ is presented with only $3T_C$. It is evident that results are incomplete if compared to Fig. 4.12e because dynamic changes in the multipath structure are under-sampled in this case and several paths are missed. In Fig. 4.13b, $10T_C$ has been used. The PDP in this case is more complete and many new contributions can be seen. Nevertheless a larger number of T_C close to the NLoS/LoS transition is needed in order to achieve the more complete results of Fig. 4.12e.

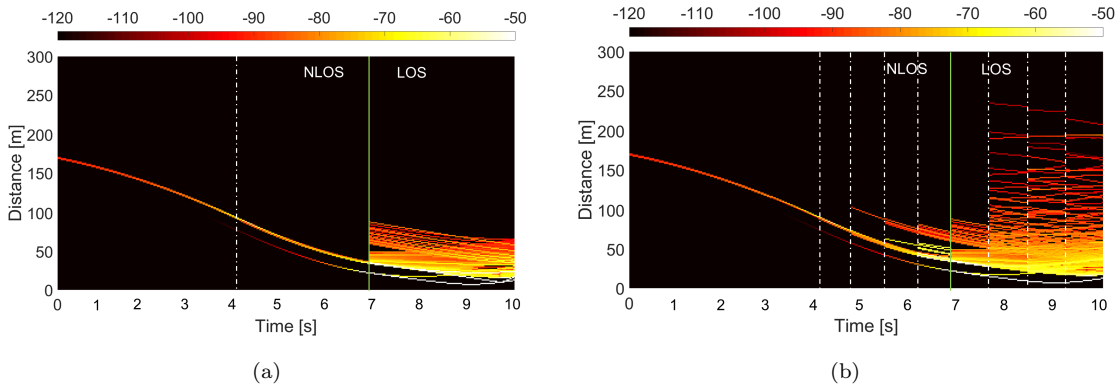


Figure 4.13: PDP obtained from simulation with DRT. In (a) $3T_C$ were used, in (b) $10T_C$

4.3.3 Computational gain

To compare the computation time of DRT vs. RT, we recorded computation times with the two approaches in $M1$ and $M2$ on the same Intel(R) Core(TM) i5-8265U CPU @1.60GHz 1.80 GHz platform. In DRT, one traditional RT run is included for multipath initialisation at the beginning of each T_C . To achieve the desired graphical resolution 1000 runs are performed with both DRT and RT, but a large fraction of them only requires the computation of analytical extrapolation formulas when using DRT, with a great computation time gain.

From Table 4.1, we can observe a CPU-time gain of about 48 times for the $M2$ scenario while the computational gain is even higher in the $M2$ scenario because the

number of T_C is smaller.

Table 4.1: Execution time for RT and DRT in M1 and M2

	RT with snapshots	DRT Analytical	Speed-up Factor
M1	4486 seconds	97.9 seconds	45.8x
M2	4384 seconds	88.8 seconds	48.2x

4.3.4 Future prospect: Predictive Radio Awareness

The DRT approach to predict “ahead-of-time” (or anticipate) the environment and/or the radio channel characteristics in highly dynamic, industrial or vehicular applications and realize the so-called *predictive radio awareness* or *location aware communications* [47, 48] is quite attractive. Exploiting such capabilities could be of paramount importance to guarantee reliable connectivity in critical application such as automated and connected driving and to foster interesting safety applications to detect dangerous situations in advance. Two kinds of applications are possible:

1. DRT-based radio channel anticipative prediction
2. Environment configuration anticipative prediction

In both cases, accurate localization of radio terminals and moving objects, which is likely to be available in future mobile radio systems [49, 50], is a prerequisite. Accurate localization, together with the availability of a local environment database is used to build a dynamic environment database for the current time T_0 . In 1), DRT is used to extrapolate multipath characteristics, and therefore to estimate the Channel State Information for $t > T_0$. In 2) kinematics theory is used to extrapolate the environment configuration for $t > T_0$ and therefore detect possible hazards or collisions. These applications will be fully addressed in follow-on studies. It is worth noting that, in turn, the availability of techniques 1) and 2) would be of great help to realize multipath-exploiting localization techniques [51]. Therefore, the two goals of anticipative channel prediction and localization might be achieved in synergy to realize an environment-aware system and enhance both connectivity and safety, as depicted in Fig. 4.14.

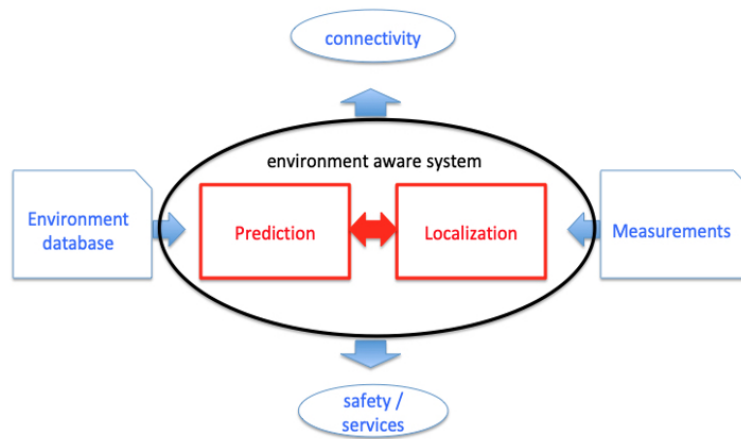


Figure 4.14: Scheme of an environment-aware system including both channel prediction and localization

Part II

An Energy-Efficient Unselfish Spectrum Leasing Scheme for Cognitive Radio Networks

Chapter 5

Background and motivation

The exponential growth of wireless services in the last decades has called for additional spectrum to accommodate the ever-increasing traffic flow. Besides, the current static spectrum policy, used by most countries in the world, has almost resulted in licensed spectrum exhaustion of some frequency bands [52]. On the contrary, recent spectrum utilization measurements have shown that the available spectrum opportunities are severely underutilized. Cognitive radio (CR), with its ability to sense available frequency bands and adaptively adjust transmission frequency, has attracted considerable attention as one of the most promising solutions to spectrum under-utilization [53–55]. Traditionally in CR networks (CRNs), there are two categories of users, namely, primary users (PUs) and secondary (SUs). PUs are licensed users, and they have the exclusive right to use their respective channels, while SUs are unlicensed, and they wish to use the underutilized channels [56]. To pay off the use of a licensed band, cooperative CRNs (CCRN) have been proposed in which SUs act as relays to provide a better transmission performance to the PUs.

5.1 Introduction to CRNs

The concept of CR was first proposed by Joseph Mitola III in 1998 and published in an article. It was a novel approach in wireless communications, which Mitola later describes as:

The point in which wireless personal digital assistants (PDAs) and the related networks are sufficiently computationally intelligent about radio resources and related

computer-to-computer communications to detect user communications needs as a function of use context, and to provide radio resources and wireless services most appropriate to those needs. [53]

In other words a CR is an intelligent radio that can be programmed and configured dynamically. Such a radio automatically detects available channels in wireless spectrum, then accordingly changes its transmission or reception parameters. [57] [58]

Two of the most important abilities of CR are:

- **Cognitive capability** Cognitive capability refers to the ability of the radio technology to capture or sense the information from its radio environment. this capability cannot simply be realized by monitoring the power in some frequency band of interest but more sophisticated techniques are required in order to capture the temporal and spatial variations in the radio environment and avoid interference to other users. Through this capability, the portions of the spectrum that are unused at a specific time or location can be identified. Consequently, the best spectrum and appropriate operating parameters can be selected [59].
- **Re-configurability** The cognitive capability provides spectrum awareness whereas re-configurability enables the radio to be dynamically programmed according to the radio environment. More specifically, the cognitive radio can be programmed to transmit and receive on a variety of frequencies and to use different transmission access technologies supported by its hardware design.

CRNs are traditionally divided into two groups: primary users (PUs) and secondary users (SUs). PUs has a license to operate in a certain spectrum band. This access can only be controlled by a primary base station (PBS) and should not be affected by the operations of any other unlicensed user. PUs do not need any modification or additional functions for coexistence with SUs. Meanwhile, SUs do not have any license to operate in a desired band. Hence,additional functionalities are required to share the licensed spectrum band. In addition, PUs as well as SUs can either communicate with each other in a multihop manner or access base stations.

5.1.1 Key technologies in CRN

The key enabling technology of CRNs is the cognitive radio. CR techniques provide the capability to use or share the spectrum in an opportunistic manner. Dynamic spectrum access techniques allow the cognitive radio to operate in the best available channel.

Once a CR supports the capability to select the best available channel, the next challenge is to make the network protocols adaptive to the available spectrum. Hence, new functionalities are required in a secondary network to support this adaptivity. In summary, the main technologies for CRs in CRN can be summarized as follows:

1. **Spectrum sensing** Detecting unused spectrum and sharing the spectrum without harmful interference with other users. Spectrum-sensing techniques may be grouped into three categories:
 - a) **Transmitter detection** Cognitive radios must have the capability to determine if a signal from a primary transmitter is locally present in a certain spectrum.
 - b) **Cooperative detection** Refers to spectrum-sensing methods where information from multiple cognitive-radio users is incorporated for primary-user detection
 - c) **Interference based detection** Interference is typically regulated in a transmitter centered way, which means interference can be controlled at the transmitter through the radiated power, the out-of-band emissions and location of individual transmitters.
2. **Spectrum management** Capturing the best available spectrum to meet user communication requirements, while not creating undue interference to other (primary) users. CRs should decide on the best spectrum band (of all bands available) to meet quality of service requirements; therefore, spectrum-management functions are required for CRs.
3. **Spectrum mobility** Process by which a cognitive-radio user changes its frequency of operation. CRNs aim to use the spectrum in a dynamic manner

by allowing radio terminals to operate in the best available frequency band, maintaining seamless communication requirements during transitions to better spectrum.

4. **Spectrum sharing** Spectrum sharing in CRNs allows CRs to share the spectrum bands of the licensed-band users. However, the cognitive radio users have to restrict their transmit power so that the interference caused to the licensed-band users is kept below a certain threshold.

5.2 Cooperative communications in CRN

Cooperative communications (CC) and CR have attracted a widespread attention in the past years. CC technique can enhance the transmission capacity of a communication system, while CR can improve the spectrum utilization ratio. As a result, the combination of these two approaches can have a significant impact in future wireless mobile communications.

In multi-user communication environment, cooperative communication technique enables the neighboring mobile users with single antenna to share their antennas in some way for cooperative transmission, which is similar to a distributed virtual multi-antenna transmission environment and combines the advantages of both diversity technology and relay transmission technology. As a result, the spatial diversity gains can be achieved and the system's transmission performance can be improved in a cooperative communication system without adding any antennas. It can be applicable to such networks as cellular mobile communication systems, wireless Ad hoc networks, Wireless Local Area Networks (WLANs) and wireless sensor networks. Being highly flexible, cooperative communication can be integrated with other technologies without sacrificing their respective advantages. Integrated with CR technology, it can improve the spectrum detection probability or get more spectrum access chances [60].

There are three ways to apply CC concept in CRN: 1) cooperation between PU peers, 2) cooperation between SU peers, and 3) cooperation between PUs and SUs. The first type may result easy if PUs belong to the same mobile operator, while might be trivial if they have different operators because logistic and economi-

cal problems may arise. The second category can be applied for inactive PUs, where neighboring SUs can lease spectral bands together from PUs, and perform CC between them. Meanwhile, the third one, since PU and SU have different priorities and they might have security concerns for their own data, cooperation between them can be challenging. This category represents an important topic for CCRN which supports a cooperation between PUs and SUs. PUs actively select SUs with good channel conditions as their cooperative relays and lease a part of the spectrum to them. Therefore, a "win-win" situation is created where PUs can potentially increase their transmission rates and save transmit power, while SUs can access the available frequency bands otherwise unavailable to them. nevertheless, In a scenario with multiple PUs and multiple SUs, the issue of relay selection and coordination needs to be considered.

5.3 Spectrum leasing in CCRN

Extensive research has been conducted regarding spectrum leasing in CCRN. To address the challenges several approaches have been adopted. The game-theoretical approaches, such as Stackelberg game [61], are used to achieve the equilibrium state (e.g., Nash Equilibrium [62]) and involves PUs and SUs as players of the game. In [63], a scenario, in which PUs compete for cooperation with available SUs under shared constraint set by SU's requirements, is modeled as a generalized Nash Equilibrium. The authors in [64], propose a noncooperative game to find the optimal power of SUs consumed in a scenario where SUs are used as relays in cooperation to aid PUs' transmission. In [65], a spectrum leasing technique to improve the spectral utility of the PUs has been proposed. Nash bargaining is used to determine the optimal division of temporal resources between relaying and reimbursement. In [66], a novel approach is presented in which the spectrum leasing problem is formulated as a Stackelberg game, while the relay selection is solved by the Hungarian method. Authors in [67], derive a cooperative game to find the optimal spectrum leasing time and allocated power of SUs.

Another popular approach is convex optimization. An adaptive spectrum leasing scheme is proposed in [68] to improve the overall network throughput. Authors

in [69], present a spectrum leasing scheme for an overlay CRN in which PUs' transmission is assisted by a cognitive multi-hop multi-branch network. The branch selection and spectrum allocation are jointly optimized such that the sum-rate of the SUs is maximized. A multi-objective optimization framework to incorporate average sum power minimization and the leased time minimization is proposed in [70]. In [71], a cooperative sharing model for cognitive wireless powered networks is proposed, to accomplish PU's transmission early and vacate opportunity for SU's transmission. An energy efficiency and spectral efficiency trade-off in an energy harvesting cooperative CRN is addressed in [72]. The objective is to maximize energy and spectral efficiency via joint optimization of spectrum sensing time and self as well as cooperative transmission gains.

Different other approaches have been chosen to address the challenges of spectrum leasing in CCRN. In [73], an opportunistic relaying based spectrum leasing is presented in which PUs lease their frequency band to the SUs and, at the same time, the primary network benefits in terms of outage probability. A cooperative relaying scheme is investigated in [74], where one of the inactive SUs is used as a relay for the PUs. By adopting an aspiration level to model SUs behavior, the SUs' strategy dynamics is formulated as a discrete-time Markov chain [75].

5.4 Motivation and contribution

The majority of the research works regarding CRNs, are considered mostly PU-centered, with PUs that decide if and when to exploit SUs as relays based on certain conditions that can improve PUs' transmission. This approach cannot guarantee full cooperation between PUs and SUs because will be dominated by the selfish behavior of PUs. In addition, networks are required nowadays to be more efficient not only in terms of spectrum use but also in terms of optimal power while guaranteeing a satisfying level of quality of service (QoS). Hence scenarios where a single pair of PUs or SUs are considered like the ones proposed in [63], [73], and [74], can result incomplete because they cannot give a full description of the efficiency of a cell. It is proven that the rising number of users in a CCRN can significantly affect the overall performance of the network. Furthermore, spectrum leasing schemes in which PUs

or SUs are assumed to have fixed transmission power like in [66], cannot fully exploit the possibility of a more energy efficient network. Besides, energy-efficient systems are required not only from an engineering point of view but also to decrease the environmental impact through networks with a low carbon footprint.

Motivated by the aforementioned observations, we aim at jointly minimize the overall power consumption for energy-efficient communication in multiuser CRN. In addition, to provide improved cooperation between PUs and SUs and to secure an unselfish behavior of each user, we propose a resource management network architecture for a considered cell. This architecture, composed of various entities, will be responsible for making decisions regarding the usage of relay and for applying the optimal strategy to achieve the maximum energy efficiency of the cell. Our proposed CRN consists of multiple PUs and multiple SUs in which SUs are used as relays to enhance the PUs' transmission performance and, in return, PUs lease a fraction of their bandwidth to the corresponding SUs. We formulate an energy efficiency based resource allocation, power allocation, and relay selection as an optimization problem. Our analysis shows that this problem can be divided into two subproblems: 1) power allocation, 2) transmission mode and relay selection. To solve the power allocation subproblem, we choose the maximization of the sum of energy efficiencies as the optimization target. This method was initially introduced in [76] but due to its sum-of-ratio form can become difficult to solve. The method is further developed in our work by transforming power allocation into a subtractive form optimization problem with methods similar to those used to solve classical fractional programming problems [77–79]. Therefore, the optimal powers closed-form expressions can be derived through a two-layer optimization. Furthermore, the transmission mode and relay selection subproblem is solved based on a modified Kuhn-Munkres bipartite matching algorithm. System simulations performed in a referenced multiuser case validate the effectiveness of our approach proven by the proposed algorithm's convergence and the increment in the efficiency of the PUs' network performance when channel conditions get worse.

To summarize, the main contributions of the paper are:

- A novel unselfish resource allocation scheme for CRNs. Unlike most of works where PUs decide whether or not to cooperate with SUs, the decisions are

made by a centralized approach with the goal of improving the overall energy efficiency of the cell.

- A resource management network architecture responsible for maximizing energy efficiency of the cell.
- We propose a two-stage three-dimensional matching algorithm to maximize the energy efficiency of the cell, in which the joint optimization problem is decoupled into two subproblems and solved separately in two stages.

Chapter 6

Proposed architecture and system model for CCRN

6.1 Proposed Architecture

In CCRN, one of the goals is to use the available spectrum resources in an efficient and coordinated way to guarantee a satisfying level of QoS for all users and achieve performance enhancement of the whole cell. To this end, in this section, we propose a resource management network architecture consisting of a number of user resource management entities (URMEs), local resource management entities (LRMEs), and one cell resource management entity (CRME), as shown in Fig. 6.1. The main functions of URMEs, LRMEs, and CRME are described as follows.

URME: It is a functional module embedded in each PU and SU, used to store channel state information, device characteristics and service requirements, etc. Through contacting associated LRMEs, URMEs send the collected information to the network and receive the resource allocation strategy accordingly.

LRME: It is deployed in each PBS or SBS, being responsible for managing local resource status through interacting with the associated URMEs and the CRME. More specifically, receiving the network and service information from URMEs and then forwarding to the CRME, and receiving the resource management strategy from the CRME and forwarding to the URMEs.

CRME: By interacting with the LRME, the CRME receives the network status, channel state information, and user service requirement information of all the users

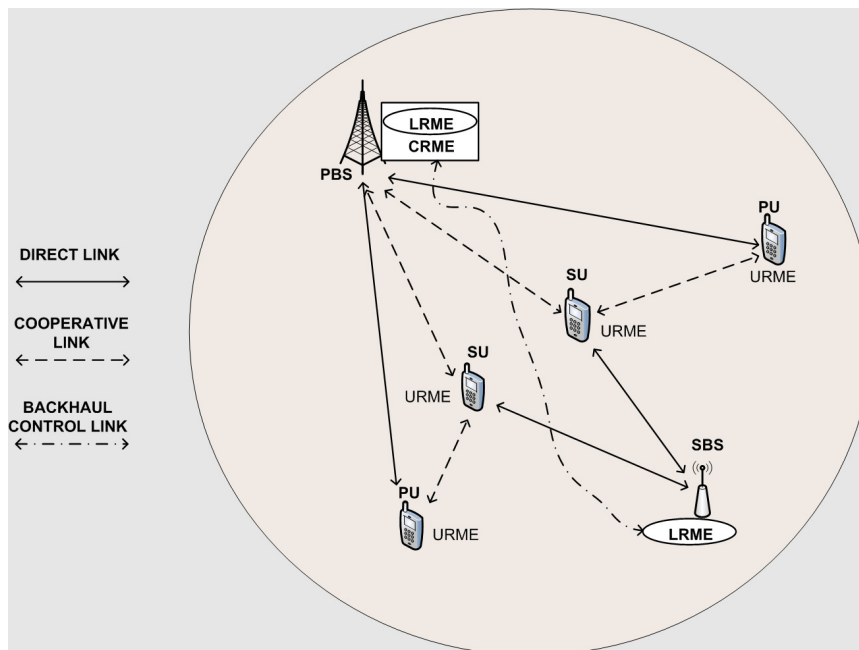


Figure 6.1: Proposed architecture and scenario for the cell.

within the cell; then performs the proposed resource allocation and relay selection algorithm to obtain the optimal strategy for the cell and communicated to the associated LRMEs.

6.2 System Model

In this paper, we consider a CCRN consisting of multiple PUs, multiple SUs, one primary base station (PBS), and one secondary BS (SBS). Assume PUs are allowed to transmit to the PBS simultaneously, by orthogonal frequency division multiple access (OFDMA). Further, assume that PUs may transmit to the PBS in direct transmission mode or one-hop relay transmission mode, while the relay SUs may also transmit their own data packets to the SBS. Fig. 6.1 illustrates the scenario considered in this paper.

To encourage SUs to relay data packets for the PUs, we propose a spectrum leasing scheme where the PUs lease part of their allocated spectrum to relay SUs so that they can transmit their own data to the SBS exploiting the licensed spectrum [80]. In this paper, we assume that the decode-and-forward (DF) scheme is applied at each relay node [81].

Let M and K denote the number of PUs and the number of SUs, respectively,

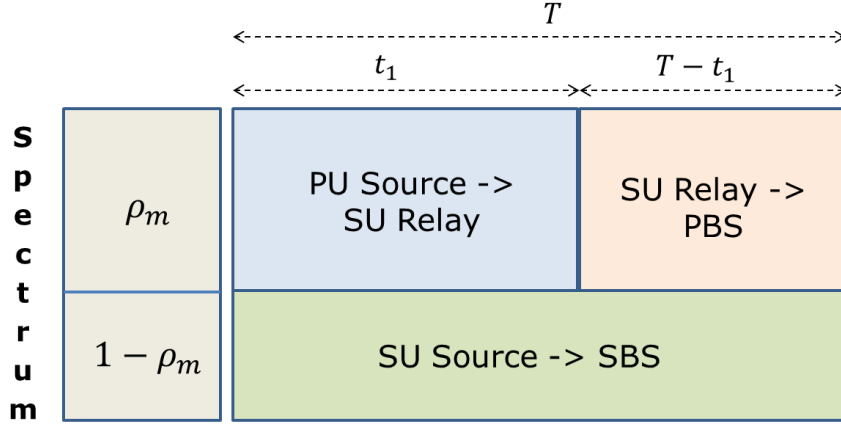


Figure 6.2: Bandwidth allocation and time slot division for PU and SU.

$B_m = \rho_m B$ denote the allocated bandwidth of the m th PU, $m = 1, \dots, M$, where $\rho_m \in [0, 1]$ denotes the spectrum fraction of the m th PU for transmitting the data packets of the PU in the relay transmission mode, and as a consequence $B_k = (1 - \rho_m)B, \forall k$, is the remaining spectrum available for the relay SU to transmit its own data to the SBS. To support relay communication, the transmission time slot T is divided into two periods. For the first part, the PUs transmit their data packets to the corresponding relay SUs, then the SUs forward the received data packets to the PBS during the remaining time. Meanwhile, the SUs transmit their own data packets to the SBS for the whole time period. Fig. 6.2 shows the time and spectrum division mode for relay transmission of the m th PU.

It is assumed that all channels undergo flat Rayleigh fading and log-normal shadowing and we consider that LRMEs know all the channel state information. The distance between m th PU and k th SU relay is denoted as $d_{m,k}^{(p,s)}$. Then the channel power gain is represented as $h_{m,k}^{(p,s)} = k_0 (d_{m,k}^{(p,s)})^{-\gamma} g_{m,k}^{(p,s)} s_{m,k}^{(p,s)}$, where k_0 denotes the average channel gain at a reference distance $d_0 = 1\text{m}$ and this gain depends on carrier frequency, transmitter and receiver antenna gains and propagation characteristics, $\gamma > 0$ is the path-loss exponent, $g_{m,k}^{(p,s)}$ is the Rayleigh distributed r.v., and $s_{m,k}^{(p,s)}$ is the log-normal r.v. with shadowing parameter σ_s . The same channel model is considered for the other links $h_m^{(p,d)}, h_{m,k}^{(p,r)}, h_{m,k}^{(s)}$ representing respectively the channel gains of the links between the m th PU and PBS in direct transmission mode, the k th SU and PBS in relay mode, and the k th SU when transmitting its own data to the SBS on the fraction of bandwidth leased by the m th PU.

In case of multiple relay SUs being available, the optimal relay selection scheme should be designed. For each PU-SU pair, the transmit power of PU, $P_{m,k}^{(p,s)}$ and the transmit power of the relay SU, consumed during relay $P_{m,k}^{(p,r)}$, and during its own data transmission $P_{m,k}^{(s)}$, should be designed for performance optimization of the cell.

Chapter 7

Proposed joint resource allocation and relay selection scheme

In the following sections, we formulate an optimization problem, and we present a new solution to the energy efficiency based resource allocation, power allocation, and relay selection.

7.1 Energy Efficiency of PUs

The energy efficiency of all the PUs can be expressed as

$$\eta^{(p)} = \sum_{m=1}^M \eta_m^{(p)} \quad (7.1)$$

where $\eta_m^{(p)}$ denotes the energy efficiency of the m th PU. As PUs may choose direct transmission or cooperative transmission through a relay SU for information transmission to the PBS, the energy efficiency of the m th PU can be calculated as

$$\eta_m^{(p)} = \beta_m^{(d)} \eta_m^{(p,d)} + \sum_{k=1}^K \beta_{m,k}^{(c)} \eta_{m,k}^{(p,c)} \quad (7.2)$$

where $\eta_m^{(p,d)}$ is the energy efficiency of the m th PU when using direct mode, while $\beta_m^{(d)} \in \{0, 1\}$ denotes the transmission indicator of the m th PU for the direct mode. More specifically, if $\beta_m^{(d)} = 1$, the m th PU uses direct transmission mode, while for

$\beta_m^{(d)} = 0$, the PU exploits SU relay assisted transmission. The term $\eta_{m,k}^{(p,c)}$ denotes the energy efficiency of the m th PU when using the k th SU as relay node for cooperative transmission mode, while $\beta_{m,k}^{(c)} \in \{0, 1\}$ is the corresponding transmission and relay selection variable, i.e., $\beta_{m,k}^{(c)} = 1$ indicates that the m th PU uses the k th SU as relay node for cooperative transmission, and $\beta_{m,k}^{(c)} = 0$, otherwise. Note that $\beta_m^{(d)}$ and $\beta_{m,k}^{(c)}$ are mutually exclusive. In the following subsections, we derive the expression of $\eta_m^{(p,d)}$ and $\eta_{m,k}^{(p,c)}$, respectively.

7.1.1 Direct Mode

The energy efficiency of the m th PU in direct mode, i.e., $\eta_m^{(p,d)}$ can be calculated as

$$\eta_m^{(p,d)} = \frac{R_m^{(p,d)}}{P_m^{(p,d)} + P_c^{(p)}} \quad (7.3)$$

where $P_m^{(p,d)}$ is the power consumed by the m th PU when transmitting in direct mode, $P_c^{(p)}$ denotes the circuit power consumption of the m th PU, which is assumed to be a constant for all the PUs in this work, and $R_m^{(p,d)}$ denotes the data rate achieved by the m th PU in direct mode, which can be expressed as

$$R_m^{(p,d)} = B \log_2 \left(1 + \frac{P_m^{(p,d)} h_m^{(p,d)}}{\sigma^2} \right) \quad (7.4)$$

where σ^2 is the noise power of the link between the m th PU and the PBS. Without loss of generality, the noise power of all the transmission links are assumed to be the same in this work.

7.1.2 Relay Mode

The energy efficiency of the m th PU when using the k th SU as relay node for cooperative transmission, denoted by $\eta_{m,k}^{(p,c)}$, can be expressed as

$$\eta_{m,k}^{(p,c)} = \frac{R_{m,k}^{(p,c)}}{P_{m,k}^{(p,c)}}. \quad (7.5)$$

The denominator $P_{m,k}^{(p,c)}$ is the power consumption of the m th PU when using the k th SU as a relay node and can be calculated as

$$P_{m,k}^{(p,c)} = P_{m,k}^{(p,s)} + P_{m,k}^{(p,r)} + P_c^{(p)} + P_c^{(s)} \quad (7.6)$$

where $P_c^{(s)}$ denotes the circuit power consumption of the SU which is assumed to be a constant for all the SUs. The numerator $R_{m,k}^{(p,c)}$ represents the data rate of the m th PU when using the k th SU as relay node for cooperative transmission. $R_{m,k}^{(p,c)}$ can be expressed as

$$R_{m,k}^{(p,c)} = \min(R_{m,k}^{(p,s)}, R_{m,k}^{(p,r)}) \quad (7.7)$$

where $R_{m,k}^{(p,s)}$ and $R_{m,k}^{(p,r)}$ are, respectively, the data rate of the link from the m th PU to the k th SU

$$R_{m,k}^{(p,s)} = t_1 \rho_m B \log_2 \left(1 + \frac{P_{m,k}^{(p,s)} h_{m,k}^{(p,s)}}{\sigma^2} \right) \quad (7.8)$$

and that from the k th SU to the PBS when the k th SU is chosen as the relay node of the m th PU

$$R_{m,k}^{(p,r)} = (1 - t_1) \rho_m B \log_2 \left(1 + \frac{P_{m,k}^{(p,r)} h_{m,k}^{(p,r)}}{\sigma^2} \right), \quad (7.9)$$

with t_1 denoting the transmission time needed from the PU to transmit the data packets towards the relaying SU, and $1 - t_1$ denoting the transmission time for the transmission from the corresponding relaying SU to the PBS.

7.2 Energy Efficiency of SUs

The energy efficiency of all the SUs in the CCRN, denoted by $\eta^{(s)}$, can be calculated as

$$\eta^{(s)} = \sum_{m=1}^M \sum_{k=1}^K \beta_{m,k}^{(c)} \eta_{m,k}^{(s)} \quad (7.10)$$

where $\eta_{m,k}^{(s)}$ is the energy efficiency of the k th SU when transmitting its own data on the subchannel leased by the m th PU, which can be calculated as

$$\eta_{m,k}^{(s)} = \frac{R_{m,k}^{(s)}}{P_{m,k}^{(s)} + P_c^{(s)}} \quad (7.11)$$

where $R_{m,k}^{(s)}$ denote the data rate of the k th SU when transmitting its own data on the subchannel leased by the m th PU

$$R_{m,k}^{(s)} = (1 - \rho_m) B \log_2 \left(1 + \frac{P_{m,k}^{(s)} h_{m,k}^{(s)}}{\sigma^2} \right). \quad (7.12)$$

7.3 Energy Efficiency for CCRN Problem Formulation and Solution

The total energy efficiency of the PUs and the SUs can be formulated as:

$$\eta = \eta^{(p)} + \eta^{(s)}. \quad (7.13)$$

In the following, we propose a joint resource allocation, power allocation, and relay selection strategy to maximize the total energy efficiency (7.13).

7.3.1 Optimization Problem Formulation

The energy efficiency based power allocation, transmission mode and relay selection scheme can be obtained by solving the following optimization problem:

$$\begin{aligned} & \max_{[\beta_m^{(d)}, \beta_{m,k}^{(c)}, P_m^{(p,d)}, P_{m,k}^{(p,s)}, P_{m,k}^{(p,r)}, P_{m,k}^{(s)}]} \eta & (7.14) \\ \text{s. t. } & \text{C1: } \beta_m^{(d)} + \sum_{k=1}^K \beta_{m,k}^{(c)} \leq 1, \quad m = 1, 2, \dots, M \\ & \text{C2: } \sum_{m=1}^M \beta_{m,k}^{(c)} \leq 1, \\ & \text{C3: } P_m^{(p,d)} \leq P_m^{(p,\max)}, \text{ if } \beta_m^{(d)} = 1, \\ & \text{C4: } P_{m,k}^{(p,s)} \leq P_m^{(p,\max)}, \text{ if } \beta_{m,k}^{(c)} = 1, \\ & \text{C5: } P_{m,k}^{(p,r)} + P_{m,k}^{(s)} \leq P_k^{(s,\max)}, \text{ if } \beta_{m,k}^{(c)} = 1, \\ & \text{C6: } R_m^{(p,d)} \geq R_m^{(p,\min)}, \text{ if } \beta_m^{(d)} = 1, \\ & \text{C7: } R_{m,k}^{(p,s)} \geq R_m^{(p,\min)}, \text{ if } \beta_{m,k}^{(c)} = 1, \\ & \text{C8: } R_{m,k}^{(p,r)} \geq R_m^{(p,\min)}, \text{ if } \beta_{m,k}^{(c)} = 1, \\ & \text{C9: } R_{m,k}^{(s)} \geq R_{m,k}^{(s,\min)}, \text{ if } \beta_{m,k}^{(c)} = 1. \end{aligned}$$

C1 represents the transmission mode indicator constraint since it is assumed that every PU can only choose direct transmission mode or relay transmission mode. Similarly, C2 specifies the relay mode indicator constraint as it is assumed that every PU can choose only one SU as its relay node and each SU can only forward packets for one PU. C3, C4 and C5 denote the maximum power constraint where $P_m^{(p,\max)}$

and $P_k^{(s,\max)}$ denote respectively the maximum transmit power of the m th PU and the k th SU. C6-C9 represent the minimum data rate constraints where $R_m^{(p,\min)}$ and $R_k^{(s,\min)}$ denote respectively the minimum required data rate of the m th PU and the k th SU.

The optimization problem in (7.14) can be classified as a nonlinear binary fractional program and therefore difficult to solve using traditional optimization methods [78]. From the optimization constraints C3-C9 given in (7.14), it can be shown that such an optimization problem can be transformed equivalently into two subproblems: 1) power allocation, 2) transmission mode and relay selection. The solution for each subproblem is presented in the following subsections.

7.3.2 Power Allocation Subproblem

Assuming that the m th PU selects direct transmission mode, i.e., $\beta_m^{(d)} = 1$, the energy efficient optimal power allocation problem can be formulated as:

$$\begin{aligned} & \max_{[P_m^{(p,d)}]} \frac{R_m^{(p,d)}}{P_m^{(p,d)} + P_c^{(p)}} & (7.15) \\ \text{s. t. } & \text{C1 : } P_m^{(p,d)} \leq P_m^{(p,\max)}, \\ & \text{C2 : } R_m^{(p,d)} \geq R_m^{(p,\min)}. \end{aligned}$$

For the relay transmission mode, when the m th PU selects the k th SU as its relay node, i.e., $\beta_{m,k}^{(c)} = 1$, the energy efficiency of the PU-SU pair can be expressed as

$$\eta_{m,k}^{(p,c)} + \eta_{m,k}^{(s)}. \quad (7.16)$$

Therefore, the optimal power allocation problem for the m th PU and the k th SU can be formulated as:

$$\begin{aligned} & \max_{[P_{m,k}^{(p,s)}, P_{m,k}^{(p,r)}, P_{m,k}^{(s)}]} \frac{R_{m,k}^{(p,c)}}{P_{m,k}^{(p,c)}} + \frac{R_{m,k}^{(s)}}{P_{m,k}^{(s)} + P_c^{(s)}} & (7.17) \\ \text{s. t. } & \text{C1 : } P_{m,k}^{(p,s)} \leq P_m^{(p,\max)}, \\ & \text{C2 : } P_{m,k}^{(p,r)} + P_{m,k}^{(s)} \leq P_k^{(s,\max)}, \\ & \text{C3 : } R_{m,k}^{(p,s)} \geq R_m^{(p,\min)}, \\ & \text{C4 : } R_{m,k}^{(p,r)} \geq R_m^{(p,\min)}, \\ & \text{C5 : } R_{m,k}^{(s)} \geq R_{m,k}^{(s,\min)}. \end{aligned}$$

7.3.3 Equivalent Problem Transformation

In order to solve the optimization problem in (7.17), we exploit the fractional programming approach [82]. As we mentioned earlier, we are considering DF at the relay node. In case $R_{m,k}^{(p,s)} < R_{m,k}^{(p,r)}$, our optimization problem becomes:

$$\begin{aligned}
 & \max_{[P_{m,k}^{(p,s)}, P_{m,k}^{(p,r)}, P_{m,k}^{(s)}]} \frac{R_{m,k}^{(p,s)}}{P_{m,k}^{(p,c)}} + \frac{R_{m,k}^{(s)}}{P_{m,k}^{(s)} + P_c^{(s)}} \quad (7.18) \\
 \text{s. t. } & \text{C1: } P_{m,k}^{(p,s)} \leq P_m^{(p,\max)}, \\
 & \text{C2: } P_{m,k}^{(p,r)} + P_{m,k}^{(s)} \leq P_k^{(s,\max)}, \\
 & \text{C3: } R_{m,k}^{(p,s)} < R_{m,k}^{(p,r)}, \\
 & \text{C4: } R_{m,k}^{(p,s)} \geq R_m^{(p,\min)}, \\
 & \text{C5: } R_{m,k}^{(p,r)} \geq R_m^{(p,\min)}, \\
 & \text{C6: } R_{m,k}^{(s)} \geq R_{m,k}^{(s,\min)}.
 \end{aligned}$$

To proceed, we rewrite the problem in (7.18) into an equivalent form [83]:

$$\begin{aligned}
 & \max_{[P_{m,k}^{(p,s)}, P_{m,k}^{(p,r)}, P_{m,k}^{(s)}, \alpha_1, \alpha_2]} \alpha_1 + \alpha_2 \quad (7.19) \\
 \text{s. t. } & \text{C1} - \text{C6 in (7.18)}, \\
 & \text{C7: } \frac{R_{m,k}^{(p,s)}}{P_{m,k}^{(p,c)}} \geq \alpha_1, \\
 & \text{C8: } \frac{R_{m,k}^{(s)}}{P_{m,k}^{(s)} + P_c^{(s)}} \geq \alpha_2
 \end{aligned}$$

where C7 and C8 denote the energy efficiency constraints.

Theorem 1: If the set $(P_{m,k}^{(p,s)*}, P_{m,k}^{(p,r)*}, P_{m,k}^{(s)*}, \alpha_1^*, \alpha_2^*)$ is the solution for (7.19), then there exist ν and κ such that $(P_{m,k}^{(p,s)*}, P_{m,k}^{(p,r)*}, P_{m,k}^{(s)*})$ satisfies that Karush-Kuhn-Tucker (KKT) conditions for $\nu = \bar{\nu}$, $\kappa = \bar{\kappa}$, $\alpha_1 = \alpha_1^*$, $\alpha_2 = \alpha_2^*$ of the following problem [84]

$$\begin{aligned}
 & \max_{[P_{m,k}^{(p,s)}, P_{m,k}^{(p,r)}, P_{m,k}^{(s)}]} \phi \quad (7.20) \\
 \text{s. t. } & \text{C1} - \text{C6 in (7.18)}
 \end{aligned}$$

where $\phi = \nu(R_{m,k}^{(p,s)} - \alpha_1 P_{m,k}^{(p,c)}) + \kappa(R_{m,k}^{(s)} - \alpha_2(P_{m,k}^{(s)} + P_c^{(s)}))$. Also the set of solutions satisfies a system of equations for $\nu = \bar{\nu}$, $\kappa = \bar{\kappa}$, $\alpha_1 = \alpha_1^*$, and $\alpha_2 = \alpha_2^*$, with

$$\begin{cases} \bar{\nu} = \frac{1}{P_{m,k}^{(p,c)}} & \bar{\kappa} = \frac{1}{P_{m,k}^{(s)} + P_c^{(s)}} \\ \alpha_1^* = \frac{R_{m,k}^{(p,s)}}{P_{m,k}^{(p,c)}} & \alpha_2^* = \frac{R_{m,k}^{(s)}}{P_{m,k}^{(s)} + P_c^{(s)}} \end{cases} \quad (7.21)$$

Proof for Theorem 1 is provided in Appendix D.

In Theorem 1 we proved that by satisfying the system of equations in (7.21) among the solutions of (7.20), the optimization problem in (7.18) can be solved. It shows as well that for an optimization problem with an objective function in fractional form, there exists an equivalent in subtractive form, i.e., ϕ in our case. As a result, we use the equivalent objective function for the rest of the work.

7.3.4 Energy Efficiency Maximization

In this section we present an iterative algorithm in order to find solutions for the problem in (7.20). After transforming our problem (7.18) into (7.20), it can be easily proven that the transformed problem is convex and can be solved using the Lagrange dual method [85], [86]. Thus, by relaxing the constraints the Lagrange function can be represented as

$$\begin{aligned} \mathcal{L}(P_{m,k}^{(p,r)}, P_{m,k}^{(p,s)}, P_{m,k}^{(s)}, \lambda, \delta, \epsilon, \xi, \theta, \mu, \nu, \kappa) = & \\ & + \nu(R_{m,k}^{(p,s)} - \alpha_1(P_{m,k}^{(p,c)})) + \kappa(R_{m,k}^{(s)} - \alpha_2(P_{m,k}^{(s)} + P_c^{(s)})) \\ & + \lambda(P_m^{(p,\max)} - P_{m,k}^{(p,s)}) + \delta(P_k^{(s,\max)} - P_{m,k}^{(p,r)} - P_{m,k}^{(s)}) \\ & + \epsilon(R_{m,k}^{(p,r)} - R_{m,k}^{(p,s)}) + \xi(R_{m,k}^{(p,s)} - R_m^{(p,\min)}) \\ & + \delta(R_{m,k}^{(p,r)} - R_m^{(p,\min)}) + \mu(R_{m,k}^{(s)} - R_k^{(s,\min)}) \end{aligned} \quad (7.22)$$

where $\lambda, \delta > 0$ and $\epsilon, \xi, \theta, \mu > 0$ represent the Lagrange multipliers associated with power constraints and minimum data rate requirements, respectively. The corresponding Lagrange dual method can be expressed as follows:

$$\min_{[\lambda, \delta, \epsilon, \xi, \theta, \mu]} \max_{[P_{m,k}^{(p,r)}, P_{m,k}^{(p,s)}, P_{m,k}^{(s)}]} \mathcal{L} \quad (7.23)$$

$$\text{s. t. } \lambda \geq 0, \delta \geq 0, \epsilon \geq 0, \xi \geq 0, \theta \geq 0, \mu \geq 0.$$

The above dual problem can be solved by optimizing the transmit power for a fixed set of Lagrange multipliers, and updating the Lagrange multipliers iteratively as well as our parameters $\nu, \kappa, \alpha_1, \alpha_2$. For a given set of Lagrange multipliers $\lambda, \delta, \epsilon, \xi, \theta, \mu$, the locally optimal transmit powers can be obtained through calculating the derivative of $\mathcal{L}(P_{m,k}^{(p,r)}, P_{m,k}^{(p,s)}, P_{m,k}^{(s)}, \lambda, \delta, \epsilon, \xi, \theta, \mu)$ over the transmit powers and setting it to zero thus obtaining

$$P_{m,k}^{(p,s)*} = \left[\frac{t_1 \rho_m B(\nu + \xi - \epsilon)}{(\lambda + \nu \alpha_1) \ln 2} - \frac{\sigma^2}{h_{m,k}^{(p,s)}} \right]^+ \quad (7.24)$$

$$P_{m,k}^{(p,r)*} = \left[\frac{(1 - t_1) \rho_m B(\epsilon + \theta)}{(\delta + \nu \alpha_1) \ln 2} - \frac{\sigma^2}{h_{m,k}^{(p,r)}} \right]^+ \quad (7.25)$$

$$P_{m,k}^{(s)*} = \left[\frac{(1 - \rho_m) B(\mu + \kappa)}{(\delta + \kappa \alpha_2) \ln 2} - \frac{\sigma^2}{h_{m,k}^{(s)}} \right]^+ \quad (7.26)$$

where $[z]^+ = \max(0, z)$.

In case $R_{m,k}^{(p,s)} \geq R_{m,k}^{(p,r)}$, a similar approach can be followed, leading to the optimization problem:

$$\begin{aligned} & \max_{[P_{m,k}^{(p,s)}, P_{m,k}^{(p,r)}, P_{m,k}^{(s)}]} \frac{R_{m,k}^{(p,s)}}{P_{m,k}^{(p,c)}} + \frac{R_{m,k}^{(s)}}{P_{m,k}^{(s)} + P_c^{(s)}} \quad (7.27) \\ \text{s. t. } & \text{C1: } P_{m,k}^{(p,s)} \leq P_m^{(p,\max)}, \\ & \text{C2: } P_{m,k}^{(p,r)} + P_{m,k}^{(s)} \leq P_k^{(s,\max)}, \\ & \text{C3: } R_{m,k}^{(p,s)} \geq R_{m,k}^{(p,r)}, \\ & \text{C4: } R_{m,k}^{(p,s)} \geq R_m^{(p,\min)}, \\ & \text{C5: } R_{m,k}^{(p,r)} \geq R_m^{(p,\min)}, \\ & \text{C6: } R_{m,k}^{(s)} \geq R_{m,k}^{(s,\min)}. \end{aligned}$$

By applying to (7.27) the same transformation explained in Theorem 1 and applying Lagrange dual method to the transformed problem, we are able to calculate the transmit powers:

$$P_{m,k}^{(p,s)*} = \left[\frac{t_1 \rho_m B(\xi + \epsilon)}{(\lambda + \nu \alpha_1) \ln 2} - \frac{\sigma^2}{h_{m,k}^{(p,s)}} \right]^+ \quad (7.28)$$

$$P_{m,k}^{(p,r)*} = \left[\frac{(1 - t_1) \rho_m B(\nu - \epsilon + \theta)}{(\delta + \nu \alpha_1) \ln 2} - \frac{\sigma^2}{h_{m,k}^{(p,r)}} \right]^+ \quad (7.29)$$

$$P_{m,k}^{(s)*} = \left[\frac{(1 - \rho_m)B(\mu + \kappa)}{(\delta + \kappa\alpha_2)\ln 2} - \frac{\sigma^2}{h_{m,k}^{(s)}} \right]^+ \quad (7.30)$$

Based on these solutions, we propose a two-layer optimization algorithm. In the inner layer the Lagrange multipliers in (7.24)-(7.26) and (7.28)-(7.30) can be updated through using the subgradient method [87], i.e.,

$$\lambda(n+1) = [\lambda(n) - \psi(P_m^{(p,\max)} - P_{m,k}^{(p,s)})]^+ \quad (7.31)$$

$$\delta(n+1) = [\delta(n) - \psi(P_k^{(s,\max)} - P_{m,k}^{(p,r)} - P_{m,k}^{(s)})]^+ \quad (7.32)$$

$$\epsilon(n+1) = [\epsilon(n) - \psi |R_{m,k}^{(p,r)} - R_{m,k}^{(p,s)}|]^+ \quad (7.33)$$

$$\xi(n+1) = [\xi(n) - \psi(R_{m,k}^{(p,s)} - R_m^{(p,\min)})]^+ \quad (7.34)$$

$$\theta(n+1) = [\theta(n) - \psi(R_{m,k}^{(p,r)} - R_m^{(p,\min)})]^+ \quad (7.35)$$

$$\mu(n+1) = [\mu(n) - \psi(R_{m,k}^{(s)} - R_k^{(s,\min)})]^+ \quad (7.36)$$

where ψ denotes the learning rate.

In the outer layer the parameters $\nu, \kappa, \alpha_1, \alpha_2$ can be updated using Newton-Raphson method [88], i.e.,

$$\nu(n+1) = \nu(n) - \chi \left(\frac{\nu(n)P_{m,k}^{(p,c)} - 1}{P_{m,k}^{(p,c)}} \right) \quad (7.37)$$

$$\kappa(n+1) = \kappa(n) - \chi \left(\frac{\kappa(P_{m,k}^{(s)} + P_c^{(s)}) - 1}{P_{m,k}^{(s)} + P_c^{(s)}} \right) \quad (7.38)$$

$$\alpha_1(n+1) = \alpha_1(n) - \chi \left(\frac{\alpha_1(n)P_{m,k}^{(p,c)} - \tau}{P_{m,k}^{(p,c)}} \right) \quad (7.39)$$

$$\alpha_2(n+1) = \alpha_2(n) - \chi \left(\frac{\alpha_2(n)(P_{m,k}^{(s)} + P_c^{(s)}) - R_{m,k}^{(s)}}{P_{m,k}^{(s)} + P_c^{(s)}} \right) \quad (7.40)$$

where χ denotes the learning rate and $\tau = \min(R_{m,k}^{(p,s)}, R_{m,k}^{(p,r)})$. Detailed steps of our algorithm are shown in Algorithm 7.1.

For the problem in (7.15), a similar approach can be followed. By transforming it using Theorem 1 and applying the Lagrange dual method, the optimal transmit power for the direct mode can be obtained.

Algorithm 7.1 Power Allocation Optimization

- 1: Set tolerance ζ and maximum number of iterations n_{\max}
 Let $n = 0$, choose $\psi \in (0, 1)$, $\chi \in (0, 1)$
 Choose arbitrarily $P_{m,k}^{(p,s)}(0)$, $P_{m,k}^{(p,r)}(0)$, $P_{m,k}^{(s)}(0)$ such that satisfies
 power constraints
 Calculate $R_{m,k}^{(p,s)}(0)$, $R_{m,k}^{(p,r)}(0)$ and $R_{m,k}^{(s)}(0)$
if $R_{m,k}^{(p,s)} < R_{m,k}^{(p,r)}$
 then $\tau = R_{m,k}^{(p,s)}$
 else $\tau = R_{m,k}^{(p,r)}$
end
 Let

$$\begin{cases} \nu(n) = \frac{1}{P_{m,k}^{(p,c)}(n)} \\ \kappa(n) = \frac{1}{P_{m,k}^{(s)}(n) + P_c^{(s)}} \\ \alpha_1(n) = \frac{\tau}{P_{m,k}^{(p,c)}(n)} \\ \alpha_2(n) = \frac{R_{m,k}^{(s)}(n)}{P_{m,k}^{(s)}(n) + P_c^{(s)}} \end{cases}$$

- Initialize the Lagrange multipliers $\lambda, \delta, \epsilon, \xi, \theta, \mu$
 - 2: **if** $\tau = R_{m,k}^{(p,s)}$
 update $P_{m,k}^{(p,s)}$ and $P_{m,k}^{(p,r)}$ with (7.24) and (7.25) and
 obtain $P_{m,k}^{(p,s)*}$ and $P_{m,k}^{(p,r)*}$
 else
 update $P_{m,k}^{(p,s)}$ and $P_{m,k}^{(p,r)}$ with (7.28) and (7.29) and
 obtain $P_{m,k}^{(p,s)*}$ and $P_{m,k}^{(p,r)*}$
 end
 Update $P_{m,k}^{(s)}$ with (7.26) and obtain $P_{m,k}^{(s)*}$
 - 3: Update the Lagrange multipliers using (7.31)-(7.36)
 - 4: Compute ϕ^* with $P_{m,k}^{(p,s)*}$, $P_{m,k}^{(p,r)*}$ and $P_{m,k}^{(s)*}$
 if $|\phi^* - \phi^{(n)}| \leq \zeta$
 $P_{m,k}^{(p,s)}(n+1) = P_{m,k}^{(p,s)*}$, $P_{m,k}^{(p,r)}(n+1) = P_{m,k}^{(p,r)*}$, $P_{m,k}^{(s)}(n+1) = P_{m,k}^{(s)*}$
 exit program (convergence reached)
 else
 $P_{m,k}^{(p,s)}(n) = P_{m,k}^{(p,s)*}$, $P_{m,k}^{(p,r)}(n) = P_{m,k}^{(p,r)*}$, $P_{m,k}^{(s)}(n) = P_{m,k}^{(s)*}$
 $\phi(n) = \phi^*$
 update $\nu, \kappa, \alpha_1, \alpha_2$ using (7.37)-(7.40)
 Update $R_{m,k}^{(p,s)}(n+1)$, $R_{m,k}^{(p,r)}(n+1)$, $R_{m,k}^{(s)}(n+1)$
 $n \leftarrow n + 1$
 end
 go to step 2 unless n reached n_{\max}
-

Table 7.1: Tables of direct mode and cooperative mode

(a) Direct mode		(b) Cooperative mode				
	Direct Mode		Coop. with SU ₁	Coop. with SU ₂	⋯	Coop. with SU _K
PU ₁	η_1^*	PU ₁	$\eta_{1,1}^*$	$\eta_{1,2}^*$	⋯	$\eta_{1,K}^*$
PU ₂	η_2^*	PU ₂	$\eta_{2,1}^*$	$\eta_{2,2}^*$	⋯	$\eta_{2,K}^*$
⋯		⋯	⋯			⋯
PU _M	η_M^*	PU _M	$\eta_{M,1}^*$	$\eta_{M,2}^*$	⋯	$\eta_{M,K}^*$

7.3.5 Transmission Mode and Relay Selection Subproblem

Given the optimal transmit power of the PUs and the SUs, the total energy efficiency of the network can be calculated as:

$$\eta^* = \sum_{m=1}^M \sum_{k=1}^K (\beta_m^{(d)} \eta_m^* + \beta_{m,k}^{(c)} \eta_{m,k}^*). \quad (7.41)$$

The transmission mode and relay selection subproblem can be formulated as:

$$\begin{aligned} & \max_{[\beta_m^{(d)}, \beta_{m,k}^{(c)}]} \eta^* & (7.42) \\ \text{s. t. } & \text{C1: } \beta_m^{(d)} + \sum_{k=1}^K \beta_{m,k}^{(c)} \leq 1, \\ & \text{C2: } \sum_{m=1}^M \beta_{m,k}^{(c)} \leq 1. \end{aligned}$$

which is a linear binary optimization problem, that can be solved using graph-based optimization method. To implement such optimization problem, we construct two tables: Table 7.1a, whose columns contain the maximum energy efficiency when the m th PU chooses direct transmission mode; Table 7.1b, which contain the optimal energy efficiency when the m th PU chooses the k th SU as a relay node for cooperation mode.

It can be seen that the optimal transmission mode and relay selection solution of (7.42) is equivalent to finding the maximum sum of the energy efficiency elements which are chosen from various rows and columns, except for the direct mode. From (7.42), we can see that when the energy efficiency of the m th PU obtained in direct mode is larger than all of the energy efficiency of the PU obtained in cooperative

mode, the PU should choose the direct mode. Hence, to solve the optimization problem formulated in (7.42), for the m th row, $1 \leq m \leq M$, we first compare the element in direct mode with the other elements in the same row number in Table 7.1b; if the energy efficiency of the PU obtained in direct mode is the largest, then we set $\beta_m^{(d)} = 1$, $\beta_{m,k}^{(c)} = 0$, and delete the corresponding row in Table 7.1b. For the remaining, we can solve the optimal relay selection subproblem for cooperation transmission mode.

Given the constraints on both PUs and SUs, the optimal relay selection subproblem can be described as a bipartite graph, and the problem of finding the optimal relay can be regarded as an optimal matching algorithm in the bipartite graph that can be solved by a modified Kuhn-Munkres (K-M) algorithm [5, 89, 90]. A brief description of this algorithm and its complexity is presented in Appendix E.

Based on the optimal relay selection results, we obtain the corresponding energy efficiency for cooperative mode, which is compared with that obtained from the direct mode for each PU. If the latter is larger, we set in direct mode the corresponding PU and rerun the K-M algorithm until the optimal energy efficiency obtained for cooperative mode is larger than that from the direct mode for all the PUs. In Algorithm 7.2, we present a brief description of the algorithm.

7.4 Numerical Results

In this section, we evaluate the system performance and effectiveness of the proposed solution throughout Monte Carlo simulations. A single PUs' cell of 250 m radius is considered (see Fig. 6.1), and a summary of the scenario parameters are shown in Table 7.2. Results are obtained averaging over 5000 independent configuration snapshots, each one with different PUs' and SUs' positions within the cell (PUs and SUs are uniformly distributed within the area), and independent realizations of shadowing and fading. Regarding the time slot subdivision between PU and SU, we initially assume $t_1 = T/2$, which is the choice maximizing energy efficiency, as shown in Section 7.4.6.

Algorithm 7.2 Transmission Mode and Relay Selection Optimization

- 1: Solving optimal power allocation subproblem
to obtain η_m^* and $\eta_{m,k}^*$, construct Table 7.1
 - 2: **for** the m th PU
 - if** $\eta_m^* > \eta_{m,k}^*, \forall 1 \leq k \leq K$
 - then**
 - set $\beta_m^{(p,d)} = 1$
 - delete the m th row in Table 7.1b
 - end**
 - end**

Table 7.1b is updated
 - 3: **repeat**
 - 4: Apply K-M algorithm on Table 7.1b to find
optimal relay node obtaining $\beta_{m,k}^{(c)}$
 - 5: **if** $\beta_{m,k}^{(c)}\eta_{m,k}^* < \eta_m^*, 1 \leq m \leq M$
 - set $\beta_m^{(p,d)} = 1$
 - set $\beta_{m,k}^{(c)} = 0$

Update Table 7.1b removing the m th row
 - end**
 - 6: **until** $\beta_{m,k}^{(c)}\eta_{m,k}^* > \eta_m^*, \forall \text{ PU}_m$ in Table 7.1b.
-

Table 7.2: System parameters

Cell radius	250 m
Small scale fading distribution	Rayleigh fading
Carrier frequency	3.5 GHz
Bandwidth	50 MHz
Noise power per link, σ^2	-90 dBm
Shadowing, $s_{m,k}^{(p,s)}$	Standard deviation of 8 dB
Average channel gain at 1 m, k_0	-39 dB
Path-loss exponent, γ	3
Circuit power per UE (PU or SU), P_c	20 dBm
Maximum transmit power per UE, P_{\max}	24 dBm
Minimum data rate constraint, $R_m^{(p,\min)}$	100 Mbit/s
Fraction of bandwidth, ρ_m	0.66

7.4.1 Convergence of the Iterative Algorithm

In Fig. 7.1, we show the energy efficiency in deciBel, i.e., $\eta(\text{dB}) = 10 \log_{10} \eta$, for different values of PUs' and SUs' circuit power, P_c , as a function of the number of iterations, to illustrate the convergence of the proposed algorithm. It can be seen that the iterative algorithm generates a nondecreasing sequence and converges to a stable point within 15 iterations. In addition, we can observe the effect of P_c to energy efficiency. As expected, the energy efficiency decreases with the increase of P_c .

7.4.2 Energy Efficiency Versus Maximum Transmit Power

In Fig. 7.2, the average energy efficiency varying the maximum transmit power, P_{\max} , is presented. The number of PUs and SUs is chosen randomly at every adaptation with a maximum number of 10 PUs and 10 SUs. From the figure, it can be observed that the energy efficiency increases with an increase of P_{\max} up to approximately 0.1W, beyond which the energy efficiency saturates. Besides, we compare the performance of our solution with three different algorithms:

- A random choice algorithm in which PUs choose cooperative relays randomly.

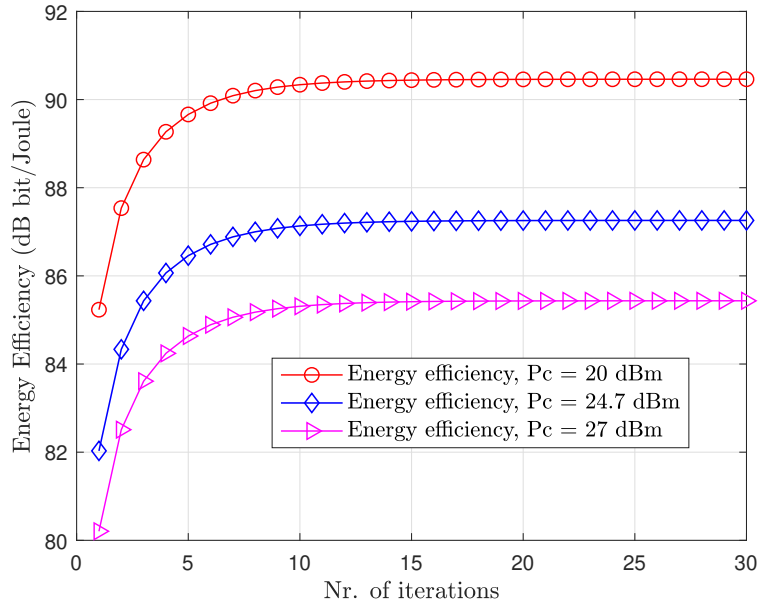


Figure 7.1: Energy efficiency versus number of iterations with $M = 10$ and $K = 10$, for different circuit power consumption P_c .

- A non-cooperative approach in which a similar system model is considered but PUs choose relays to increase their own energy efficiency, instead of maximizing the total energy efficiency of the system.
- A system in which there are only PUs, and therefore only direct transmission is possible.

As can be observed, the proposed algorithm outperforms the other three solutions. In addition, compared to a system where only PUs are present, we can show that with our approach having the same available spectrum, higher energy efficiency can be achieved, and also more users are able to use the resources available.

7.4.3 Energy Efficiency Versus Number of PUs

Fig. 7.3 illustrates the effect that an increasing number of PUs have on energy efficiency when the number of SUs is set to 10. When the number of PUs is smaller than the number of SUs, we can observe a higher energy efficiency achieved. However, increasing the number of PUs, the energy efficiency decreases because of the increased contention of PUs to choose the most convenient cooperative relay. When the number of PUs becomes larger than the number of SUs, the decline of the curve

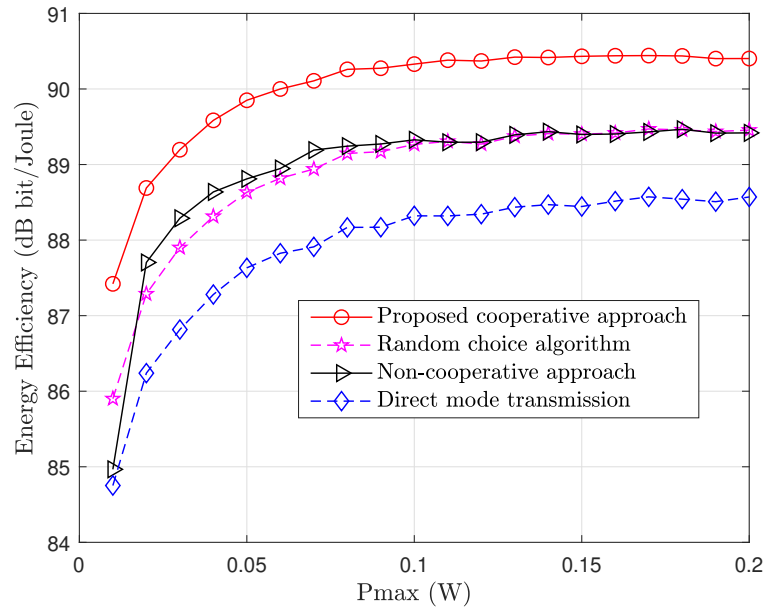


Figure 7.2: Energy efficiency varying the maximum transmit power. Three different algorithms are compared. M and K in this case change randomly from 1 to 10.

becomes sharper. This comes from the fact that not every PU can choose a cooperative relay and is bounded to perform a direct transmission. As we have shown before, the energy efficiency based only on direct transmission is lower than the one based on the cooperative relay.

7.4.4 Energy Efficiency Versus Path Loss Exponent

In Fig. 7.4, the average energy efficiency varying the path-loss exponent, γ , is presented. With the increase of γ , the energy efficiency decreases; this is due to the increased attenuation, which reflects in a lower data rate. Also, it can be seen that our algorithm outperforms the energy efficiency obtained from the scheme proposed in [66], in which only PUs' power is optimized, the non-cooperative approach, as well as a system where only PUs are present. In harsh propagation environments with $\gamma > 3.5$, the energy efficiency of the proposed algorithm outperforms the direct transmission scenario by approximately 110% and the proposed scheme in [66] by 10 percentage points.

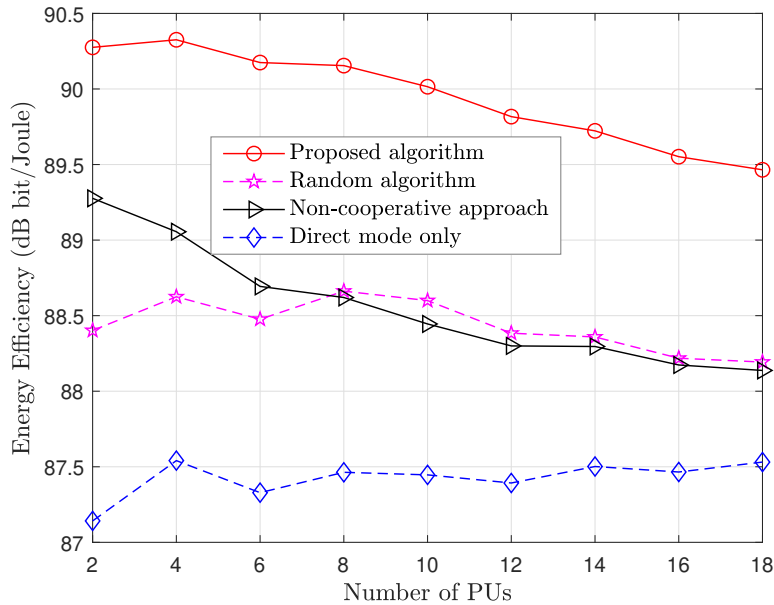


Figure 7.3: Energy efficiency varying number of PUs. M varies from 2 to 18 and $K = 10$.

7.4.5 Energy Efficiency Versus Shadowing Standard Deviation

In Fig. 7.5, we illustrate the average energy efficiency varying the shadowing standard deviation. As can be seen, also considering the previous figure, the proposed algorithm is more robust to shadowing and attenuation hence offers better performance in harsh propagation environments. The proposed scheme outperforms the direct transmission scenario by 72% and the proposed scheme in [66] by nearly 20 percentage points.

7.4.6 Energy Efficiency Versus Time Slot Division

In Fig. 7.6, is illustrated the average energy efficiency varying the time slot division chosen in the two relay transmission links. As we notice in the figure, when both links have the same duration, we can achieve the highest value of energy efficiency. In addition, it can be observed that the variation between the maximum, for $t_1/T = 0.5$, and minimum value, for $t_1/T = 0.9$, of energy efficiency is not very high. This fact confirms the robustness of the proposed algorithm to the choice of the time slot division in the relay transmission.

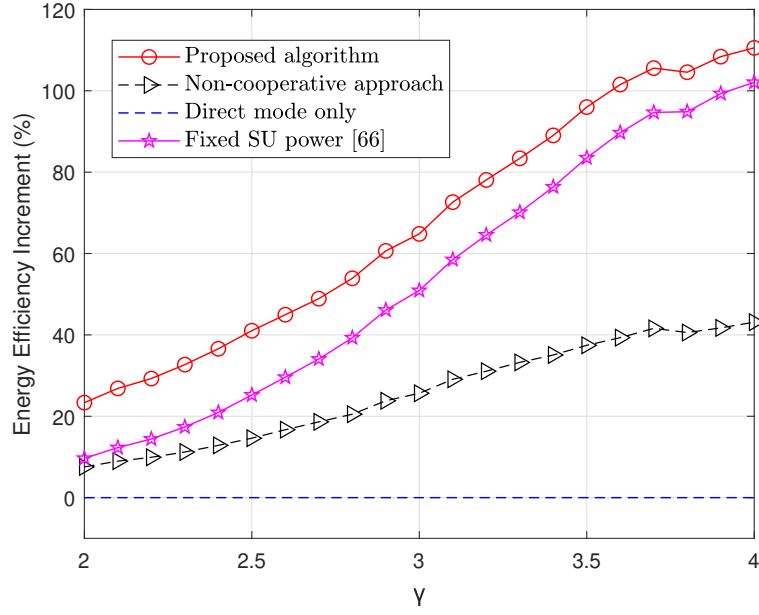


Figure 7.4: Energy efficiency increment with respect to direct mode varying the path loss exponent. M and K change randomly from 1 to 15 while $\sigma_s = 8\text{dB}$.

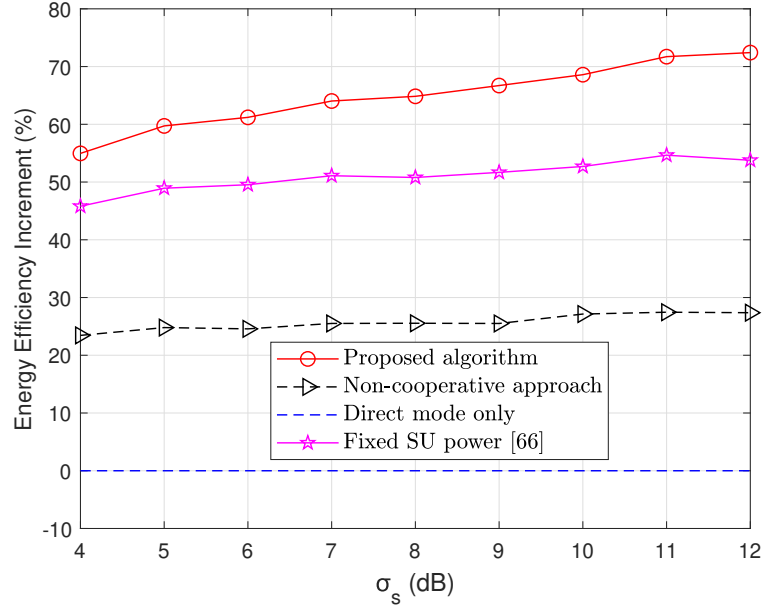


Figure 7.5: Energy efficiency increment with respect to direct mode versus shadowing standard deviation. M and K in this case change randomly within 1 and 15 while $\gamma = 3$.

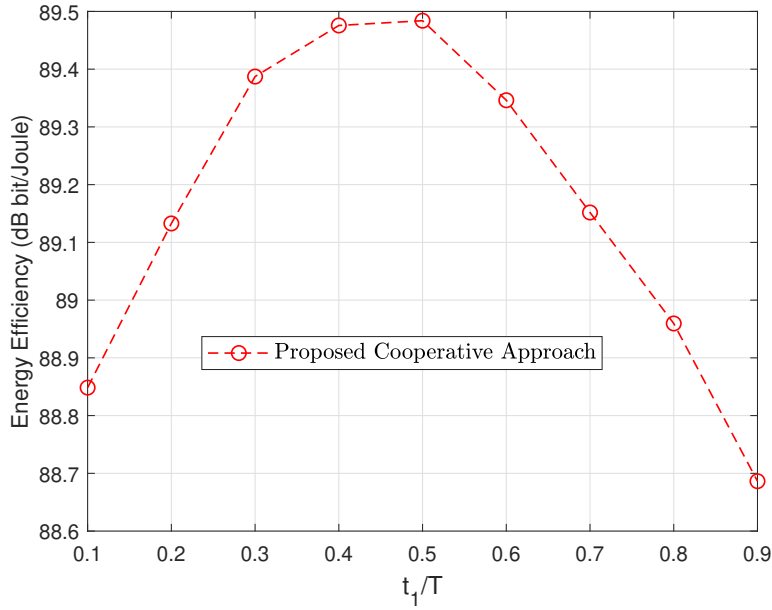


Figure 7.6: Energy efficiency versus time slot division in the relay transmission link. The parameters M and K are random variables uniformly distributed from 1 to 10.

7.5 Future incorporation with RT models

In the above presented work, the propagation channel was modelled using a stochastic channel model with a Rayleigh distributed r.v. and a log-normal r.v. with a shadowing parameter. In future, instead of stochastic model, a deterministic one like RT will be used. In addition, a real environment will be taken in consideration and modelled into the RT. In this way, the results can be seen from two different propagation modelling and comparison between them can give us a better understanding of which model to use for future works.

Chapter 8

Conclusions

In the first part of this thesis, a new dynamic ray tracing approach that can perform a deterministic ray-based prediction in a moving environment, was presented. This new algorithm allows to extend ray tracing prediction over a given multipath coherence time using an analytical formulation, assuming constant accelerations for moving objects. In addition, through DRT, the computation of the Doppler's shifts for each ray can be completed within a single run.

This new approach is shown to give the same results as multiple RT runs on successive environment configurations at a fraction of the computation time, with a speed up of the order of 48x. Additionally, DRT was validated over two case studies: 1) ideal street canyon, and 2) comparison with measurements in an intersection. Future work will be concentrated on validating DRT in different vehicular scenarios. In addition, the extrapolation time or coherence time which is related to the lifetime of rays has to be known in advance. So a formulation regarding this lifetime of rays need to be further explored.

The second part of the thesis, was dedicated to the presentation of novel energy-efficient architecture for CRN is proposed where each PU can choose one SU as a relay node. To encourage the cooperative behaviour of the SUs, PU lease a fraction of their allocated spectrum to the relay SUs to transmit their data. In addition, a centralized resource management network architecture to achieve a performance enhancement of the cell. The resource allocation problem is formulated as a constrained sum energy efficiency maximization problem. Meanwhile, a modified K-M algorithm is used to solve the transmission mode and relay selection sub-problem.

System simulation performed in a typical multiuser case show that the proposed algorithm converges to the solution within a small number of iterations. Furthermore, the proposed algorithm shows a robustness to the choice of time division in the relay transmission.

Appendix A

Doppler frequency calculation

One of the advantages of the DRT approach is the computation of Doppler information online in the algorithm with the aid of simple formulas. In such a way, there is no need to consider successive “snapshots” of the environment with slightly different displacements of the objects, and then to calculate the Doppler shifts with a “finite difference” computation method.

When TX and RX are both moving, the resulting apparent frequency f' , including the Doppler frequency shift f_D is computed for the LoS ray using the following equation:

$$f' = f_0 + f_D = f_0 \left(\frac{c - \bar{v}_{RX} \cdot \hat{k}}{c - \bar{v}_{TX} \cdot \hat{k}} \right) \quad (\text{A.1})$$

where (\cdot) represents the vector dot product operator, f_0 is the carrier frequency of the transmitted signal, \hat{k} is the unit vector of the ray's direction from TX towards RX, and \bar{v}_{TX} , \bar{v}_{RX} are the velocities of transmitter and receiver, respectively.

This formula can be extended to rays with multiple bounces, where we have n scattering points, each one moving with different speed (see Fig. A.1):

$$f' = f_0 + f_D = f_0 \prod_{i=1}^{n+1} \left(\frac{c - \bar{v}_i \cdot \hat{k}_i}{c - \bar{v}_{i-1} \cdot \hat{k}_i} \right) \quad (\text{A.2})$$

where \bar{v}_i , $i = 1, 2, \dots, n$ is the velocity of the i -th interaction point, $\bar{v}_0 = \bar{v}_{TX}$, and $\bar{v}_{n+1} = \bar{v}_{RX}$, respectively.

Equation (A.2) assumes that the velocities of the interaction points on the objects are known. In the simplified case of small scattering objects that can be approximated as “point scatterers”, no further processing is needed, and we can directly apply eq. (A.2).

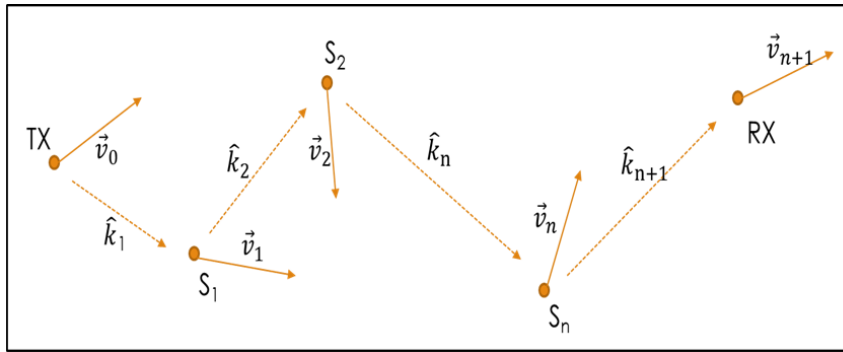


Figure A.1: Representation of the multiple scatterers Doppler model

Instead, in the case of large objects we need to compute the velocity of the interaction points on the object surface as explained in Chapter 4.

Appendix B

Reflection points' velocity and acceleration calculation

Given the reflection point position (Q_R), its velocity (\bar{v}_{Q_R}) can be determined by deriving eq. (4.2) with respect to time. The x-component of \bar{v}_{Q_R} can be calculated as:

$$\begin{aligned} v_{Q_R,x} &= \frac{\partial x_{Q_R}}{\partial t} = \frac{\partial x_{Q_R}}{\partial x_{TX}} \frac{\partial x_{TX}}{\partial t} + \frac{\partial x_{Q_R}}{\partial y_{TX}} \frac{\partial y_{TX}}{\partial t} \\ &\quad + \frac{\partial x_{Q_R}}{\partial x_{RX}} \frac{\partial x_{RX}}{\partial t} + \frac{\partial x_{Q_R}}{\partial y_{RX}} \frac{\partial y_{RX}}{\partial t} \\ &= f_{x_{TX}} + f_{y_{TX}} + f_{x_{RX}} + f_{y_{RX}}, \end{aligned} \tag{B.1}$$

with

$$\begin{aligned} f_{x_{TX}} &= \frac{\partial x_{Q_R}}{\partial x_{TX}} v_{TX,x} \\ f_{y_{TX}} &= \frac{\partial x_{Q_R}}{\partial y_{TX}} v_{TX,y} \\ f_{x_{RX}} &= \frac{\partial x_{Q_R}}{\partial x_{RX}} v_{RX,x} \\ f_{y_{RX}} &= \frac{\partial x_{Q_R}}{\partial y_{RX}} v_{RX,y}. \end{aligned}$$

The partial derivatives in (B.1) can be easily computed by deriving x_{Q_R} w.r.t.

the x, y coordinates of TX and RX:

$$\begin{aligned}\frac{\partial x_{Q_R}}{\partial x_{TX}} &= 1 - \frac{y_{TX}}{y_{TX} + y_{RX}} \\ \frac{\partial x_{Q_R}}{\partial y_{TX}} &= \frac{y_{RX}(x_{RX} - x_{TX})}{(y_{RX} + y_{TX})^2} \\ \frac{\partial x_{Q_R}}{\partial x_{RX}} &= \frac{y_{TX}}{y_{TX} + y_{RX}} \\ \frac{\partial x_{Q_R}}{\partial y_{RX}} &= \frac{-y_{RX}(x_{RX} - x_{TX})}{(y_{RX} + y_{TX})^2}\end{aligned}$$

and substituting these expressions in (B.1) we finally get $v_{Q_R, x}$.

By following the same method as above, we can obtain the z-component of the velocity, $v_{Q_R, z}$, by time deriving the z-coordinate of Q_R (z_{Q_R}).

A similar procedure is used to calculate \bar{a}_{Q_R} by deriving \bar{v}_{Q_R} with respect to time:

$$\begin{aligned}a_{Q_R, x} &= a_{Q_R, x}^{(1)} + a_{Q_R, x}^{(2)} + a_{Q_R, x}^{(3)} + a_{Q_R, x}^{(4)} \\ &= \frac{\partial}{\partial t} f_{x_{TX}} + \frac{\partial}{\partial t} f_{y_{TX}} + \frac{\partial}{\partial t} f_{x_{RX}} + \frac{\partial}{\partial t} f_{y_{RX}}\end{aligned}\tag{B.2}$$

For the sake of brevity, we report below only the computation of the first partial derivative in eq. (B.2):

$$\begin{aligned}a_{Q_R, x}^{(1)} &= \frac{\partial}{\partial t} f_{x_{TX}} = \frac{\partial}{\partial t} \frac{\partial x_{Q_R}}{\partial x_{TX}} \frac{\partial x_{TX}}{\partial t} + \frac{\partial x_{Q_R}}{\partial x_{TX}} \frac{v_{TX, x}}{\partial t} \\ &= \left(\frac{\partial^2 x_{Q_R}}{\partial x_{TX} \partial y_{TX}} \frac{\partial y_{TX}}{\partial t} + \frac{\partial^2 x_{Q_R}}{\partial x_{TX} \partial y_{RX}} \frac{\partial y_{RX}}{\partial t} \right) v_{TX, x} \\ &\quad + \frac{\partial x_{Q_R}}{\partial x_{TX}} a_{TX, x} \\ &= \left(\frac{\partial^2 x_{Q_R}}{\partial x_{TX} \partial y_{TX}} v_{TX, y} + \frac{\partial^2 x_{Q_R}}{\partial x_{TX} \partial y_{RX}} v_{RX, y} \right) v_{TX, x} \\ &\quad + \frac{\partial x_{Q_R}}{\partial x_{TX}} a_{TX, x}\end{aligned}\tag{B.3}$$

where the partial derivatives in (B.3) are expressed by:

$$\begin{aligned}\frac{\partial x_{Q_R}}{\partial x_{TX}} &= 1 - \frac{y_{TX}}{y_{TX} + y_{RX}} \\ \frac{\partial^2 x_{Q_R}}{\partial x_{TX} \partial y_{TX}} &= \frac{-y_{RX}}{(y_{TX} + y_{RX})^2} \\ \frac{\partial^2 x_{Q_R}}{\partial x_{TX} \partial y_{RX}} &= \frac{y_{TX}}{(y_{TX} + y_{RX})^2}.\end{aligned}$$

By substituting these expressions in (B.3) we obtain $a_{Q_R,x}^{(1)}$.

By repeating the same procedure for the remaining components of $a_{Q_R,x}$, we finally get:

$$\begin{aligned}
 a_{Q_R,x} = & \left(\frac{\partial^2 x_{Q_R}}{\partial x_{TX} \partial y_{TX}} v_{TX,y} + \frac{\partial^2 x_{Q_R}}{\partial x_{TX} \partial y_{RX}} v_{RX,y} \right) v_{TX,x} \\
 & + \frac{\partial x_{Q_R}}{\partial x_{TX}} a_{TX,x} + \left(\frac{\partial^2 x_{Q_R}}{\partial y_{TX} \partial x_{TX}} v_{TX,x} + \frac{\partial^2 x_{Q_R}}{\partial y_{TX} \partial x_{RX}} v_{RX,x} \right) v_{TX,y} \\
 & + \left(\frac{\partial^2 x_{Q_R}}{\partial y_{TX}^2} v_{TX,y} + \frac{\partial^2 x_{Q_R}}{\partial y_{TX} \partial y_{RX}} v_{RX,y} \right) v_{TX,y} + \frac{\partial x_{Q_R}}{\partial y_{TX}} a_{TX,y} \\
 & + \left(\frac{\partial^2 x_{Q_R}}{\partial x_{RX} \partial y_{TX}} v_{TX,y} + \frac{\partial^2 x_{Q_R}}{\partial x_{RX} \partial y_{RX}} v_{RX,y} \right) v_{RX,x} + \frac{\partial x_{Q_R}}{\partial x_{RX}} a_{RX,y} \\
 & + \left(\frac{\partial^2 x_{Q_R}}{\partial y_{RX} \partial x_{TX}} v_{TX,x} + \frac{\partial^2 x_{Q_R}}{\partial y_{RX} \partial x_{RX}} v_{RX,x} \right) v_{RX,y} \\
 & + \left(\frac{\partial^2 x_{Q_R}}{\partial y_{RX} \partial y_{TX}} v_{TX,y} + \frac{\partial^2 x_{Q_R}}{\partial y_{RX}^2} v_{RX,x} \right) v_{RX,x} + \frac{\partial x_{Q_R}}{\partial y_{RX}} a_{RX,y}.
 \end{aligned} \tag{B.4}$$

A similar approach can be adopted to compute the z-component of \bar{a}_{Q_R} .

Appendix C

Diffraction Point's Velocity and Acceleration Calculation

Time derivation of (4.15), gives us the z-component of the diffraction point instantaneous velocity:

$$\begin{aligned}
 v_{Q_D,z} &= \frac{\partial z_{Q_D}}{\partial t} = \frac{\partial z_{RX}}{\partial t} + \frac{\partial}{\partial t} \left(\frac{d_{RX}}{d_{RX} + d_{TX}} (z_{TX} - z_{RX}) \right) \\
 &= v_{RX,z} + \frac{d_{RX}}{d_{RX} + d_{TX}} (v_{TX,z} - v_{RX,z}) \\
 &\quad + (z_{TX} - z_{RX}) \frac{\partial}{\partial t} \left(\frac{d_{RX}}{d_{RX} + d_{TX}} \right)
 \end{aligned} \tag{C.1}$$

where

$$\frac{\partial}{\partial t} \left(\frac{d_{RX}}{d_{TX} + d_{RX}} \right) = \frac{\frac{\partial d_{RX}}{\partial t} (d_{RX} + d_{TX}) - \left(\frac{\partial d_{RX}}{\partial t} + \frac{\partial d_{TX}}{\partial t} \right) d_{RX}}{(d_{TX} + d_{RX})^2} \tag{C.2}$$

The derivative of d_{RX} with respect to time can be computed by applying the derivative chain rule to eq. (4.14):

$$\begin{aligned}
 \frac{\partial d_{RX}}{\partial t} &= \frac{\partial d_{RX}}{\partial x_{RX}} \frac{\partial x_{RX}}{\partial t} + \frac{\partial d_{RX}}{\partial y_{RX}} \frac{\partial y_{RX}}{\partial t} \\
 &= \frac{1}{d_{RX}} [(x_{RX} - x_{Q_D}) v_{RX,x} + (y_{RX} - y_{Q_D}) v_{RX,y}].
 \end{aligned} \tag{C.3}$$

In similar way the derivative of d_{TX} can be calculated:

$$\frac{\partial d_{TX}}{\partial t} = \frac{1}{d_{TX}} [(x_{TX} - x_{Q_D}) v_{TX,x} + (y_{TX} - y_{Q_D}) v_{TX,y}] \tag{C.4}$$

By substituting (C.3) and (C.4) into (C.2) and (C.1), we finally get $v_{Q_D,x}$.

The diffraction point's acceleration ($a_{Q_D,z}$) can be computed in a similar way by time deriving (C.1).

Appendix D

Proof of Theorem 1

To solve the problem in (7.19), Lagrange dual method is used [86]. For this purpose, we first need the Lagrange function of this problem. The Lagrangian can be written as:

$$\begin{aligned}
\mathcal{L}(P_{m,k}^{(p,r)}, P_{m,k}^{(p,s)}, P_{m,k}^{(s)}, \alpha_1, \alpha_2, \lambda, \delta, \epsilon, \xi, \theta, \mu, \nu, \kappa) &= \alpha_1 + \alpha_2 \\
&+ \lambda(P_m^{(p,\max)} - P_{m,k}^{(p,s)}) + \delta(P_k^{(s,\max)} - P_{m,k}^{(p,r)} - P_{m,k}^{(s)}) \\
&+ \epsilon(R_{m,k}^{(p,r)} - R_{m,k}^{(p,s)}) + \xi(R_{m,k}^{(p,s)} - R_m^{(p,\min)}) \\
&+ \delta(R_{m,k}^{(p,r)} - R_m^{(p,\min)}) + \mu(R_{m,k}^{(s)} - R_k^{(s,\min)}) \\
&+ \nu(R_{m,k}^{(p,s)} - \alpha_1(P_{m,k}^{(p,c)})) + \kappa(R_{m,k}^{(s)} - \alpha_2(P_{m,k}^{(s)} + P_c^{(s)})). \tag{D.1}
\end{aligned}$$

If the set of solutions $(P_{m,k}^{(p,s)*}, P_{m,k}^{(p,r)*}, P_{m,k}^{(s)*}, \alpha_1^*, \alpha_2^*)$ is the solution of the problem in (7.19), then exist the Lagrange multipliers $\bar{\lambda}, \bar{\delta}, \bar{\epsilon}, \bar{\xi}, \bar{\theta}, \bar{\mu}, \bar{\nu}, \bar{\kappa}$ in order to satisfy the KKT conditions [84] for the problem (7.19). The conditions are as follows:

$$\begin{cases}
\frac{\partial \mathcal{L}}{\partial P_{m,k}^{(p,s)}} = \bar{\nu}(P_{m,k}^{(p,s)} - \alpha_1^*) - \bar{\lambda} - \bar{\epsilon}R_{m,k}^{(p,s)} = 0 \\
\frac{\partial \mathcal{L}}{\partial P_{m,k}^{(p,r)}} = (\bar{\epsilon} + \bar{\theta})R_{m,k}^{(p,r)} - \bar{\nu}\alpha_1^* - \bar{\delta} = 0 \\
\frac{\partial \mathcal{L}}{\partial P_{m,k}^{(s)}} = (\bar{\mu} + \bar{\kappa})R_{m,k}^{(s)} - \bar{\kappa}\alpha_2^* - \bar{\delta} = 0
\end{cases} \tag{D.2}$$

$$\frac{\partial \mathcal{L}}{\partial \alpha_1} = 1 - \bar{\nu} P_{m,k}^{(p,c)} = 0 \quad (\text{D.3})$$

$$\frac{\partial \mathcal{L}}{\partial \alpha_2} = 1 - \bar{\kappa} (P_{m,k}^{(s)} + P_c^{(s)}) = 0 \quad (\text{D.4})$$

$$\frac{\partial \mathcal{L}}{\partial \lambda} = P_m^{p,max} - P_{m,k}^{(p,s)} = 0 \quad (\text{D.5})$$

$$\frac{\partial \mathcal{L}}{\partial \delta} = P_k^{s,max} - P_{m,k}^{(p,r)} - P_{m,k}^{(s)} = 0 \quad (\text{D.6})$$

$$\frac{\partial \mathcal{L}}{\partial \epsilon} = R_{m,k}^{(p,r)} - R_{m,k}^{(p,s)} = 0 \quad (\text{D.7})$$

$$\frac{\partial \mathcal{L}}{\partial \xi} = R_{m,k}^{(p,s)} - R_m^{(p,min)} = 0 \quad (\text{D.8})$$

$$\frac{\partial \mathcal{L}}{\partial \theta} = R_{m,k}^{(p,r)} - R_m^{(p,min)} = 0 \quad (\text{D.9})$$

$$\frac{\partial \mathcal{L}}{\partial \xi} = R_{m,k}^{(s)} - R_k^{(s,min)} = 0 \quad (\text{D.10})$$

$$\frac{\partial \mathcal{L}}{\partial \nu} = R_{m,k}^{(p,s)} - \alpha_1^* P_{m,k}^{(p,c)} = 0 \quad (\text{D.11})$$

$$\frac{\partial \mathcal{L}}{\partial \kappa} = R_{m,k}^{(s)} - \alpha_2^* (P_{m,k}^{(p,c)} + P_c^{(s)}) = 0 \quad (\text{D.12})$$

Considering that $P_{m,k}^{(p,c)} > 0$ and $P_{m,k}^{(p,c)} + P_c^{(s)} > 0$ then from (D.3) and (D.4) we have

$$\begin{cases} \bar{\nu} = \frac{1}{P_{m,k}^{(p,c)}} \\ \bar{\kappa} = \frac{1}{P_{m,k}^{(s)} + P_c^{(s)}} \end{cases} \quad (\text{D.13})$$

and (D.11) and (D.12) are equivalent to

$$\begin{cases} \alpha_1^* = \frac{R_{m,k}^{(p,s)}}{P_{m,k}^{(p,c)}} \\ \alpha_2^* = \frac{R_{m,k}^{(s)}}{P_{m,k}^{(s)} + P_c^{(s)}}. \end{cases} \quad (\text{D.14})$$

The system equations (D.2), (D.5)–(D.10) are the KKT conditions of the optimization problem in (7.20) for $\nu = \bar{\nu}$, $\kappa = \bar{\kappa}$, $\alpha_1 = \alpha_1^*$, $\alpha_2 = \alpha_2^*$.

Appendix E

Summary of K-M algorithm

For the sake of completeness, we briefly introduce some definitions and a theorem regarding the K-M algorithm.

Bipartite: A bipartite graph is a graph whose vertices can be divided into two disjoint sets U and V , such that every edge connects a vertex in U to one in V . It can be represented as $G = (U, V, E)$ with E denoting the edges of the graph.

Weighted bipartite: A weighted bipartite is a bipartite in which each edge (u, v) has a weight factor $w(u, v)$.

Matching: A matching in a graph is a subset $H \subseteq G$. If H and G share the same vertex set, then H is called a complete matching. The size of a matching is denoted as $|H|$ which equals to the number of edges in H .

Feasible vertex labeling: A feasible vertex labeling in G is a real-valued function l on $U \cup V$ such that for $u \in U$ and $v \in V$,

$$l(u) + l(v) \geq w(u, v). \tag{E.1}$$

Equality subgraph: If l is a feasible labeling, we denote a subgraph of G as G_l which contains a number of edges and the endpoints of these edges. If the edges of G_l meet the condition $l(u) + l(v) \geq w(u, v)$, then G_l is called the equality subgraph for l .

Theorem 2: If l is a feasible vertex labeling for G , and H is a complete matching of U to V with $H \subseteq G_l$, then H is an optimal assignment of U to V .

E.1 Solving Optimal Relay Selection Problem Based on K-M Algorithm

Applying K-M algorithm to solve the optimal relay selection problem of the PUs, a weighted bipartite graph G with a bipartite division $G^0 = (U, V, E)$ is constructed, where the set of vertices U represents the set of PUs, that is, $U = [\text{PU}_1, \text{PU}_2, \dots, \text{PU}_M]$ and the set of vertices V represents the set of SUs, $V = [\text{SU}_1, \text{SU}_2, \dots, \text{SU}_K]$. The weight of the edge $(\text{PU}_m, \text{SU}_k)$ in the weighted bipartite graph can be defined as the joint energy efficiency of the m th PU and the k th SU, that is, $\eta_{m,k}^{(p,c)} + \eta_{m,k}^{(s)}$, $m = 1, \dots, M$ and $k = 1, \dots, K$.

The steps of solving the optimal relay selection problem based on K-M algorithm can be described as follows:

1. Find initial feasible vertex labeling and determine G_l^0 and choose an arbitrary matching H in G_l^0 .
2. If H is a maximum matching for G , then the optimization problem is solved. Otherwise, the label having not being allotted by the distribution H is selected in G_l^0 . Set $S = U$, and $T = \Phi$, which denotes the empty set.
3. $N_{G_l^0}(S)$ denotes the collection of points which connect with S in G_l^0 . If $N_{G_l^0}(S) \neq T$, go to step (2). Otherwise, $N_{G_l^0}(S) = T$. Find

$$\Delta = \min(l(u) + l(v) \geq w(u, v) | u \in S, v \in V - T) \quad (\text{E.2})$$

and replace existing labeling l with l' by

$$l'(u) = \begin{cases} l(u) - \Delta, & u \in S \\ l(u) + \Delta, & u \in T \\ l(u), & \text{otherwise.} \end{cases}$$

The process continues until an equal sub-graph consisting a complete match is obtained.

E.2 Complexity of the K-M Algorithm

Theoretically, the K-M algorithm is guaranteed to reach the global optimal solution [91]. It is the first proved polynomial algorithm and it was observed to be a strongly polynomial by Munkres in Reference [92]. Further, Edmonds and Karp in Reference [93] noticed that it can be modified to $O(n^3)$ running time.

In our case in each of the steps (1) or (2) the algorithm adds one edge to the matching and this happens $O(|V|)$. In addition, it needs $O(|V|)$ to find the right vertex (if there is one) and improving the labelling takes $O(|V|)$ time to find delta and to update the labelling accordingly. We might have to improve the labelling $O(|V|)$ times until we matching occurs. This makes for a total of $O(|V^2|)$. In all, there are $O(|V|)$ iterations each taking $O(|V|)$ work, leading to a total running time of $O(|V^3|)$.

Bibliography

- [1] O. O. Erunkulu, A. M. Zungeru, C. K. Lebekwe, M. Mosalaosi and J. M. Chuma, "5G Mobile Communication Applications: A Survey and Comparison of Use Cases," in *IEEE Access*, vol. 9, pp. 97251-97295, 2021
- [2] O. O. Erunkulu, E. N. Onwuka, O. Ugweje, and L. A. Ajao, "Prediction of call drops in GSM network using artificial neural network," *J. Teknol. Sist. Komput.*, vol. 7, no. 1, p. 38, 2019.
- [3] D. Bilibashi, E. M. Vitucci and V. Degli-Esposti, "Dynamic Ray Tracing: Introduction and Concept," *14th European Conference on Antennas and Propagation (EuCAP)*, 2020, pp. 1-5
- [4] D. Bilibashi, E. M. Vitucci and V. Degli-Esposti, "Dynamic Ray Tracing: A 3D Formulation," *International Symposium on Antennas and Propagation (ISAP)*, 2021, pp. 279-280
- [5] D. Bilibashi, E. M. Vitucci, V. Degli-Esposti, and A. Giorgetti, "An Energy-Efficient Unselfish Spectrum Leasing Scheme for Cognitive Radio Networks," *Sensors*, vol. 20, no. 21, p. 6161, Oct. 2020.
- [6] Z. Yun and M. F. Iskander, "Ray Tracing for Radio Propagation Modeling: Principles and Applications," in *IEEE Access*, vol. 3, pp. 1089-1100, 2015
- [7] H. T. Friis, "A note on a simple transmission formula," *Proc. IRE*, vol. 34, no. 5, pp. 254–256, May 1946.
- [8] M. Hata, "Empirical formula for propagation loss in land mobile radio services," *IEEE Trans. Veh. Technol.*, vol. 29, no. 3, pp. 317–325, Aug. 1980.

- [9] Y. Okumura, E. Ohmori, T. Kawano, and K. Fukuda, "Field strength and its variability in VHF and UHF land-mobile service," *Rev. Elect. Commun. Lab.*, vol. 16, nos. 9–10, pp. 825–873, 1968.
- [10] M. F. Iskander and Z. Yun, "Propagation prediction models for wireless communication systems," *IEEE Trans. Microw. Theory Techn.*, vol. 50, no. 3, pp. 662–673, Mar. 2002
- [11] E. Damosso and L. M. Coreia, COST Action 231: Digital Mobile Radio Towards Future Generation Systems: Final Report, European Commission, 1999.
- [12] F. Mani, *Improved ray-tracing for advanced radio propagation channel modeling*, PhD Thesis, ICTEAM, UCL Belgium, 2012.
- [13] P. Kyosti *et al.*. Ist-4-027756 winner ii d1. 1.2 v1. 2 winner ii channel models. *EBITG, TUI, UOULU, CU/CRC, NOKIA, Tech. Rep., Tech. Rep*, 2007.
- [14] L. Liu, C. Oestges, J. Poutanen, K. Haneda, P. Vainikainen, F. Quitin, F. Tufvesson, and P. De Doncker. "The cost 2100 mimo channel model", *IEEE Wireless Communications*, 19(6):92–99, 2012.
- [15] L. Azpilicueta, C. Vargas-Rosales and F. Falcone, "Intelligent Vehicle Communication: Deterministic Propagation Prediction in Transportation Systems," in *IEEE Vehicular Technology Magazine*, vol. 11, no. 3, pp. 29–37, Sept. 2016
- [16] F. Fuschini, H. El-Sallabi, V. Degli-Esposti, L. Vuokko, D. Guiducci, and P. Vainikainen, "Analysis of multipath propagation in urban environment through multidimensional measurements and advanced ray tracing simulation," *IEEE Trans. Antennas Propag.*, vol. 56, no. 3, pp. 848–857, Mar. 2008.
- [17] 3GPP, "Study on 3D channel model for LTE," Tech. Rep. 3GPP 36.873 (V12.2.0), July 2015.
- [18] "Aalto University, BUPT, CMCC, Nokia, NTT DOCOMO, New York University, Ericsson, Qualcomm, Huawei, Samsung, Intel, University of Bristol, KT Corporation, University of Southern California, "5G Channel Model for bands up to 100 GHz", Dec. 6, 2015," Tech. Rep. [Online]. Available: <http://www.5gworkshops.com/5GCM.html>

- [19] K. Haneda et al., "5G 3GPP-Like Channel Models for Outdoor Urban Micro-cellular and Macrocellular Environments," 2016 IEEE 83rd Vehicular Technology Conference (VTC Spring), 2016, pp. 1-7
- [20] F. Fuschini, E. M. Vitucci, M. Barbiroli, G. Falciasecca and V. Degli-Esposti, "Ray tracing propagation modeling for future small-cell and indoor applications: A review of current techniques," in *Radio Science*, vol. 50, no. 6, pp. 469-485, June 2015
- [21] F. Fuschini, M. Zoli, E.M. Vitucci, M. Barbiroli and V. Degli-Esposti, "A Study on Mm-wave Multi-User Directional Beamforming Based on Measurements and Ray Tracing Simulations," *IEEE Transactions on Antennas and Propagation*, Vol 67, No. 4, pp 2633-2644, April 2019
- [22] R. Alieiev, T. Hehn, A. Kwoczek and T. Kürner, "Predictive Communication and Its Application to Vehicular Environments: Doppler-Shift Compensation," in *IEEE Transactions on Vehicular Technology*, vol. 67, no. 8, pp. 7380-7393, Aug. 2018
- [23] N. Dreyer and T. Kürner, "An Analytical Raytracer for Efficient D2D Path Loss Predictions," *13th European Conference on Antennas and Propagation (EuCAP)*, 2019, pp. 1-5.
- [24] F. Quatresooz, S. Demey and C. Oestges, "Tracking of Interaction Points for Improved Dynamic Ray Tracing," in *IEEE Transactions on Vehicular Technology*, vol. 70, no. 7, pp. 6291-6301, July 2021
- [25] K. Guan et al., "5-GHz Obstructed Vehicle-to-Vehicle Channel Characterization for Internet of Intelligent Vehicles," in *IEEE Internet of Things Journal*, vol. 6, no. 1, pp. 100-110, Feb. 2019
- [26] A. F. Molisch, F. Tufvesson, J. Karedal and C. F. Mecklenbrauker, "A survey on vehicle-to-vehicle propagation channels," in *IEEE Wireless Communications*, vol. 16, no. 6, pp. 12-22, December 2009

- [27] M. Boban, R. Meireles, J. Barros, P. Steenkiste and O. K. Tonguz, "TVR—Tall Vehicle Relaying in Vehicular Networks," in *IEEE Transactions on Mobile Computing*, vol. 13, no. 5, pp. 1118-1131, May 2014
- [28] D. Vlastaras, T. Abbas, M. Nilsson, R. Whiton, M. Olbäck and F. Tufvesson, "Impact of a truck as an obstacle on vehicle-to-vehicle communications in rural and highway scenarios," *IEEE 6th International Symposium on Wireless Vehicular Communications (WiVeC 2014)*, 2014, pp. 1-6
- [29] F. Wiffen, L. Sayer, M. Z. Bocus, A. Doufexi and A. Nix, "Comparison of OTFS and OFDM in Ray Launched sub-6 GHz and mmWave Line-ofSight Mobility Channels," *2018 IEEE 29th Annual International Symposium on Personal, Indoor and Mobile Radio Communications (PIMRC)*, Bologna, 2018, pp. 73-79
- [30] M. Kline and I. Kay, *Electromagnetic theory and geometrical optics*, John Wiley Sons, 1965
- [31] F. Quatresooz, *Dynamic ray tracing techniques for mobile radio communications*, Master thesis, UCL Belgium, 2020.
- [32] C. A. Balanis, *Advanced engineering electromagnetics*, John Wiley Sons, 1999
- [33] D. McNamara, C. Pistorius, and J. Malherbe, *Introduction to the Uniform Geometrical Theory of Diffraction*, Artech House, 1990.
- [34] V. Degli-Esposti, "A diffuse scattering model for urban propagation prediction," *IEEE Trans. Antennas Propag.*, vol. 49, no. 7, pp. 1111–1113, Jul. 2001
- [35] P. Pongsilamane and H. L. Bertoni, "Specular and nonspecular scattering from building facades," *IEEE Trans. Antennas Propag.*, vol. 52, no. 7, pp. 1879–1889, Jul. 2004
- [36] V. Degli-Esposti, F. Fuschini, E. M. Vitucci, and G. Falciasecca, "Measurement and modelling of scattering from buildings," *IEEE Trans. Antennas Propag.*, vol. 55, no. 1, pp. 143–153, Jan. 2007
- [37] J. S. Lu, H. L. Bertoni, and V. Degli-Esposti, "Scale model investigation of mechanisms for scattering from office buildings at 2 GHz," *IEEE Trans. Antennas Propag.*, vol. 62, no. 12, pp. 6435–6442, Dec. 2014

- [38] E. M. Vitucci, F. Mani, V. Degli-Esposti, and C. Oestges, "Polarimetric properties of diffuse scattering from building walls: Experimental parameterization of a ray-tracing model," *IEEE Trans. Antennas Propag.*, vol. 60, no. 6, pp. 2961–2969, Jun. 2012
- [39] J. Keller, "One hundred years of diffraction theory," in *IEEE Transactions on Antennas and Propagation*, vol. 33, no. 2, pp. 123-126, February 1985
- [40] J. Keller, "Geometrical Theory of Diffraction*," *J. Opt. Soc. Am.* 52, 116-130 (1962).
- [41] C. Oestges, *Propagation Modelling of Low Earth-Orbit Satellite Personal Communication Systems*, PhD Thesis, UCL Belgium, 2000.
- [42] G. H. Martin, *Kinematics and Dynamics of Machines*, McGraw-Hill, 1968.
- [43] J. R. Taylor, *Classical mechanics*, University Science Books, 2005.
- [44] E. M. Vitucci, J. Chen, V. Degli-Esposti, J. S. Lu, H. L. Bertoni, X. Yin, "Analyzing Radio Scattering Caused by Various Building Elements Using Millimeter-Wave Scale Model Measurements and Ray Tracing," *IEEE Trans. Antennas Propag.*, Vol. 67, No. 1, pp. 665-669, Jan. 2019.
- [45] R.G. Kouyoumjian, P. H. Pathak, "A uniform geometrical theory of diffraction for an edge in a perfectly conducting surface", *Proc. IEEE*, vol. 62, No. 11, pp. 1448-1461, Nov. 1974.
- [46] T. Abbas, J. Nuckelt, T. Kürner, T. Zemen, C. F. Mecklenbräuker and F. Tufvesson, "Simulation and Measurement-Based Vehicle-to-Vehicle Channel Characterization: Accuracy and Constraint Analysis," in *IEEE Transactions on Antennas and Propagation*, vol. 63, no. 7, pp. 3208-3218, July 2015
- [47] R. Alieiev, T. Hehn, A. Kwoczek and T. Kürner, "Predictive Communication and its Application to Vehicular Environments: Doppler-Shift Compensation," *IEEE Trans. Veh. Technol.*, Vol. 67, No. 8, pp. 7380-7393, Aug. 2018.
- [48] R. Di Taranto, S. Muppirisetty, R. Raulefs, D.T.M. Slock, T. Svensson, H. Wymeersch, "Location-Aware Communications for 5G Networks", *IEEE Signal Proc. Magazine*, vol. 31, no. 6, pp. 102-112, November 2014

- [49] K. Witrisal, P. Meissner, E. Leitinger, Y. Shen, C. Gustafson, F. Tufvesson, K. Haneda, D. Dardari, A. Molisch, A. Conti, and M. Z. Win, “High-accuracy localization for assisted living: 5G systems will turn multipath channels from foe to friend,” *IEEE Signal Process. Mag.*, vol. 33, no. 2, pp. 59–70, Mar. 2016.
- [50] M. Koivisto, A. Hakkarainen, M. Costa, P. Kela, K. Leppanen, M. Valkama, “High-Efficiency Device Positioning and Location Aware Communications in Dense 5G Networks”, *IEEE Comm. Mag.*, vol. 55, no. 8, pp. 188-195, Aug. 2017.
- [51] M. N. de Sousa, R. S. Thomä, “Enhancement of Localization Systems in NLOS Urban Scenario with Multipath Ray Tracing Fingerprints and Machine Learning,” *Sensors*, Vol. 18, No. 11, 4073, 2018.
- [52] Federal Communications Commission, ET Docket No. 03-322, Dec. 2003.
- [53] J. Mitola and G. Q. Maguire, “Cognitive radio: making software radios more personal,” *IEEE Personal Communications*, vol. 6, no. 4, pp. 13-18, Aug. 1999.
- [54] K. Sithampanathan and A. Giorgetti, *Cognitive Radio Techniques: Spectrum Sensing, Interference Mitigation, and Localization*, Artech House, Sep. 2012.
- [55] A. Giorgetti, M. Varrella, and M. Chiani, “Analysis and performance comparison of different cognitive radio algorithms,” in *Proc. IEEE Int. Work. on Cognitive Radio & Advanced Spectrum Management (CogART)*, Aalborg, Denmark, pp. 127–131, Invited Paper, May 2009.
- [56] S. Aqeel and Y. Kok-Lim, “Spectrum Leasing in Cognitive Radio Networks: A Survey,” *International Journal of Distributed Sensor Networks*, Feb. 2014.
- [57] S. Haykin, “Cognitive radio: brain-empowered wireless communications,” *IEEE Journal on Selected Areas in Communications* 23 (2), 201–220, 2005.
- [58] R.W. Thomas, L.A. DaSilva, A.B. MacKenzie, “Cognitive networks”, in *Proc. IEEE DySPAN 2005*, pp. 352–360, November 2005
- [59] I. F. Akyildiz, Won-Yeol Lee, M. C. Vuran, S. Mohanty. “NeXt generation/dynamic spectrum access/cognitive radio wireless networks: A survey,” *Computer Networks* 50, pp. 2127–2159, 2006

- [60] L. Tao, H. Jianjun, Y. Guangxin, "Cooperative Communication and Cognitive Radio" [Online] Available:
http://wwen.zte.com.cn/endata/magazine/ztecommunications/2009year/no1/articles/200903/t20090319_170890.html.
- [61] P. Y. Nie and P. Zhang, "A note on Stackelberg games," *Chinese Control and Decision Conference*, Yantai, China, pp. 1201-1203, May 2008.
- [62] G. Scutari and J. Pang, "Joint Sensing and Power Allocation in Nonconvex Cognitive Radio Games: Nash Equilibria and Distributed Algorithms," *IEEE Transactions on Information Theory*, vol. 59, no. 7, pp. 4626-4661, July 2013.
- [63] T. Elkourdi and O. Simeone, "Spectrum Leasing via Cooperation With Multiple Primary Users," *IEEE Transactions on Vehicular Technology*, vol. 61, no. 2, pp. 820-825, Feb. 2012.
- [64] S. M. M. Toroujeni, S. M. Sadough, and S. A. Ghorashi, "Spectrum Leasing for OFDM-Based Cognitive Radio Networks," *IEEE Transactions on Vehicular Technology*, vol. 62, no. 5, pp. 2131-2139, June 2013.
- [65] M. Hafeez and J. M. H. Elmirghani, "Dynamic Spectrum Leasing for Bi-Directional Communication: Impact of Selfishness," *IEEE Transactions on Communications*, vol. 64, no. 6, pp. 2427-2437, June 2016.
- [66] Y. Tang, D. Grace, and L. Wang, "Spectrum Leasing and Relay Selection in Multiuser Cooperative Cognitive Radio Networks," *Journal of Communications*, vol. 9, no. 3, pp. 198-207, Mar. 2014.
- [67] Z. Liu, M. Zhao, Y. Xie, X. Li and K. Ma, "Relay selection and power allocation for spectrum leasing in cooperative cognitive radio networks," *Proc. Chinese Control Conference (CCC)*, Dalian, China, pp. 8958-8963, July 2017.
- [68] C. Zhai and W. Zhang, "Adaptive Spectrum Leasing with Secondary User Scheduling in Cognitive Radio Networks," *IEEE Transactions on Wireless Communications*, vol. 12, no. 7, pp. 3388-3398, July 2013.

- [69] A. H. Bastami and P. Kazemi, "Cognitive Multi-Hop Multi-Branch Relaying: Spectrum Leasing and Optimal Power Allocation," *IEEE Transactions on Wireless Communications*, vol. 18, no. 8, pp. 4075-4088, Aug. 2019.
- [70] Y. Ma, X. Yin, X. Yang, and Q. Liu, "Resource allocation for spectrum-leasing based CRN with delay-sensitive traffic," *EURASIP Journal on Wireless Communications and Networking*, article 108, June 2017.
- [71] S. Yin, Z. Qu, Z. Wang, and L. Li, "Energy-Efficient Cooperation in Cognitive Wireless Powered Networks," *IEEE Communications Letters*, vol. 21, no. 1, pp. 128-131, Jan. 2017.
- [72] S. Chatterjee, S. P. Maity, T. Acharya, "Energy-Spectrum Efficiency Trade-Off in Energy Harvesting Cooperative Cognitive Radio Networks," *IEEE Transactions on Cognitive Communications and Networking*, vol. 5, no. 2, pp. 295-303, Jun. 2019.
- [73] Asaduzzaman, H. Y. Kong, and I. Koo, "Opportunistic relaying based spectrum leasing for cognitive radio networks," *Journal of Communications and Networks*, vol. 13, no. 1, pp. 50-55, Feb. 2011.
- [74] M. F. Kader, Asaduzzaman, and M. Chowdhury, "Cooperative secondary user selection as a relay for the primary system in underlay cognitive radio networks," *15th International Conference on Computer and Information Technology (IC-CIT)*, Chittagong, Bangladesh, pp. 275-278, Dec. 2012.
- [75] C. Shao, H. Roh, and W. Lee, "Aspiration Level-Based Strategy Dynamics on the Coexistence of Spectrum Cooperation and Leasing," *IEEE Communications Letters*, vol. 18, no. 1, pp. 70-73, Jan. 2014.
- [76] D. Bilibashi and R. Chai, "Energy Efficiency Based Resource Allocation Scheme for Cooperative Cognitive Radio Networks," *International Journal of Electronics and Electrical Engineering*, vol. 5, no. 1, pp. 7-14, Feb. 2017.
- [77] R. Jagannathan, "On some properties of programming problems in parametric form pertaining to fractional programming," *Management Science*, vol. 12, no. 7, pp. 609-615, 1966.

- [78] W. Dinkelbach, "On nonlinear fractional programming," *Management Science*, vol. 13, pp. 492–498, 1967.
- [79] M. Dür, R. Horst, and N. Thoai, "Solving sum-of-ratios fractional programs using efficient points," *Optimization*, vol. 49, pp. 447–466, Jan. 2001.
- [80] D. Darsena, G. Gelli, F. Melito and F. Verde, "Performance Analysis of Amplify-and-Forward Multiple-Relay MIMO Systems With ZF Reception," *IEEE Transactions on Vehicular Technology*, vol. 64, no. 7, pp. 3274-3280, July 2015
- [81] S. Bagheri, F. Verde, D. Darsena and A. Scaglione, "Randomized Decode-and-Forward Strategies for Two-Way Relay Networks," *IEEE Transactions on Wireless Communications*, vol. 10, no. 12, pp. 4214-4225, Dec. 2011
- [82] D. P. Bertsekas, *Nonlinear Programming*, 2nd edition. Athena Scientific, 1999.
- [83] S. He, Y. Huang, L. Yang, and B. Ottersten, "Coordinated Multicell Multiuser Precoding for Maximizing Weighted Sum Energy Efficiency," in *IEEE Transactions on Signal Processing*, vol. 62, no. 3, pp. 741-751, Feb. 2014.
- [84] J. Borwein, and A. Lewis, *Convex Analysis and Nonlinear Optimization: Theory and Examples*, Springer Verlag, 2006
- [85] D. W. K. Ng, E. S. Lo, and R. Schober, "Energy-Efficient Resource Allocation in OFDMA Systems with Large Numbers of Base Station Antennas," in *IEEE Transactions on Wireless Communications*, vol. 11, no. 9, pp. 3292-3304, Sep. 2012.
- [86] S. Boyd, and L. Vandenberghe, *Convex optimization*, Cambridge University Press, 2004.
- [87] S. Boyd, and A. Mutapcic, "Subgradient methods," notes for EE364 Stanford University, Winter 2006-07.
- [88] E. T. Lee, and J. W. Wang, *Statistical Methods for Survival Data Analyses*, Third Edition, John Wiley and Sons, Inc., pp. 428-432, 2003.
- [89] H. Kuhn, "The hungarian method for the assignment problem," *Naval Research Logistics Quarterly*, vol. 2, no. 1-2, pp. 83–97, 1955.

- [90] K. K. Mensah, R. Chai, D. Bilibashi, and F. Gao, "Energy efficiency based joint cell selection and power allocation scheme for HetNets," *Digital Communications and Networks*, vol. 2, no. 4, pp. 184-190, Nov. 2016.
- [91] C. Hong, Z. Jingjing, C. Chunfeng, and C. Qinyu, "Solving large-scale assignment problems by Kuhn-Munkres algorithm," *International Conference on Advances in Mechanical Engineering and Industrial Informatics*, Hangzhou, China, Apr. 2016.
- [92] F. Bourgeois, and J.C. Lassalle, "An extension of the munkres algorithm for the assignment problem to rectangular matrices," *Communications of the Acm*, vol. 14, pp. 802-804, Dec. 1971.
- [93] J. Edmonds, and R.M. Karp, "Theoretical improvements in algorithmic efficiency for network flow problems", *Communications of the Acm*, vol. 19, pp. 248-264, Apr. 1972.